X-ray Diffraction Analysis of InAs Nanowires

Faculty of Science and Engineers
Of Physics
University of Siegen
Germany

For the PhD degree

by

Anton Davydok
Solid State Physics Group
University of Siegen
57072, Walter-Flex-Str, 3
Siegen, Germany

X-ray Diffraction Analysis of InAs Nanowires

DISSERTATION

zur Erlangung des Grades eines Doktors

der Naturwissenschaften

vorgelegt von

M. Sc. Anton Davydok

eingereicht bei der Naturwissenschaftlich-Technischen Fakultät

der Universität Siegen

Siegen 2013

Referees:

Prof. Dr. Ullrich Pietsch
Prof. Dr. Vaclav Holy
Date of examination: 08.04.2013

Contents

List of abbreviations I

Abstracts II

Zusammenfassung . . . . . . **III**

Chapter 1 Introduction 1

Chapter 2 VLS/VSS growth 3

2.1 Why InAs nanowires 4

2.2 Vapor-Liquid-Solid Growth 6

2.3 Crystal phases of InAs. 11

Chapter 3 X-ray Diffraction: Kinematical Scattering Theory. . 16

3.1 Crystal structure 17

3.2 Reciprocal space 18

3.3 X-ray diffraction on crystal 20

3.4 The Laue equations and Bragg interpretation of diffraction conditions 22

3.5 Lattice sum and Laue conditions . . . 23

3.6 Atomic form factor and structure factor . . . 24

3.7 Crystal truncation rod 25

3.8 X-ray diffraction from zinc-blende and wurtzite structures . 27

3.9 Coherence of X-ray beam 30

3.10 Reciprocal space coordinates 32

Chapter 4 MOVPE Au-assisted growth of InAs nanowires on GaAs[111]B substrate. 33
4.1 Introduction 34
4.2 Experimental technique 35
4.3 Results and discussion 37
4.4 Growth model 40
4.5 Summery 41
Chapter 5 Growth parameters influence on phase composition and defect structure of InAs nanowires grown by self-assisted molecular beam epitaxy onto Si (111) 42
5.1 As-/In/rich conditions 47
5.2 Substrate coverage 49
5.3 Substrate temperature 51
5.4 Growth rate 54
5.5 Conclusions 57
Chapter 6 Structural Phase composition of InAs nanowires grown by self-assisted molecular beam epitaxy onto Si(111) . 58
6.1 Introduction 59
6.2 MBE growth 60
6.3 Experimental technique and results. . . . 61
6.3.1 Ensemble measurements 62
6.3.2 Grazing incident diffraction 67
6.3.3 Single wire resolved measurements . . . 68
6.4 Simulations 72
6.5 Discussion. 75
6.6 Conclusions 76

Conclusions 77

References 79

Acknowledgments 82

Appendix - MATLAB scripts 83

List of abbreviations

AFM	Atomic Force Microscopy
Au	Chemical symbol denote gold
bcc	body centered cell
CTR	Crystal Truncation Rod
EDX	Energy Dispersive X-ray
ESF	Extrinsic Stacking Faults
ESRF	European Synchrotron Radiation Facility
fcc	face centered cell
FET	Field-Effect Transistor
FWHM	Full Width Half Maxima
FZP	Fresnel Zone Plate
GaAs	Galliumarsenid
GID	Grazing Incident Diffraction
GR	Growth Rate
HSQ	Hydrogen Silsesquioxane
InAs	Indiumarsenid
ISF	Intrinsic Stacking Faults
LED	Light-Emitting Diode
MBE	Molecular Beam Epitaxy
ML	Monolayer
MOCVD	Metal-Organic Chemical Vapour Deposition
MOVPE	Metal-Organic Vapour Phase Epitaxy

NW . . .	Nanowire
PL . . .	Photoluminescence
RHEED . .	Reflection High-Energy Electron Diffraction
RSM . . .	Reciprocal Space Map
SEM . . .	Scanning Electron Microscopy
SET . . .	Single-Electron Transistors
SF . . .	Stacking Fault
Si . . .	Silicon
SiO_x . . .	Silicon Oxide
TEM . . .	Transmission Electron Microscopy
TMI . . .	Trimethylindium
TPL . . .	Triple Phase Line
TW . . .	Twin defects
VLS . . .	Vapor-Liquid-Solid
VS . . .	Vapor-Solid
WZ . . .	Wurtzite
XRD . . .	X-ray Diffraction
ZB . . .	Zincblende

Abstracts

Semiconductor nanowires have attracted great interest as building blocks for future electronic and optoelectronic devices. The variability of the growth process opens the opportunity to control and combine the various properties tailoring for specific application. It was shown that the electrical and optical characteristics of the nanowires are strongly connected with their structure. Despite intensive research in this field, the growth process is still not fully understood. In particular, extensive real structure investigations are required. Most of the reports dedicated on the structural researches are based on the results of scanning electron microscopy (SEM) or transmission electron microscopy (TEM). SEM provides an image of the surface with nanostructures and is mainly used to describe the morphology of the sample, but it does not bring information about the internal structure, phase composition and defect structure. At the same time, the internal structure can be examined by TEM down to atomic scale. TEM image of good quality are very expensive due to the efforts in sample preparation and in localisation of a single object. All these aspects make the statistical structural analysis difficult.

In the present work, X-ray diffraction analysis has been applied for structural investigation of InAs nanowires grown by different techniques. Using various X-ray diffraction geometries, the nanowire systems were investigated in terms of the lattice parameters, phase composition, strains and displacement fields and stacking defects.

In particular, realizing grazing incidence diffraction and controlling the penetration depth of X-ray beam, we characterized sample series grown by Au-assisted metal organic phase epitaxy on GaAs [111]B substrate with different growth time. According to the results of SEM and X-ray investigations, a model of the growth process has been proposed.

A more detailed analysis was performed on InAs nanowires grown by molecular beam epitaxy (MBE) on Si substrate. MBE provides the opportunity to combine a group III-V material with nearly any semiconductor substrate independent from lattice mismatch. Vertically aligned nanowire ensembles were studied performing X-ray diffraction experiments in different scattering geometries. Considering the nanowires are composed by structural units of zinc-blende and wurtzite the latter one was found to be affected by a high density of

stacking faults already at nanowires with short growth time. The stacking faults density was estimated by Monte-Carlo simulations based on model of ensemble average. A strong signal of unique zinc-blende reflection was observed as well. Coherent X-ray diffraction experiments with the use of a nano-focus setup have shown 'bar-code' patterning due to stacking fault arrangement within the nanowire. The found highly defective structure cannot be attributed to wurtzite or zinc-blende phases alone. Also parasitic islands were found on the samples surfaces and characterized as pure zinc-blende objects.

Zusammenfassung

Halbleiter-Nanodrähte sind von großem Interesse als Bausteine für zukünftige elektronische und optoelektronische Bauelemente. Die Variabilität des Wachstumsprozesses eröffnet die Möglichkeit, spezifische Eigenschaften unterschiedlicher Materialien für spezifische Anwendungen zu spezifizieren. Es wurde gezeigt, dass die elektrischen und optischen Eigenschaften der Nanodrähte stark mit ihrer Struktur verbunden sind. Ungeachtet unfangreicher Untersuchungen in diesem Feld, ist der Wachstumsprozess noch nicht vollständig verstanden. Insbesondere sind umfangreiche Realstrukturuntersuchungen erforderlich. Viele Untersuchungen zur Realstruktur basieren auf Ergebnissen der Rasterelektronenmikroskopie (SEM) oder Transmissionselektronenmikroskopie (TEM). SEM bietet ein Bild der Oberfläche der Nanostrukturen, aber es liefert keine Informationen über die innere Struktur. Andererseits kann man mit TEM die interne Struktur auf atomarer Längenskala untersuchen. Aber eine TEM-Aufnahme von guter Qualität ist wegen des großen Aufwandes bei der Probenpräparation und insbesondere bei Lokalisierung einzelner Objekte sehr teuer. Alle diese Aspekte machen die statistische Strukturanalyse schwierig.

In dieser Arbeit werden verschiedene Verfahren der Röntgenbeugung für strukturelle Untersuchungen an InAs-Nanodrähte verwendet, die durch verschiedene Techniken gewachsen wurden. Bei Verwendung verschiedener Streugeometrien werden die Nanodrähte in Bezug auf ihren Gitterparameter, Phasenzusammensetzung und Stapelfehler untersucht.

Bei Verwendung der Geometrie, wurde eine Probenserie,die mittels von Au-assistierter MOVPE auf GaAs [111] B Substrat mit unterschiedlichen Wachstumszeit gewachsen wurden, charakterisiert. Unter Verwendung von Ergebnissen von SEM- und Röntgen-Untersuchungen wurde ein Modell des Wachstumsprozesses vorgeschlagen worden.

Eine genauere Analyse wurde an InAs-Nanodrähten vorgenommen, die mittels MBE auf Si Substrat aufgewachsen wurden. MBE bietet dabei die Möglichkeit, AIIIBV Halbleiter mit nahezu jedem anderen Halbleitersubstrat zu kombinieren, ungeachtet der Gitterfehlanpassung. Vertikal ausgerichtete Nanodraht-Ensembles wurden mittels Röntgenbeugung in verschiedenen Streugeometrien untersucht. Die Nanodrähte enthielten sowohl Zinkblende als auch Wurzit Struktureinheiten erwiesen und wiesen bereits nach kurzer

Wachstumzeit eine hohe Dichte von Stapelfehlern auf. Die Stapelfehlerdichte des Ensemble Mittelwertes wurde mittels Monte-Carlo-Simulationen aus der Kurvenform spezifischen Beugungsreflexen abgeschätzt. Ein starkes Signal der einzigartigen Zinkblende-Reflexion wurde ebenfalls beobachtet. Kohärente Röntgenbeugungsexperimente mit kohärenter Röntgenstrahlung wurden unter Verwendung eines Nano-Fokus Setups durchgeführt und lieferten ein "Bar-Code" Strukturierung der Beugungsreflexe, die aus der konkreten Anordnung von Stapelfehlern innerhalb des Nanodrahtes resultieren. Die gefundene Struktur des Braggreflexes kann nicht mehr mit reinen Wurtzit und Zinkblende Phasen beschrieben werden. Auch parasitäre Inseln wurden auf der Substratoberfläche gefunden, die als reine Zinkblende-Objekte charakterisiert wurden.

Chapter 1

Introduction

X-ray diffraction is one of the standard tools for crystal structure analysis which was developed 100 years ago. The use of synchrotron radiation opened new opportunities for structural investigations. Modern sources produce a flux of photons being high enough to investigate small scale objects. In combination with novel two-dimensional detectors, one is able to run fast measurement, producing three-dimensional information of the structure under investigation. X-ray diffraction opens the possibilities to examine ensembles of nano-structures and, with the use of focusing setups, individual objects on the micro- and nano-scale.

The tendency of electronics to decrease in size opens new opportunity for applications. Considerable reduction in object size of semiconductor materials had a crucial effect on well known physical properties. The geometry of nanowires offers the capability to form heterostructures between highly lattice-mismatched materials, because the strain energy can be released at the free-standing nanowires sidewalls. In particular, this allows for the combination of groups III-V materials with the Si technology. Nanowires growth is typically realized using the vapour-liquid-solid mode onto [111] planes of a zinc-blende or diamond type of semiconductor. The knowledge about new nanostructure properties constantly increases with an increasing number of fields of future applications. However, the journey from a new scientific field to practical application requires deeper understanding.

The development of new growth modes expands the range of the materials used in nanowires growth. An increasing number of reports, dedicated to the properties of nanostructures, is being published. X-ray diffraction methods occupy an important place in this field. Compared to standard methods of structural analysis as transition electron microscopy, X-ray diffraction experiments are easier to perform and enable ensemble analysis. Also during last

years huge success has been achieved in focusing the X-ray beam down to nanometers size, with stability high enough to perform X-ray measurements at surface nano-objects.

The thesis is arranged as follows: in Chapter 2 we introduce the growth mechanisms of nanowires and describe technical aspects of growth realization. Also we introduce crystal structure types, phase descriptions and structural relations. Chapter 3 is dedicated to the basics of kinematical X-ray diffraction theory, specifications of experimental geometries and calculations of reciprocal space maps. Chapter 4 presents the X-ray structure analysis of Au-catalysed InAs nanowires grown by metal-organic-phase-epitaxy on GaAs [111]B substrate. The results obtained in symmetric out-of-plane and grazing incident geometries describe the time evolution of a growing nanowire system. As main outcome, a growth model is suggested. Chapter 5 introduces the influence of growth parameters on the structure of nanowires in terms of stacking faults density and phase composition. Chapter 6 contains our findings from self-assisted InAs nanowires grown by molecular beam epitaxy on Si substrate. The results are obtained from samples series produced by different growth time. Observations made with nano-focus setups and Monte Carlo simulations are also presented in the chapter. Chapter 4 and chapter 6 are based on following articles:

1. J. Brauer, U. Pietsch, A. Davydok, A. Biermanns, J. Grenzer, V. Gottschalch, G. Wagner, "X-ray investigation of the interface structure of free standing InAs nanowires grown on GaAs $[\bar{1}\,\bar{1}\,\bar{1}]$B", Appl. Phys. A, 96, 851, 2009
2. A. Davydok, E. Dimakis, A. Biermanns, L. Geelhaar, U. Pietsch „Structural Phase composition of InAs nanowires grown by self-assisted molecular beam epitaxy onto Si(111)", *in preparation*

Chapter 2

Nanowires growth: thermodynamics, models, structures

The peculiarities of nanowire growth are subject of scientific debate. In recent years, great progress in the study of the growth process has been achieved. However, there are still open questions that need to be solved prior to a productive application of nanostructures in industry. Nanoscale structures are characterized by new properties and new prospects, especially in the creation of new semiconductor heterostructures. These properties are connected to their structure. Description of the growth process is an important step in the study of new materials. That's why information about the internal structural order is required.

2.1 InAs is material for nanowires

The main motivation behind the development in nanoscience is future applications of those semiconductor materials with novel properties not attainable on the macroscale. Semiconductors are materials with a narrow energy gap between valence and conduction bands. Their electrical properties can be tuned, for example, by adding doping carriers. This characteristic makes semiconductors indispensable to microelectronics applications. However, electrical properties are associated also with the crystal structure of the material. The functionality of novel nanomaterials and their impact on society will be ultimately dictated by increasing understanding and ability for precise control of structural properties, size uniformity, and dopant distribution in atomic level. Nanostructured materials exhibit interesting size- and morphology-dependent properties and offer unique opportunities for fundamental studies and applications. In particular, semiconductor nanowires and nanowire heterostructures became an important class of nanomaterials for applications in nanophotonics and optoelectronics. Nanowire device functionalities, such as emission wavelength and efficiency, are sensitive to miniscule changes in interface quality and interdiffusion between nanowire segments or surface passivation layers.

For device materials, the important characteristics are lattice parameter, band gap and density of states. The lattice parameter is defined by the size of the crystal unit cell and plays a crucial role in the creation of heterostuctures via integration of one material onto another. Lattice mismatches of the materials become a reason of structural defects creation at the hetero interface. The band gap characterizes the forbidden electron energies in the crystal band structure. This characteristic is strongly connected with light absorption wavelength and carrier concentration. The density of states (DOS) describes how many available electrons states can be found within a specific energy range [1].

Semiconductor materials are compounds by groups IV elements or binary compounds formed by elements of groups III-V, II-VI or IV-VI. In this work we concentrate on InAs. This material is characterised by a narrow band gap (0.36eV) compared to other semiconductors (Fig. 2.1). Together with its high electron mobility and small electron effective mass, InAs is extremely promising for applications in high-speed electronics. In addition, surface passivation has a lower effect on the conductivity. Most of the bulk semiconductors exist in a cubic zinc-blende crystal structure. In nanoscale the material can be grown in the

hexagonal phase as found for SiC and ZnSe [2, 3] for example. The zinc-blende and wurtzite phases have different electronic band structures [4].

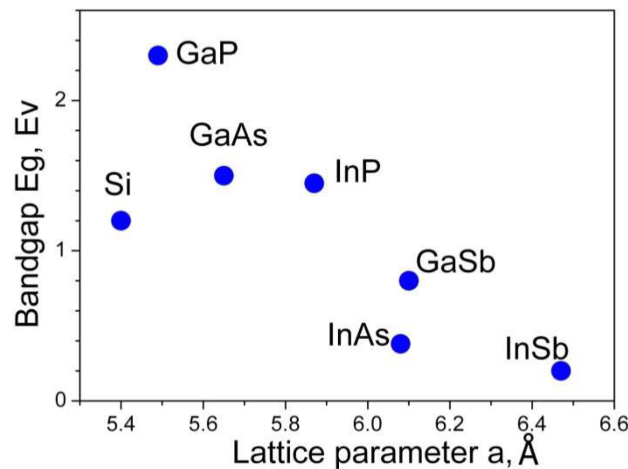

Figure 2.1 Energy band gap and lattice parameter of semiconductor materials

Due to its high electron mobility InAs has attracted interest as III-V complementary in metal-oxide-semiconductor (CMOS) technology in combination with other semiconductor materials. In this case, crystal lattice mismatches become a significant problem. Strain becomes released via misfit dislocations what is a harmful effect for devices manufacturing. The small diameter of hexagonally shaped nanowires opens the possibility to grow strain relaxed semiconductor heterostructures independent from lattice mismatches of materials. Free edges of nanowires enable to release the strain by expanding (compressing) the edges of the structure.

Prototypes of devices based on InAs NWs grown onto various substrates have been demonstrated already [5, 6]. But the growth process is not well-studied up to now. There are still a lot of open questions requiring further growth experiments and structural investigations. In case of InAs growth on GaAs substrate (lattice mismatch 7%) the problem of lattice mismatch was solved by applying metal catalysts. The metal catalysts can be chosen from a variety of materials with suitable chemical properties. Gold is the most common catalyst. It is inert in the liquid phase and does not react with the vapor phase of most semiconductors. It also forms a liquid alloy with growth materials. On other hand, one can find many reasons which make the use of gold undesirable, for example with Si substrate (lattice mismatch with InAs 11%). The unacceptable

contamination and the large diffusion length of Au in Si are accompanied with the formation of deep-level electronic traps [7].

2.2 Vapor-Liquid-Solid growth

The most common way to grow semiconductor NWs is the Vapor-Liquid-Solid mechanism. In 1964 Wagner and Elis suggested an explanation of the formation of Si whiskers from vapor phase with the existence of liquid gold on the top of the substrate surface [8]. The development of the so called free-standing nanowhiskers was described by the Vapor-Liquid-Solid model. The name of the growth mechanism came from the three phases appearing simultaneously – vapor-phase precursor ($SiCl_4$), liquid mixture of gold and silicon under growth temperature and solid whiskers.

Considering the thermodynamic of the process, the phase transition reaction requires supersaturation of one of the diluted growing components. The growth takes place because of the chemical potential difference. The reaction rate is defined by kinetic factors like the amount of supplying source material.

For two-compound systems like InAs, the growth depends on the reaction of two elements: indium and arsenic. The two materials are introduced separately into the growth chamber. As shown in many publications, the ratio of both fluxes directly influences the growth process [9, 10]. Also, the difference of chemical potentials between the vapor and solid phases of the two materials is an important factor. NW growth is initiated by the use of a metallic catalyst. At growth temperature, the catalyst is liquid and cooperates with the source materials. In case of supersaturation of source materials within the catalyst growth takes place the bottom interface. However, the composition of alloy catalyst was unknown for long time. In addition, it is not fully clear which kind of reaction takes place at the growing interface. Many compound semiconductor materials produce an unstable composition with metals which can be used as catalysts (commonly Au). Usually, the catalyst droplet contains only one of the growing elements in considerable amount to catalyze the growth. From III-V materials it is the group III element. Here, we come with the question how the element of group V behaves during the growth of wire? This problem could be solved considering that the material of group V moves along the growing surface in the particles. High diffusion rate of arsenic along Au-grain has been shown [11]. The group III element forms many different alloys with Au. Some of these

alloys have melting points in the range of the growth temperatures of NWs. Current models still do not fully explain the development of binary compound NWs. Prior to growth experiment one should study the phase diagrams of the growing components [12].

It is reported that growth occurs from a supersaturated alloy with a rate higher than it is expected from supply of vapor phase. One possible explanation suggests that the source particle decomposes at the growth surface. Here, the required growth rate depends on the catalyst and the source materials [13, 14]. Also, the substrate influences the decomposition process of the source material [15]. The choice of materials defines the success of the future growth. A list of source materials and possible catalysts has been published in [16].

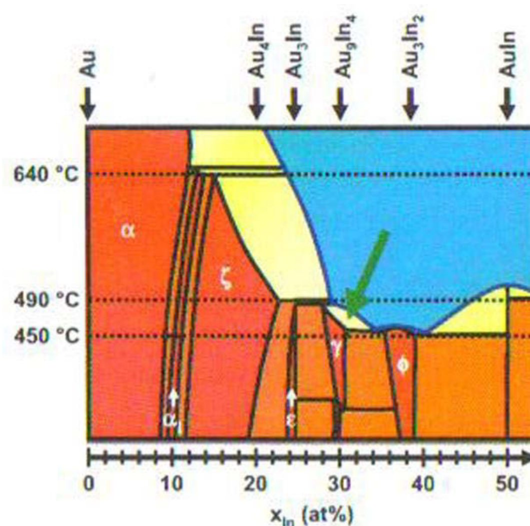

Figure 2.2 Au-In phase diagram with possible alloys under growth temperature conditions

During VLS growth of InAs the alloy droplet contains a considerable amount of group-III material. As a result, the growth of desirable InAs NW heterostructures is prevented [17]. Indium has low melting point of about 156 °C whereas the InAs NW grows usually at temperature of 400-500°C. The melting point of gold is 1064 °C. But Au and In create an eutectic alloy (alloy of materials with melting point lower then melting point of the materials separately) with melting temperature of 454°C (Fig. 2.2). In addition, under certain temperature conditions gold can react with the substrate material like in case of InAs growth on GaAs substrate. The Au-Ga alloy shows eutectic behavior as well with temperature even lower then found for the Au-In case [18].

In practice, Au-assisted NWs growth can be described by five steps: 1) preparation of the semiconductor substrate; 2) deposition of a thin layer of gold;

3) heating the substrate up to melting point of gold; 4) temperature stabilization; 5)steady supply of source materials(Fig. 2.3). Once the catalysts material is saturated by NWs source material, the vertical growth of the semiconductor NWs takes place. A more specific Au-catalyzed growth is described in Chapter 4 based on own experimental results.

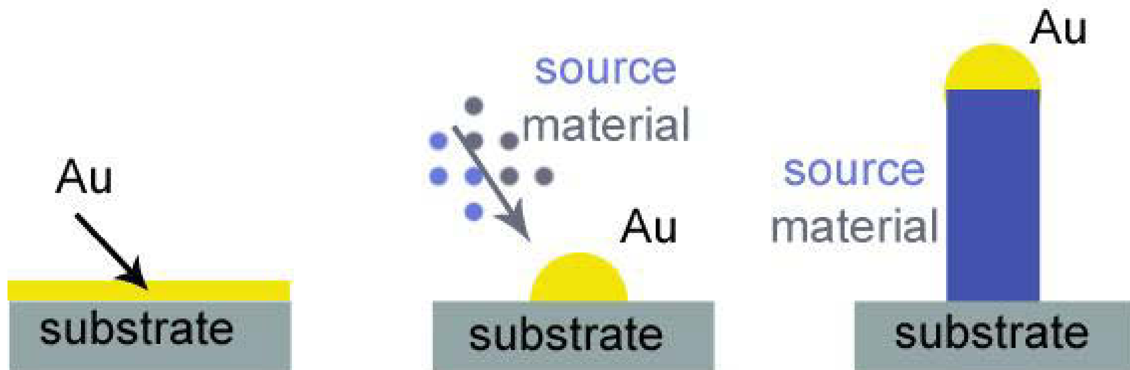

Figure 2.3 Growth scheme of semiconductor nanowires via Au-assisted vapor-liquid-solid growth

For CMOS technology the growth of InAs on Si is interested. The lattice mismatch between InAs and Si is 11.6%, but composition of both materials in one device opens a wide perspectives for high-speed electronics. Low band gap material with electrical properties of Si may become a base for new generation of semiconductor devices.

In case of Si substrate, the use of gold as catalyst must be avoided. Due to the large diffusion length of gold into Si, such devices will be highly defected. For realization of the growth process, the thermodynamics of Au-Si alloy prevents the combination of these materials. In case of Au and Si, there is a single eutectic point at 363°C. At this point the composition of the liquid alloy will contain 18.6% of Si. When a liquid Au-Si alloy of this composition is cooled, solid Au and Si will sediment out at the eutectic temperature. If a liquid alloy with, for example, 50 % each Au and Si is cooled, this alloy will precipitate Si only. This is accompanied by decreasing the Si composition in the liquid, until it reaches the eutectic composition. At this point both Au and Si will be precipitated. The vapor-liquid-solid mechanism assumes that a liquid Au-Si alloy forms above the eutectic point. It leads to a local increase of the amount of Si in the vapor near the particle. Si will be dissolved in the particle until the composition reaches the liquid state. Beyond this point, if the local concentration of Si close to the particle is still higher than that within the particle, a small amount of Si will continue to enter

the particle. This increases the composition beyond the liquid line in the phase diagram (Fig. 2.4). In this case, the alloy is thermodynamically unstable. The particle will precipitate Si in order to re-establish the stable composition of Si and Au in the binary liquid alloy [19].

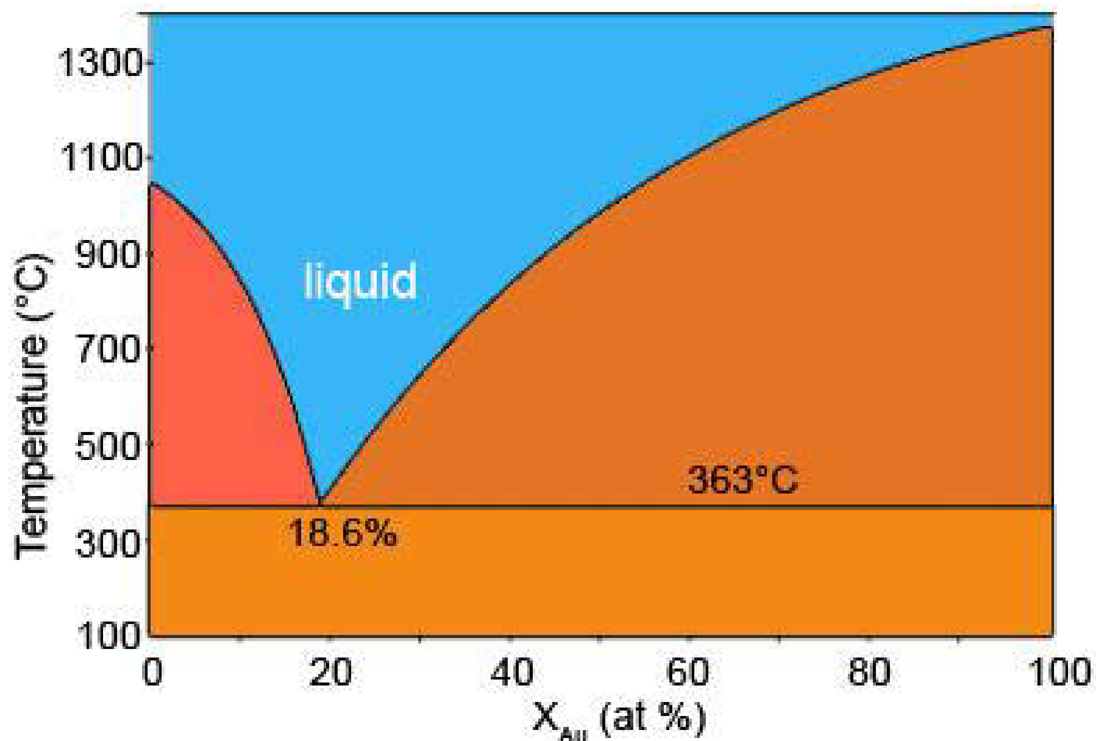

Figure 2.4 Au-Si phase diagram: under NW growth temperature top layers of Si substrate become Au-rich

The alternative way of the NW growth is the application of the self-assisted VLS growth which is widely applied nowadays. Many papers dedicated to the self-assisted growth mode of different materials have been published [20-22]. The published growth models are based on the supersaturation of crystal growth components in radial direction to make an axial one-dimensional structure. The method is realized by selective area epitaxy growth with the use of an oxide layer. The mask defines the locations of future NWs via predefined openings in the oxide layer. The growth occurs in a layer-by-layer mode along one dimension above the mask. The growth process is characterized by the formation of side facets with low surface energy [23]. If we consider III-V material systems, the catalysts particle consists of a group III material. Supersaturation leads to the growth at the particle-crystal interface.

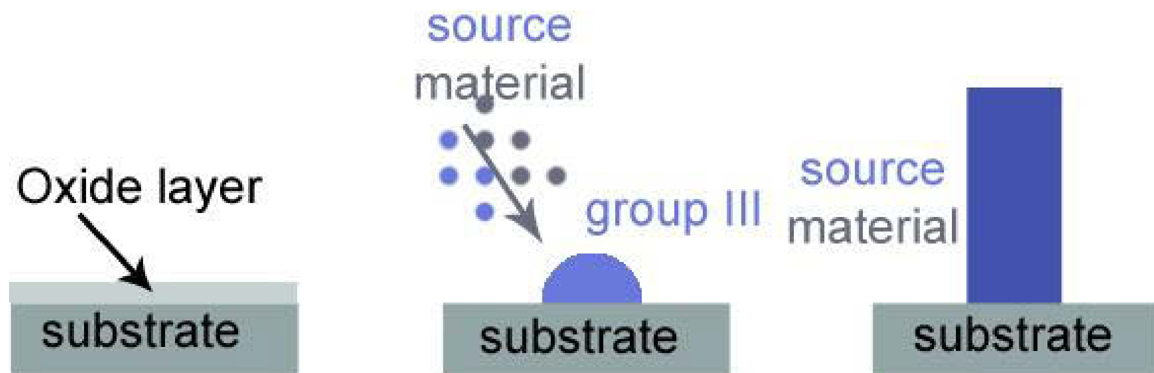

Figure 2.5 Growth scheme of self-assisted VLS growth

Fig. 2.5 shows a scheme of the self-assisted growth mechanism. The substrate covered with a coating layer is heated up to growth temperature of NW material. The oxide layer starts to evaporate and holes are forming in the oxide layer determining the locations for NW growth. The source material should be supplied in the correct sequence. First group III elements accumulate in the holes and create seeds. Then group V material should be supplied. After supersaturation of the catalyzes the growth process is starting. After the growth, fluxes of source components stop and the whole system cools down.

In this thesis, I characterize both types of growth in terms of growth components, chemical composition and defect structure. Au-assisted growth has been implemented in the metal organic vapor chamber epitaxy using GaAs [111] B substrate. Self-assisted growth was carried out in a molecular beam epitaxy chamber on a silicon substrate. The two growth techniques differ significantly. MBE growth does not require decomposition of metal-organic or hydride molecules. The growth occurs because of adatom diffusion on the substrate and the sidewalls of NW. The growth rate is determined by diffusion from the substrate surface, the top and sidewalls of the growing nanowires [24].

In case of MOVPE, growth takes much less time and growth rate may reach values of a few microns per hour. The construction of MOVPE chambers allows for multi-wafer growth i.e., the simultaneous use of several substrates. The growth process that occurs is thermodynamically more favorable compared to MBE [25]. But high pressure prohibits installation of electron gun for Reflection High Energy Electron Diffraction (RHEED) or others *in-situ* monitoring techniques. Atoms of source materials often remain at the chamber wall and memory effects become an issue.

2.3 Crystal phases of InAs

It was found that the properties of InAs may change on the nanoscale. In 1966 scientists from Tokyo Institute of Technology reported on the growth of InAs whiskers in wurtzite structures [26]. Bulk InAs exists in the cubic zinc-blende phase, but on the nanoscale the wurtzite phase becomes possible as well. A small number of reports is available today on structurally perfect NWs with only one structure phase [27, 28]. The structure of grown NWs strongly depends on the growth parameters, which opens the opportunity to develop NWs with zinc-blende, wurtzite or mixed phases. The dependence of the electronic band structure on the lattice structure allows for the formation of heterostructures formed by the same material, but different phases [29].

The cubic zinc-blende (ZB) structural phase is composed by two fcc lattices (face centered cubic) shifted by one quarter along the space diagonal (Fig. 2.6a). The cubic symmetry requires a=b=c and $\alpha=\beta=\gamma=90°$, where a, b, c are the lattice parameters and α, β, γ are the angles between the axis. The hexagonal wurtzite (WZ) structural phase is observed for most of semiconductors on nanoscale, which also exist in bulk in zinc-blende phase. In this case the lattice symmetry is described by $a=b\neq c$ and $\alpha=\beta=90°$, $\gamma\neq 90°$ (Fig. 2.6b).

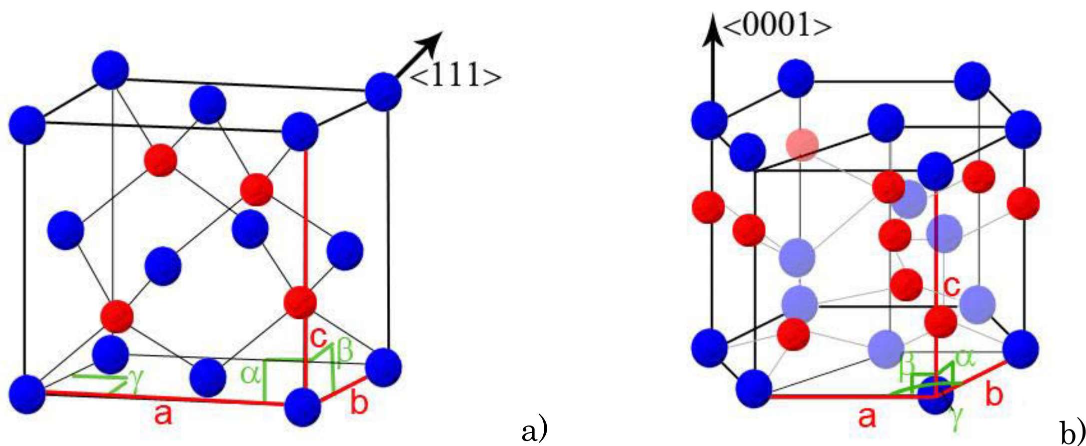

Figure 2.6 Unit cell of a) zinc-blende; b) wurtzite

The appearance of both phases for semiconductor nanorods is related to the direction in which most of the NWs grow. It is the <111> direction of the cubic cell, which is equal to the <0001> direction of the hexagonal system. The tetrahedral bonds between the nearest atoms are same for both structure types. The main difference of the two phases is the stacking sequences along the growth

direction. For ZB sequences three distinct layers of III-V pairs are repeated. The WZ phase is described by sequences of two layers of III-V pairs. The energetic difference is attributed to the difference in the third-nearest-neighbor spacing, which is shorter in the WZ structure compared to ZB one [30].

The stacking sequences along the growth direction are noted by 'ABC' letters. The ZB structure is characterized by three distinct layers, resulting in ABC sequences. In case of WZ structure, only two positions of the layer are possible, described by AB sequence. In literature, one finds notation with capital and small letters AaBbCc denoting stacking of cation and anion lattices. During crystal growth or under external influence, the sequences of layers can change. The deviation of stacking sequences from perfect 'ABCABC' for ZB to 'ABABAB' for WZ stacking is called stacking fault (SF). There are three kinds of SF: intrinsic (ISF), extrinsic (ESF) and twin defects (TW) (Fig. 2.7).

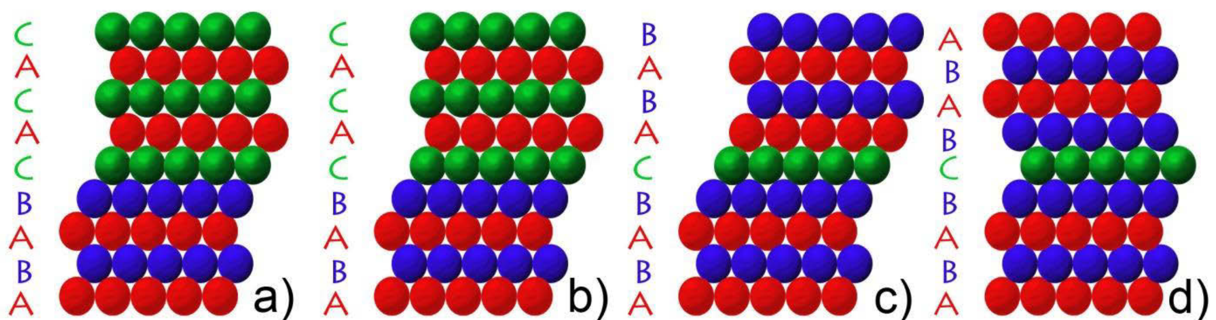

Figure 2.7 Typical stacking faults: a), b) intrinsic; c) extrinsic; d) twin defect

ISF happens when the sequence is changed by one of the stacking components. In notation of a WZ stack with 'ABAB' layers the sequence switches to 'ABABCACAC' or 'ABABCBCBC' as shown on Fig. 2.7 (a, b). The second type is ESF, it happens when an intervening layer C separates two vertical stacks. In letter notation it is written as 'ABABCABAB' (Fig. 2.7c). Twin defects happen when the ABC sequence is rotated by 180° with respect to the lower layers. Figure 3.3 shows an example of 'ABABCBABA' stack [31]. The stacking faults are non-desirable effect for electronics application. Structural defects become scattering centres for charge carriers leading to degradation of the device. One of the major problems to solve in nanowires growth is to decrease of the defects density and to achieve of defects-free growth and phase control with any kind of materials.

It was also shown that misfit dislocations play a crucial role in lattice relaxation between two mismatch materials (nanowire and the substrate). TEM

and XRD were used to characterize the realization of growth of GaAs nanowires on Si substrate (lattice mismatch 4%) [32].

As far as electrical and optical properties of NWs are crucially dependent on structural composition, phase purity, defect density *etc.* [33], investigation of growth process and growth parameters influence become a key for understanding and improvement of future devices. Most reports on structure and morphology of nanowires are based on SEM and TEM techniques results. SEM provides an images of the structure and can be used for morphology description. The internal structure can be inspected with TEM even on atomic scale, but the technique requires a complicated preparation procedure using focus ion beam, or other methods for localisation of single nano-object.

Alternatively, X-ray diffraction was successful in determination of shape, chemical composition and defect structure [32, 34, 35]. The technique allows ensemble as well as single nanostructure characterization (with the use of special focusing setups). The basic problem of X-ray scattering from nanostructures was in low scattering intensity from objects with a small amount of material. The problem was solved by opening new high-flux sources of synchrotron radiation and upgrading of existing X-ray sources. Using a nano-focused beam of such sources, the scattering signal is strong enough for detection and further evaluation for the NW structure. Using X-ray diffraction technique, one is able to detect and characterize the defect structure of the NWs system. The concentration of defects and the defect types can be investigated and described numerically.

Here, I demonstrate results of investigations of InAs NWs growth obtained by X-ray diffraction. Following questions that raise from preparation and growth modes will be solved in this thesis:

- composition and structural phase of growing system?
- temporal evolution of growing system during Au-catalysed growth?
- temporal evolution of growing system during self-assisted growth?
- investigation of defect structure of the MBE grown NWs?
- parasitic growth accompanying NWs growth?

In addition, we present a technique for description and numerical characterization of SF density in NWs. The methods are based on measurements of one particular sensitive to SF reflection and its simulation. Improvement of grown NWs will be achieved by understanding of a number of processes occurring during the growth.

References

[1] M. Passlack, OFF-state current limits of narrow bandgap MOSFETs, *Electron Devices, IEEE Transactions,* 53, 11, 2773-2778 (2006)

[2] P. Gaiduk, F. Komarov, V.Tishkov, W. Wesch, E. Wendler, *Physical Review B*, 61, 15785 (2000)

[3] V. Narayanan, S. Mahajan, N. Sukidi, K. J. Bachmann, V. Woods, N. Dietz, *Philasophical Magazine A,* 80, 555, (2000)

[4] S. Q. Wang, H. Q. Ye, *Journal of Physics of Condensed Matter*, 14, 9579 (2002)

[5] L. Chuang, F. Sedgwick, R. Chen, W. Ko, M. Moewe, K.Ng, T. Tran, C. Chang-Hasnain, *Nano Lett.* 11, 385, (2011)

[6] K. Tomioka, T. Fukui, *Appl. Phys. Lett.*, 98, 083114 (2011)

[7] M.Stiles,D. Hamann, *Phys Rev..B 38* , 2021-37 (1988)

[8] R. Wagner, W. Ellis, *Applied Physics Letters*,4(5): 89 (1964)

[9] H. J. Joyce, J.Wong-Leung,Q.Gao, H. Tan,C.Jagadish, *Nano Letters.*, 10 , 908 (2010)

[10] S. Hertenberger,D. Rudolph,S. Bolte,M. Döblinger,M. Bichler,D. Spirkoska,J. Finley,G. Abstreiter,G. Koblmüller ,*Applied Physics Letters* 98, 123114 (2011)

11] V.G. Weizer, N.S. Fatemi, *Journal of Applied Physics*, 64, 4618 (1988)

[12] J. Bauer PhD thesis „Metallorganische Gasphasenepitaxie von GaAs- und InAs-Nanodrahtstrukturen über den „vapor-liquid-solid“ - Wachstumsmechanismus“, Fakultät für Physik und Geowissenschaften der Universität Leipzig (2009)

[13] S. Kodambaka, J. Tersoff, M.C. Reuter, F.M. Ross, *Physical Review Letters*, 96, 096105 (2006)

[14] M.A. Verheijen, G. Immink, T. Desmet, M.T. Borgstro¨m, E.P.A.M. Bakkers, *Journalof the American ChemicalSociety*, 128, 1353 (2006)

[15] A.I. Persson, L.E. Fröberg, S. Jeppesen, M.T. Björk, L. Samuelson, *Journal of Applied Physics*, 101, 034313 (2007)

[16] H. Tuan, D. Lee, B.Korgel, *Angewandte Chemie International Edition*, 45, 5184 (2006)

[17] J. Bauer, V. Gottschalch, G. Wagner, *Journal of Applied Physics* 104, 114315 (2008)

[18] A. Lugstein,M. Steinmair,Y. J. Hyun,E. Bertagnolli, P. Pongratz, *Applied Physics Letters* 90, 023109 (2007)

[19] J. Lin, C. Chen, E. Diau, T. Liu, Journal of Materials Processing Technology, 206, 425 (2008)

[20] L. Gao, R. Woo, B. Liang, M. Pozuelo, S. Prikhodko, M. Jackson, N. Goel, M. Hudait, D. Huffaker, M. Goorsky, S. Kodambaka, R. Hicks, *Nano Letters*, 9 (6), 2223 (2009)

[21] W. Wei, X. Bao, C. Soci, Y. Ding, Z. Wang, D. Wang, *Nano Letters*, 9 (8), 2926–2934 (2009)

[22] K. Ikejiri, J. Noborisaka, S. Hara, J. Motohisa, T. Fukui, *Journal of Crystal Growth*, 298, 616 (2007)

[23] B. Mandl, J.Stangl, E. Hilner, A. Zakharov, K. Hillerich, A. Dey, L. Samuelson, G. Bauer, K. Deppert, A. Mikkelsen, *Nano Letters*, 10 (11), 4443 (2010)

[24] M. Tchernycheva, L. Travers, G. Patriarche, F. Glas, J.-C. Harmand G. Cirlin, V. Dubrovskii, Journal of Applied Physics, 102, 094313 (2007)

[25] P. Dapkus, *Journal of Crystal Growth*, 68, 345, (1984)

[26] K. Takahashi, T. Morizumi, *Japanese Journal of Applied Physics*, 5, 8, 657-662 (1966)

[27] Y. Kitauchi, Y. Kobayashi, K. Tomioka, S. Hara, K. Hiruma, T. Fukui, J. Motohisa, *Nano Letters*, 10, 1699 (2010)

[28] K. Dick, C. Thelander, L. Samuelson, P. Caroff, *Nano Letters*, 10, 3494 (2010)

[29] L. Zhang, W-J. Luo, A. Zunger, N. Akopian, V. Zwiller, J.-C. Harmand, *Nano Letters*, 10, 4055 (2010)

[30] K. Dick, P. Caroff, J. Bolinsson, M. Messing, J. Johansson, K. Deppert, R. Wallenberg, L. Samuelson, *Semicon Sci technol*, 25, 024009 (2010)

[31] M.Stiles, *Phys Rev..B 38*, 2021-37 (1988)

[32] A. Biermanns, S. Breuer, A. Trampert, A. Davydok, L. Geelhaar, U. Pietsch, *Nanotechnology*, 23 (30), 305703 (2012)

[33] C. Thelander, K . Dick, M. Borgström, L. Fröberg, P. Caroff, H. Nilsson, L. Samuelson, *Nanotechnology*, 21, 205703 (2010)

[34] A. Davydok, S. Breuer, A. Biermanns, L. Geelhaar, U. Pietsch, *Nanoscale Research Letters*, 7,109 (2012)

[35] D. Kriegner, C. Panse, B. Mandl, K. Dick, M. Keplinger, J. Persson , P. Caroff, D. Ercolani, L. Sorba, F. Bechstedt, J. Stangl, G. Bauer, *Nano Lett., 11* , 1483, (2011)

Chapter 3

X-ray Diffraction: Kinematical Scattering Theory

X-ray diffraction methods were used to analyse the structure of InAs NWs. The basic principal of scattering methods will be presented. The brief overview includes the elements of kinematic theory of X-ray diffraction, description of structural representation in X-ray diffraction experiments and overview of the X-ray coherence. We give a short explanation of the methodology and the fundamental concept of data evaluation used in this thesis. Based on this knowledge a computer software was developed for data simulations.

.

X-ray diffraction is a non-destructive method of crystal structure analysis, sensitive to sizes, composition and strain acting at the lattice. As visible light diffracts at a diffraction grating, X-rays diffract at a crystal lattice. The wavelength of X-ray is in the same order of magnitude as interatomic distance in a crystal (in order of angstroms). We focus on classical treatment of elastic Thomson scattering which is realized by placing the detector at a distance from the scattering object much larger then crystal lattice parameter. Inelastic Compton scattering was not taken to account. We also neglected multi-scattering effects and follow the kinematical approach of X-ray scattering theory. In order to describe scattering mathematically, we will discuss the key points of crystal representation and reciprocal space.

3.1 Crystal structure

By definition a crystal is formed by three-dimensional periodic repetition of atomic position along the axes. The smallest unit used for crystal representation is called unit cell. The unit cell is composed by the basis vectors of the crystal. The lengths of the vectors are the lattice parameters. The whole crystal is described by translation of atom in the direction of basis vector with periods defined by the lattice parameters.

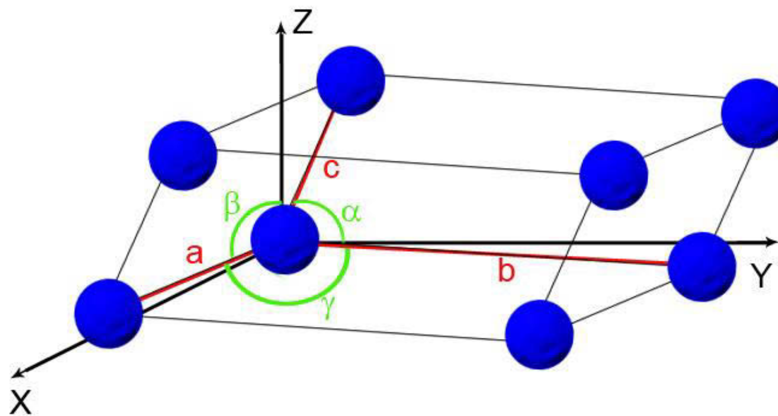

Figure 3.1 Unit cell with lattice parameters a, b, c and angles between basis vectors α, β, γ

Any position of atom in the lattice can be described using basis vectors as lattice parameters. For certain point R in the crystal one can write:

$$\vec{R} = \vec{a}u + \vec{b}v + \vec{c}w \qquad (3.1),$$

where a, b, c are three linear independent primitive vectors and u, v, w are integer numbers. Lattices described by equation (3.1) we called Bravias lattice. All possible variation of the atom arrangement two-dimensions were defined by five Bravias lattices, in three dimensions there are fourteen Bravias lattices.

3.2 Reciprocal space

In 1921 P. P. Ewald introduced the reciprocal lattice – a mathematical construction useful for crystal planes indexing and further description of scattering. One of the definitions for reciprocal lattice is the following: consider a plane wave e^{ikr}. It will only have the periodicity if the following condition is fulfilled for all vectors r

$$e^{(i\vec{k}(\vec{r}+\vec{R}))} = e^{(i\vec{k}\vec{r})} \quad \text{with} \quad e^{i\vec{k}\vec{R}} = 1 \qquad (3.2),$$

The set of all wavevectors in three dimensions, which gives a plane wave with periodicity R is called the reciprocal lattice. We label the reciprocal lattice vectors by $\vec{G}$ [1].

The basis vectors of the reciprocal lattice can be written as:

$$\begin{array}{lll} \vec{a} \cdot \vec{a}^* = 2\pi & \vec{b} \cdot \overrightarrow{b^*} = 2\pi & \overrightarrow{c} \cdot \overrightarrow{c^*} = 2\pi \\ \vec{b} \cdot \overrightarrow{a^*} = 0 & \vec{a} \cdot \overrightarrow{b^*} = 0 & \vec{a} \cdot \overrightarrow{c^*} = 0 \\ \vec{c} \cdot \overrightarrow{a^*} = 0 & \vec{c} \cdot \overrightarrow{b^*} = 0 & \vec{b} \cdot \overrightarrow{c^*} = 0 \end{array} \qquad (3.3)$$

Solutions of the system of equations are:

$$\overrightarrow{a^*} = \frac{2\pi}{V} \cdot \vec{b} \times \vec{c} \quad \overrightarrow{b^*} = \frac{2\pi}{V} \cdot \vec{a} \times \vec{c} \quad \overrightarrow{c^*} = \frac{2\pi}{V} \cdot \vec{a} \times \vec{b} \qquad (3.4),$$

where $V = \vec{a} \cdot (\vec{b} \times \vec{c})$defines the volume of unit cell. As far the crystal is a periodic system of the atoms, the reciprocal lattice can be obtained by Fourier transformation of the real crystal lattice. In this case the vector of a certain lattice plane is normalized

$$\vec{N} = \frac{1}{2\pi} \cdot (n_1\overrightarrow{a^*} + n_2\overrightarrow{b^*} + n_3\overrightarrow{c^*}) \qquad (3.5)$$

and the distance of the lattice plane from origin is defined by:

$$D = \vec{N}\vec{R} = n_1 u + n_2 v + n_3 w \qquad (3.6)$$

where R is formed by equation (3.1). If a lattice plane crosses the coordinates axis in the points a_0, b_0, c_0 equation (3.6) can be rewritten by

$$D = n_1 \cdot \overrightarrow{a_0} = n_2 \cdot \overrightarrow{b_0} = n_3 \cdot \overrightarrow{c_0} \qquad (3.7)$$

Based on equations (3.5) and (3.6) we can write the lattice plane equation:

$$hu + kv + lw = m \qquad (3.8)$$

where h, k, l are integer. With certain suitable values of m, h, k, l define as:

$$h = \frac{m}{\overrightarrow{a_0}}, \quad k = \frac{m}{\overrightarrow{b_0}}, \quad l = \frac{m}{\overrightarrow{c_0}}$$

Using these equations, we can write the reciprocal lattice vector, which is along perpendicular to the real lattice by:

$$\vec{G} = h \cdot \overrightarrow{a^*} + k \cdot \overrightarrow{b^*} + l \cdot \overrightarrow{c^*} \qquad (3.9)$$

where (h, k, l) are called Miller's indices.

With the help of the equation (3.9), we can define the angle between two lattice planes as the angle between corresponding normal's to these planes by:

$$\cos\psi = \frac{\overrightarrow{G_1} \cdot \overrightarrow{G_2}}{G_1 G_2} \qquad (3.10)$$

Moreover, we may calculate the distance between two neighboured lattice planes of the same orientation by:

$$d_{hkl}^2 = \frac{1}{|\vec{G}_{hkl}^2|} = \frac{1}{(h \cdot \overrightarrow{a^*} + k \cdot \overrightarrow{b^*} + l \cdot \overrightarrow{c^*})^2} \qquad (3.11)$$

In such a way, the real space distances are connected with reciprocal space interpretation. If we consider a denominator of the right part of the equation:

$$\left(h \cdot \vec{a}^* + k \cdot \vec{b}^* + l \cdot \vec{c}^*\right)^2 = \left(h \cdot \vec{a}^* + k \cdot \vec{b}^* + l \cdot \vec{c}^*\right) \cdot \left(h \cdot \vec{a}^* + k \cdot \vec{b}^* + l \cdot \vec{c}^*\right) =$$

$$h^2 \cdot \vec{a}^{*2} + k \cdot \vec{b}^{*2} + l \cdot \vec{c}^{*2} + 2kl \cdot \vec{b}^* \cdot \vec{c}^* + 2lh \cdot \vec{c}^* \cdot \vec{a}^* + 2hk \cdot \vec{a}^* \cdot \vec{b}^* =$$

$$= h^2 \cdot \vec{a}^{*2} + k \cdot \vec{b}^{*2} + l \cdot \vec{c}^{*2} + 2klb^*c^* \cos\alpha^* + 2lhb^*c^* \cos\beta^* + 2hka^*b^* \cos\gamma^*$$

The interplanar distance can be evaluated through the parameters of the direct lattice by substituting for the magnitudes a^*, b^* and c^* and for $cos\alpha^*$, $cos\ \beta^*$ and $cos\ \gamma^*$ in these two equations. Considering the specifics of crystal system we can calculate interplanar distance for cubic and hexagonal structure. In case of cubic lattice $\alpha^* = \beta^* = \gamma^* = 90^\circ$ and $a^* = b^* = c^* = \frac{1}{a}$, we obtain: ${d_{hkl}}^2 = \frac{a^2}{h^2+k^2+l^2}$. For hexagonal one: $\alpha^* = \beta^* = 90^\circ$; $\gamma^* = 60^\circ$; $a^* = b^* = \frac{2}{a\sqrt{3}}$; $c^* = \frac{1}{c}$, which gives ${d_{hkl}}^2 = \frac{a^2}{\frac{4}{3}(h^2+k^2+hk)+(l\frac{a}{c})^2}$.

3.3 X-ray diffraction on crystal

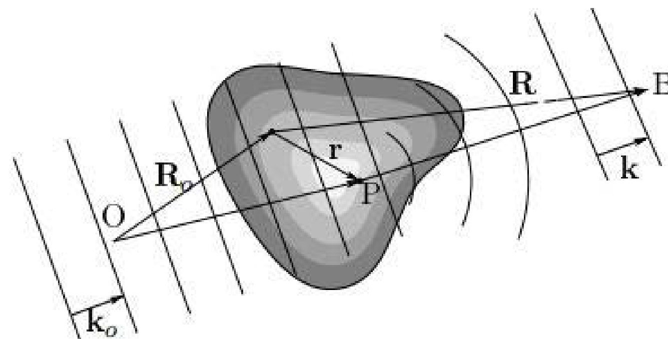

Figure 3.2 Diffraction scheme on the crystal: O – source of radiation; B- observed point; P – point in the crystal

Using the kinematical scattering theory X-ray diffraction at crystals can be subdivided in two processes: scattering of photons at atomic electrons and interference of these scattered waves at the position of detector. In other words, the incoming plane wave originates oscillations of atomic electrons with the same frequency as the incident wave has. These oscillation leads to emission of a spherical wave. The incoming wave is characterized by its wavevector $\vec{k}_0$ by $|\vec{k}_0| = k = \frac{2\pi}{\lambda}$. The superposition of all scattered waves creates a signal at the point of observation. The direction of a scattered wave is defined by the wavevector $\vec{k_f}$. At a certain point in matter (point P – Fig. 3.2) the amplitude of the incoming wave is:

$$A_P(\vec{r},t) = A_0 e^{i\vec{k}_0(\overrightarrow{R_0}+\vec{r}) - i\omega_0 t} \qquad (3.12)$$

here, $\overrightarrow{R_0}$ is the vector from origin to the sample, $\vec{r}$ –distance vector from R_0 to the scattering point R (Fig. 3.2). At this point an electron is exited and emits a wave with probability f. The outgoing amplitude at the observing point can be written as:

$$A_{op} = A_p(\vec{r},t) \cdot f \cdot \frac{e^{ik(\vec{R}-\vec{r})}}{R} \qquad (3.13),$$

where R defines the distance from leading vector to the observed point. The amplitude can be calculated by considering the total scattering volume of the scattered crystal. The integration should include the volume of the crystal and the number of scattering centres for photons. These factors were considered by the electron density distribution $\rho(r)$. The electron density is a probability of electron presence at a defined location in real space. One should mentioned that discussed scheme is valid for the far-field limit only. As mentioned on the beginning of the chapter we discuss Thompson scattering.

In a real experiment with a real detector the intensity is a measurable quantity and can be calculated by:

$$I_{op}^{TOT} = \frac{A_0^2}{R^2} \cdot f^2 \cdot \left| \int \rho(\vec{r}) e^{i(\overrightarrow{k_0}-\vec{k})\vec{r}} d^3r \right|^2 \qquad (3.14)$$

Crystal lattice is defined by the periodicity of electron density distribution. In such away, one can connect with the reciprocal lattice description by:

$$\rho(\vec{r}) = \sum_{\vec{G}} \rho_{\vec{G}} e^{i\vec{G}\vec{r}} \qquad \text{or} \qquad \rho_{\vec{G}} = \frac{1}{V} \cdot \int \rho(\vec{r}) \cdot e^{-i\vec{G}\vec{r}}\, d^3r \quad (3.15)$$

We can define the conditions for diffraction in a crystal. The scattering intensity will be 0 for all q, except $q = G$, which gives scattering volume:

$$\int \rho(\vec{r}) e^{i(\vec{k}_0-\vec{k})\vec{r}} d^3r = V \qquad (3.16)$$

This defines the condition of constructive interference of all outgoing spherical waves at the point of observation in sample coordinates:

$$q = k - k_0 = G \qquad (3.17)$$

So the measured intensity in the observing point can be defined by:

$$I_{op}^{TOT} = \frac{A_0^2}{R^2} \cdot N^2 \cdot f^2 \cdot \left|\rho_{\vec{q}}\right|^2 \qquad (3.18)$$

3.4 The Laue equations and Bragg interpretation of diffraction conditions

Considering equation (3.17) for the three basic vectors a, b, c, one obtains the Laue equations:

$$\vec{a} \cdot (\vec{k} - \overrightarrow{k_0}) = 2\pi h \qquad \overrightarrow{b} \cdot (\vec{k} - \overrightarrow{k_0}) = 2\pi k \qquad \vec{c} \cdot (\vec{k} - \overrightarrow{k_0}) = 2\pi l \quad (3.19)$$

Since the wavevector depends on wavelength of the radiation and the equations contain three indexes of certain reflection we obtain three equations with three unknown values. The h, k, l are integer numbers and are connected by: $h = \frac{\Delta\vec{k}\cdot\vec{a}}{\Delta\vec{k}\cdot\vec{c}} \cdot l$ and $k = \frac{\Delta\vec{k}\cdot\vec{b}}{\Delta\vec{k}\cdot\vec{c}} \cdot l$. With this information one is able to determine the reflection indexes and wavelength of radiation used in the experiment.

The conditions shown in equation (3.17) are interpreted as lattice planes. In crystal the X-ray behaves like an optic beam in atmosphere. So it obeys optical laws, in this case the process of diffraction can be described by the difference in optical path lengths through the crystal. It should be equal to an integer number of the wavelength. This condition for interference can be written as:

$$m \cdot \lambda = \Delta r = 2d_{hkl} \sin\theta \qquad (3.20)$$

where d_{hkl} is the distance between two lattice planes introduced in (3.9), m is an integer and defines the order of interference.

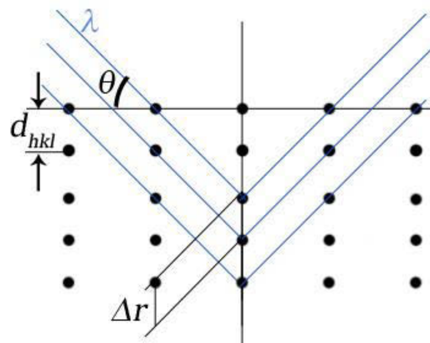

Figure 3.3 Bragg interference conditions

It should be taken into account that the transition from constructive to destructive interference is gradual with the change of the incident angle.

Combining angular conditions with reciprocal space, we consider that the scanning parameter can be the incident or exit wave vectors depending on setups (angular- or energy-dispersive). The simple relationship between diffraction angle θ and reciprocal space is:

$$|\vec{q}| = \frac{4\pi \cdot \sin\theta}{\lambda} \qquad (3.21)$$

3.5 Lattice sum and Laue conditions

For calculation of scattered intensity we use the term lattice sum. It is a sum of complex terms corresponding to the points located on the unit circle. The lattice sum is the sum of a large amount of terms (in case of cubic crystal with size 1x1x1μm^3, number of terms equals to 10^{12}). From statistics we know when one adds a large number of random terms, the sum will be equal to zero. The atoms not in phase produce destructive interference. When $e^{i\vec{G}\vec{R}} = 1$ for all $\vec{R}$, the sum is N, a large number. This holds that if G is a reciprocal lattice vector H:

$$\vec{G} = \vec{H} \qquad (3.22)$$

The Laue conditions for scattering from a crystal are equivalent to Bragg's law.

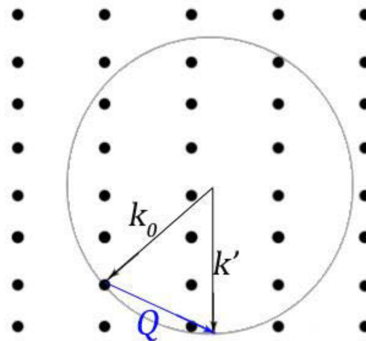

Figure 3.4 Ewald's circle (2D case of a sphere) with fulfilled Laue diffraction conditions when points located on circle.

For visualisation of the diffraction conditions defined in (3.17), one can use a specific construction called Ewald's sphere. The radius of the sphere depends on the length of the wavevector, which goes through the origin. Plotting the

wavevectors for the case of elastic scattering the following condition should be fulfilled: $\vec{G} = \overrightarrow{k_0} - \overrightarrow{k'}$. In other words, respective reciprocal lattice points lie on Ewald's sphere. Example on Ewald's circle is shown in fig. 3.4. It is useful to calculate the lattice sum explicitly and we write $\vec{R} = n_1\overrightarrow{a_1} + n_2\overrightarrow{a_2} + n_3\overrightarrow{a_3}$; $\vec{G} = h\overrightarrow{b_1} + k\overrightarrow{b_2} + l\overrightarrow{b_3}$ and use definition of delta-function:

$$S_n(\vec{G}) = \sum_{R_n} e^{i\vec{G}\cdot\vec{R}_n} \sum_{n_1} e^{i2\pi h n_1} \sum_{n_2} e^{i2\pi k n_2} \sum_{n_3} e^{i2\pi l n_3} \tag{3.23}$$

For the calculation of the lattice sum, we use equation (3.1) and (3.9). The finite size of the crystal can be described with presentation of the crystal as parallelepiped with basis vectors. Consider sums in (3.23) as geometric progression using values from 0 to N-1 unit cells, it becomes:

$$S_u(h) = \sum_0^{N-1} e^{i2\pi h u} = \frac{1-e^{i2\pi N h}}{1-e^{i2\pi h}} = \frac{\sin \pi N h}{\sin \pi h} e^{i\pi(N-1)h} \tag{3.24}$$

The measured intensity is proportional to the square of the lattice sum. In other words, we can rewrite the measured intensity as:

$$I^{TOT} \sim |S_u(h)|^2 = \frac{\sin^2(\pi N h)}{\sin^2(\pi h)} \tag{3.25}$$

where N is the total number of unit cells in the crystal.

3.6 Atomic form factor and structure factor

The scattering intensity calculated in (3.18) is defined by the square of Fourier transformation of components of electron density distribution ρ_G. In this case, constructive interference is observed only at reciprocal lattice vectors G. The electron density calculation for the unit cell is shown in (3.15). The total density can be represented by the sum of electron density of all atoms within the unit cell located at the relative coordinates r_a:

$$\rho_G = \frac{1}{V_{cell}} \int \sum_a \rho(\vec{r}_a + \vec{r}') \cdot e^{-i\vec{G}\cdot\overrightarrow{r'} - i\vec{G}\cdot\vec{r}_a} \, d^3r' = \tag{3.26}$$

$$= \frac{1}{V} \sum_a e^{-i\overrightarrow{G}\cdot\overrightarrow{r_a}} \cdot \int \rho_a(\overrightarrow{r'}) \cdot e^{-i\overrightarrow{G}\cdot\overrightarrow{r'}} d^3\, r'$$

where $\vec{r} = \vec{r_a} + \vec{r}\,'$ defines the distance from origin of the atomic coordinates to a certain point. The integral $f_a = \int \rho_a(r') \cdot e^{-iqr'} d^3 r'$ is the atomic scattering factor. It depends on chemical composition and reciprocal lattice vector q. The atomic form factor can be calculated for an angle θ between $\vec{q}$ and $\vec{r}\,'$:

$$f_a = \int \rho_a(\vec{r}\,')e^{-i\vec{q}\vec{r}'}d^3r' = -2\pi \int_0^\infty \int_{-1}^{1} \rho_a(\vec{r}\,')e^{-iGr'\cdot\cos\theta}\, r'^2 d' d\cos\theta =$$

$$= 4\pi \int_0^\infty \rho_a(r') \cdot r'^2 \cdot \frac{\sin(q\cdot r')}{q\cdot r'} dr' \qquad (3.27)$$

Using this, one can write an equation for the structural factor:

$$F(G) = \int_{j=1}^{unit\ cell} f_j e^{iGr_j} dr \qquad (3.28)$$

The measured intensity is proportional to square of scattering amplitude, when the amplitude is defined by phase sum of atomic scattering factor. The presented calculations define the extinction rules for any structure type. The rules describe conditions to find a Bragg-reflection with non-zero intensity for a certain lattice.

3.7 Crystal truncation rods

Our experiments are dedicated to structure investigation of nano-size wires grown on the millimetre-size substrate. Here an important role plays the surface effects and high surface/bulk ratio. The scattering of X-rays is also sensitive to such influence. As shown in [2] integral across all crystal equals:

$$F(\vec{G}) = F^{uc}(\vec{G}) \cdot \int \rho_\infty(\vec{r}) s(\vec{r}) e^{i\vec{G}\cdot\vec{r}}\, d\vec{r} \qquad (3.29)$$

where $F^{uc}(G)$ is the structure factor of the unit cell, $s(r)$ is the shape function to be zero outside the crystal and $\rho_\infty = \sum_{n=1}^{\infty} \delta(r-R)_n$. Using inside the convolution theorem:

$$F(\vec{G}) = \frac{F^{uc}(\vec{G})}{(2\pi)^3} \int \rho_\infty(\vec{G}')s(\vec{G} - \vec{G}')d\vec{G}' \qquad (3.30)$$

The shape function is defined as Fourier transform:

$$s(\vec{G}) = \int s(\vec{r})e^{i\vec{G}\cdot\vec{r}}\, d\vec{r} \qquad (3.31)$$

and

$$\rho_\infty(\vec{G}) = \int \rho_\infty(\vec{r})e^{i\vec{G}\cdot\vec{r}}d\vec{r} = \sum_n e^{i\vec{G}\cdot\vec{R}_n} = \sum_n \delta(\vec{G} - \vec{H}_n) \qquad (3.32)$$

Using presented ratios we rewrite

$$F(\vec{G}) = \frac{F^{uc}(\vec{G})}{(2\pi)^3} \sum_n s(\vec{G} - \vec{H}_n) \qquad (3.33)$$

At the position of Bragg reflection $\vec{G} \approx \vec{H} = \vec{H}_n$ and with $\vec{q} = \vec{G} - \vec{H}$we can write:

$$F(\vec{q}) = \int s(\vec{r})e^{i\vec{q}\cdot\vec{r}}\, d\vec{r} \qquad (3.34)$$

Here, we received the lattice part of the structure factor at the Bragg point. The shape of the crystal is represented by the shape function $s(r)$. Using the Gaussian divergence theorem and consider the structure factor as volume integral, we get:

$$F(\vec{q}) = \frac{i}{q^2}\vec{q} \cdot \vec{n} \cdot \int_S \; e^{-i\vec{q}\cdot\vec{r}}dS \qquad (3.35)$$

where n is normal to surface element dS. The structure factor equation shows that strongest scattering will be observed for reciprocal vectors parallel to surface normal n. In case of samples with facets, strong scattering occur towards a direction perpendicular to facets of the crystal. The streaks appearing from Bragg reflections along the crystal surface normal are known as crystal truncation rods (CTRs) because the signal appears from truncation of three dimension periodicity of the crystal by the surface. The CTRs concept is widely used for surface investigations or for small size crystals grown on substrate. In (3.35) intensity decays by $\frac{1}{q^2}$ from Bragg reflection. The example of small crystal measurements is shown in [3].

3.8 X-ray diffraction from zinc-blende and wurtzite structures

As was mentioned in Chapter 2, semiconductor NWs may grow in two structure phases – zinc-blende and wurtzite. In most cases NW growths is realized along <111> direction of semiconductor ZB substrate which equal to <0001> of WZ phase. During the X-ray diffraction experiment, one often faces the problem that a Bragg reflection is measured from a mixed phases of ZB and WZ phases. To overcome the problem a specific coordinate system is used to describe the X-ray diffraction experiment, the surface coordinate system.

We consider (111) surface of a ZB crystal. Most of the semiconductor materials exhibit zinc-blende structure in bulk. The ZB unit cell consists of two fcc lattices and one of both is shifted by one quarter along the space diagonal of the ZB cell. As far as NWs grow in [111] direction, it is useful to chose one coordinate axis along the [111] direction and two in-plane vectors perpendicular. This coordinate system is often used in surface physics [4], with cubic lattice parameter a_0 , are given by

$$\vec{a} = \left(\frac{a_0}{2}\right)(\vec{x} - \vec{z})$$

$$\vec{b} = \left(\frac{a_0}{2}\right)(-\vec{x} + \vec{y}) \qquad (3.36)$$

$$\vec{c} = a_0(\vec{x} + \vec{y} + \vec{z})$$

For hexoganl system one can write these values as $\vec{a} = \vec{b} = \frac{a}{\sqrt{2}}; \vec{c} = \sqrt{3}a_0$ with the angles $(\widehat{\vec{a},\vec{b}}) = 120°$; $(\widehat{\vec{a},\vec{c}}) = (\widehat{\vec{b},\vec{c}}) = 90°$

The corresponding reciprocal vectors are:

$$\overrightarrow{a^*} = \frac{4\pi}{3a_0}(\vec{x} + \vec{y} - 2\vec{z});\ \overrightarrow{b^*} = \frac{4\pi}{3a_0}(\overrightarrow{-x} + \overrightarrow{2y} - \vec{z});\ \overrightarrow{c^*} = \frac{2\pi}{3a_0}(\vec{x} + \overrightarrow{y+z}) \qquad (3.37)$$

These vectors used for a hexagonal system with $\overrightarrow{a^*} = \overrightarrow{b^*} = \frac{4\pi}{a_{0}{}_0}\sqrt{\frac{2}{3}}$; $\overrightarrow{c^*} = \frac{2\pi}{\sqrt{3}a_0}$ and with the angles $(\widehat{\overrightarrow{a^*}\overrightarrow{b^*}}) = 60°$; $(\widehat{\overrightarrow{a^*}\overrightarrow{c^*}}) = (\widehat{\overrightarrow{b^*}\overrightarrow{c^*}}) = 90°$. For surface system, we mark the coordinates with bottom index s. In surface coordinate the basis vectors of fcc lattice are:

$$\overrightarrow{r_1} = [0,0,0]_s;\quad \overrightarrow{r_2} = \left[\frac{2}{3},\frac{1}{3},\frac{1}{3}\right]_s;\ \overrightarrow{r_3} = \left[\frac{1}{3},\frac{2}{3},\frac{2}{3}\right]_s \qquad (3.38)$$

Follow equation (3.38) structure factor of fcc unit cell defines as:

$$F_S^{fcc}(\vec{G}) = \sum_{r_1} e^{i\vec{G}\cdot\vec{r}_1} = 1 + e^{i\left(\frac{2\pi}{3}\right)(2h+k+l)} + (e^{i\left(\frac{2\pi}{3}\right)(2h+k+l)})^2 =$$

$$= \begin{cases} 3 \; for \; 2h+k+l = 3i, & i \in Z \\ 0 \end{cases}$$

This is an example of extinction rules mentioned before in subchapter 3.6. It shows conditions that the measured intensity is non-zero and Bragg reflection can be observed. Also, we would like to stress on a case of twins defects (Chapter 2), following an ABC stack is rotated around [111] direction by 60°. For this case, extinction rule contains the indices h and k

$$h + 2k + l = 3i, \qquad i \in Z$$

For InAs the atoms occupy the follow positions of fcc lattice:

$$In: \quad [0,0,0]_s \qquad As: \quad [\frac{1}{4},\frac{1}{4},\frac{1}{4}]_s$$

The structure factor of InAs in surface coordinates is:

$$F_S^{InAs}(\vec{G}) = f_{In}(\vec{G}) \cdot F_S^{fcc}(\vec{G}) + f_{As}(\vec{G}) \cdot F_S^{fcc}(\vec{G}) \cdot e^{i\pi\frac{l}{2}} \qquad (3.39)$$

Here, we express the structure factor by atomic form factors of In and As with certain values of l =2, 6, 10…. Now we can estimate which reflections are forbidden. The reflections with low value of in structure factor is zero or very small.

The zinc-blende structure can be represented also as stacking of hexagonally closed packed bilayers. Zinc-blende is characterized by stacking sequence ABC. Twin defects rotated for 60 degrees around [111] direction are described by ACB stacking. Using this notation, different structures can be described. In addition to ZB structure phase, in semiconductor nanowires the wurtzite structure is observed with stacking sequence AB. For this phase, the basis in with cubic lattice parameter is described by (3.36).

In surface coordinates, we rewrite the out-of-plane vector $[111]_c$ to $\left[\frac{2}{3},\frac{2}{3},\frac{2}{3}\right]_c$. It does not change along in-plane reciprocal vectors but has an effect for out-of-

plane vector c^*: $\frac{3c^*}{2} = \left[\frac{1}{2}, \frac{1}{2}, \frac{1}{2}\right]_c$. Following this logic, any stacking sequence can be described and explained including sequences with stacking faults. For example, the basis of a wurtzite configuration is represented by $c \rightarrow 2c$ and the out-of-plane lattice parameter is written as $\frac{c^*}{2}$ [5]. Often structures are described by a ratio of out-of-plane and in-plane parameters c/a. For ideal hexagonal close packed lattice this ratio equal to $\frac{c}{a} = \sqrt{\frac{8}{3}}$ and refer to the optimum packing factor 0.74. In this case the basis is described by:

$$In: \quad \overrightarrow{a_1^*} = \frac{1}{3}\vec{a} + \frac{2}{3}\vec{b} \qquad \overrightarrow{b_1^*} = \frac{2}{3}\vec{a} + \frac{1}{3}\vec{b} + \frac{1}{2}\vec{c}$$

$$As: \quad \overrightarrow{a_2^*} = \frac{1}{3}\vec{a} + \frac{2}{3}\vec{b} + \frac{3}{8}\vec{c} \qquad \overrightarrow{b_2^*} = \frac{2}{3}\vec{a} + \frac{1}{3}\vec{b} + \frac{7}{8}\vec{c}$$

Using this basis, one can calculate structure factor of hexagonal close pack structure:

$$F_{hcp}(\vec{G}) = \sum_{r_1} e^{i\vec{G}\cdot\vec{r}_1} = 1 + e^{i\left(\frac{2\pi}{3}\right)(2h+k)} e^{i\pi l_w} \tag{3.40}$$

$$0 \quad \text{for } l_w \text{ odd} \quad \text{and } 2h + k = 3i, \quad i \in Z$$

where $l_w = \frac{2l_s}{3}$. From here we can define forbidden reflections of WZ phase. The conditions are fulfilled when l_w =4, 12, 20… . Many papers have shown that the c/a ratio in a real case of InAs nanowires is different from the ideal value [6, 7]. For real experiments it is much more comfortable to use one coordinate system for measured reflections for both types of crystal phases. For this case we use transformation matrices from cubic system to hexagonal one, with the notations a_c for cubic lattice parameters and a_h and c_h for hexagonal lattice parameters

$$\begin{pmatrix} x \\ y \\ z \end{pmatrix}_c = \begin{pmatrix} \frac{\sqrt{2}a_c}{3a_h} & \frac{\sqrt{2}a_c}{3a_h} & -\frac{2\sqrt{2}a_c}{3a_h} \\ -\frac{\sqrt{2}a_c}{3a_h} & \frac{2\sqrt{2}a_c}{3a_h} & -\frac{\sqrt{2}a_c}{3a_h} \\ \frac{a_c}{\sqrt{3}c_h} & \frac{a_c}{\sqrt{3}c_h} & \frac{a_c}{\sqrt{3}c_h} \end{pmatrix} \begin{pmatrix} x \\ y \\ z \end{pmatrix}_h$$

and in reciprocal space will be:

$$\begin{pmatrix} h \\ k \\ l \end{pmatrix}_c = \begin{pmatrix} \frac{a_h}{\sqrt{2}a_c} & 0 & -\frac{a_h}{\sqrt{2}a_c} \\ -\frac{a_h}{\sqrt{2}a_c} & \frac{a_h}{\sqrt{2}a_c} & 0 \\ \frac{c_h}{\sqrt{3}a_c} & \frac{c_h}{\sqrt{3}a_c} & \frac{c_h}{\sqrt{3}a_c} \end{pmatrix} \begin{pmatrix} h \\ k \\ l \end{pmatrix}_h$$

In the results of the calculations we demonstrate one example of [10L] and [11L] rod calculated for InAs, which contain three types of reflections – ZB, WZ and reflections from twin defects.

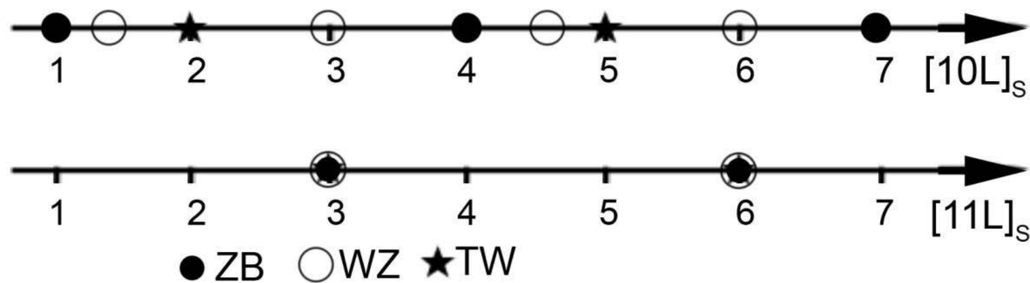

Figure 3.5 [10L]s and [11L]s rods in surface coordinates as function of L with reflections of the different structural configurations

The described transformation from cubic system to the hexagonal one in surface coordinate system is show for [10L]s and [11L]s rods (fig. 3.5). The [10L]s rod is perpendicular to (111) oriented surface. The allowed reflections for ZB phase are marked by filled circles, for WZ phase by empty circles and reflections appeared due to twin defects are marked by stars. All these reflections have the same in-plane lattice parameter for a certain rod. It makes it possible experimentally to get access to reflections unique for a certain phase and to perform phase analyzes of the system. Also, via structure factor calculations, sensitive reflections to different kinds of plane defects can be defined.

3.9 Coherence of X-ray beam

Up to this subchapter we presented the X-ray beam as perfect plane wave. During real experiments this assumption is not fully true and some deviations from the perfect case are possible. The deviations can be of two types: the X-ray beam is not perfectly monochromatic and the beam does not propagate entirely in

the defined direction. Consider this, the X-ray beam can be characterized in terms of the coherence length concept.

Let's imagine two waves are exactly in phase at certain point, propagating in the same direction but with slightly different wavelengths (λ and $\lambda - \Delta\lambda$). The longitudinal coherence length defines the distance where the waves become out of phase. We denote this distance L_L. After passing L_L the waves are out of phase, they come again in phase after travelling $2L_L$. If we define this distance equal to $N\lambda$ or equal $(N+1)(\lambda - \Delta\lambda)$, it because:

$$2L_L = N\lambda = (N+1)(\lambda - \Delta\lambda) \tag{3.41}$$

Replacing $(N+1)\Delta\lambda = \lambda$. We can rewrite the equation as:

$$L_L = \frac{1}{2}\frac{\lambda^2}{\Delta\lambda} \tag{3.42}$$

Now we consider two waves with equal wavelengths but a bit different directions defined by an angle $\Delta\theta$ (Fig. 3.6). The distance, through which both wavefronts become out of phase, is call transverse coherent length L_T. Following the assumption that at some distance the waves become in phase again and using the same replacement as used above with example of longitudinal coherent length, we can write: $L_T = \frac{\lambda}{(2\Delta\theta)}$. If we discuss two waves with slightly different direction emitted by the same source, we suppose that both waves come from different points of the source, separated by the distance D. The distance between the observed point and the source we denote with R and based on geometry shown at fig. 3.6, it becomes: $L_T = \frac{\lambda}{2}\frac{R}{D}$.

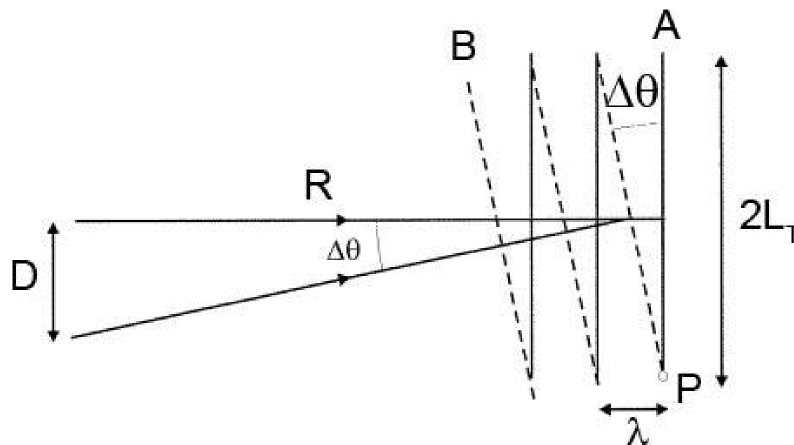

Figure 3.6 Two waves with equal wavelength emitted by source of size D

For real experiments the coherence lengths of beam are important parameters. For example, if we consider two electrons separated by a distance larger than the coherence length then the total scattered intensity is defined by sum of scattering intensities from the individual objects. The coherence length of the beams is also defined by experimental setups. The type of synchrotron radiation source and monochromator are key point in optimization of beam quality. Also the geometry of the experiment plays an important role for the value of coherent length of the beam.

3.10 Reciprocal space coordinates

In the next chapters experimental results and its interpretation are described. For sake of comparison of the experiments all angular coordinates were transformed into wavelength independent reciprocal space coordinates using the relations:

$$q_x = \frac{2\pi}{\lambda}\left(\cos(\alpha_f) - \cos(\alpha_i)\right)$$

$$q_y = \frac{2\pi}{\lambda}\sin(\theta) \qquad (3.43)$$

$$q_z = \frac{2\pi}{\lambda}\left(\sin(\alpha_f) + \sin(\alpha_i)\right)$$

where $\alpha_{i,f}$ are the incidence and exit angle with respect to (111) lattice planes, respectively θ - scattering angle in the detector plane perpendicular to α_f.

References

[1] Ashcroft and Mermin, Solid State Physics, Stratford Books, 1976

[2] A. Vartanyants and I. K. Robinson. Partial coherence effects on the imaging of small crystals using coherent x-ray diffraction. J. Phys.-Condes. Matter, 13:10593–10611, 2001.

[3] I. A. Vartanyants, A. V. Zozulya, K. Mundboth, O. M. Yefanov, M.-I. Richard, E. Wintersberger, J. Stangl, A. Diaz, C. Mocuta, T. H. Metzger, G. Bauer, T. Boeck, and M. Schmidbauer. Crystal truncation planes revealed by three-dimensional reconstruction of reciprocal space. Phys. Rev. B, 77:115317, 2008.

[4] V. Vonk, J. Huijben, D. Kukuruznyak, A. Stierle, H. Hilgenkamp, A. Brinkman, and S. Harkema, Phys. Rev. B 85 045401 (2012)

[5] S. Mariager, PhD thesis „Structure and dynamics of crystalline nano-systems“,University of Copenhagen, 2010

[6] H.Shu, X, Chen, H. Zhao, H. Zhou, W.Lu *J. Phys. Chem. C*, 2010, 114 (41), pp 17514–17518

[7] D. Kriegner, C. Panse, B. Mandl, K. Dick, M. Keplinger, J. Persson , P. Caroff, D. Ercolani, L. Sorba, F. Bechstedt, J. Stangl, G. Bauer, *Nano Lett., 11* , 1483, (2011)

[8] W.L., Bragg, Proceedings of the Cambridge Philosophical Society 17, (1913)

[9] J. Als-Nielsen, “Elements of Modern X-ray Physics”, Wiley,1st edition, 2001

[10] B. Warren, “X-ray diffraction”, Dover Publications, 1990

[11] U. Pietsch, V. Holy, T. Baumbach, ” High-Resolution X-Ray Scattering: From Thin Films to Lateral Nanostructures”, Springer; 2nd edition, 2004

Chapter 4

MOVPE Au-assisted growth of InAs NWs on GaAs[111]B substrate

The results of investigations of InAs nanowires grown by a vapour-liquid-solid mechanism with Au-catalyser by X-ray diffraction methods realized in out-of-plane and in-plane geometry of diffraction using synchrotron radiation are presented. InAs NWs on GaAs $[\bar{1}\bar{1}\bar{1}]$B substrate are received in the results of heteroepitaxial growth in MOVPE chamber. The characterization of the growth process based on the inspection of the samples with different growth time performed by scanning electron microscopy and X-ray diffraction techniques. The growth occurs via graduated alloy layer nucleated at early stage of growth. The vertical growth is taking place after supersaturation of catalyst particles by source material.

Chapter is based on paper: J. Brauer, U. Pietsch, A. Davydok, A. Biermanns, J. Grenzer, V. Gottschalch, G. Wagner, "X-ray investigation of the interface structure of free standing InAs nanowires grown on GaAs $[\bar{1}\,\bar{1}\,\bar{1}]$B", Appl. Phys. A, 96, 851, 2009

4.1 Introduction

Semiconductor nanowires (NWs) raise an interest due to the ability to produce single-crystalline 1D epitaxial structures and heterostructures in the nanometer range. The superior electrical and optoelectronic properties of semiconductor nanowires make it highly attractive for future manufacturing of nanoscale devices. Nowadays nanowires have already found application as single-electron transistors (SET) [1], resonant tunnelling diodes, light emitting diodes (LED) [2], photo detectors, lasers and nano-sensors for detection [3] of biological and chemical specimen [4]. In this chapter we present results of structural investigation of the NWs growth process using X-ray diffraction techniques and SEM imaging.

VLS growth of semiconductor NW is mostly realized on [111] oriented substrates for nearly any materials of group $A^{III}B^{V}$ [5]. Important place in growth theory is dedicated to defects structure of the grown objects. Novel properties of well-studied materials are crucially dependents from the local atomic distribution and ordering. One of the advantages of MOVPE growth is opportunity to control of defect structure of grown heterostructures [6, 7]. Semiconductor NWs nucleate in the result of supersaturation of metal catalyses (in most common cases – gold) by one of source material components. Vertical growth occurs after alloy formation with the presence of liquid metal droplets and vapour semiconductor elements (see Chapter 2). The size and position of catalysts defines the size and position of future NW. The VLS growth process itself is not fully studied and for the moment is under debates. Results of different groups are contributing to general model applying various experimental techniques. For example, Dick *et al.* proposed that growth is initiated by a solid seed particles (vapor-solid mechanism) during InAs NW growth [8]. However, Dayeh *et al.* [9] are not in agreement with the conclusions of [8]. Such question can be solved by detail analysis of surface/interface characterization on different growth stages.

Real space structure information of certain NW can be obtained by TEM, but a statistical analysis of many wires is an utopian task because of expensive preparation procedure. In other hand, SEM can provide images of NWs arrays but without information about the internal structure. In contrast to TEM, X-ray diffraction is unrestrictive technique and can provide structure information from NWs ensembles without special preparation procedures. This method is sensitive to size, material composition and internal strain. In particular, grazing incident diffraction is a tool dedicated to surface/interface investigations due to possible control of X-ray penetration depth [10].

Prior reported investigation the first steps of the structural analysis of the grown system have been done. Single wire inspection performed by TEM and X-ray diffraction experiments demonstrated the presence of two structural types in NWs – zinc-blende and wurtzite [11]. Also the existence of a close transition layer between substrate and NWs has been shown. The formation of the transition layer and the appearance of alloy of metal seeds with source material are important questions for further design of future devices.

In this chapter I report on results received by use of different geometries of X-ray diffraction applied for structural characterization of the InAs NW growth process by the VLS mechanism via gold seeds on GaAs $[\bar{1}\bar{1}\bar{1}]$B substrate. The investigation of growth procedure was performed on sample series with different growth time corresponding to certain stages of growth procedure, starting from very first seconds and up to NWs with length of micron. The results became a basis for the creation of model of the growth process.

4.2 Experimental technique

A detailed overview on preparation and growth is published in [12, 13]. NWs were grown on GaAs $[\bar{1}\bar{1}\bar{1}]$B substrate. The growth process was catalysed by gold particle formed from 1nm gold layer deposited on the substrate. The NWs were grown in LP-MOVPE chamber, a commercial system (AIX200) with pressure of 5 kPa and 7000 sccm total gas flow and hydrogen atmosphere. Trimethylindium (TMI, p = 0.36 Pa) and arsane (AsH_3) served as precursor materials. The investigated samples were grown at 450°C with V/III ratios of 10 without additional pre-annealing. The growth time was varied between 20s and 300s. For further structural analysis X-ray out-of-plane diffraction and GID were performed.

Prior to X-ray experiments the NW samples were examined by SEM (Fig. 4.1). The SEM study was realized at a FEI Nova 200 NanoLab system with a field-emission cathode. X-ray measurements have been performed at ID01 beamline of ESRF (Grenoble, France) and at X-ray lab of University of Siegen. First step of investigation was out-of-plane X-ray diffraction measurements, performed at the high-resolution diffractometer GE HR-XRD 3003 at Siegen University using a coplanar Bragg reflection and Cu Kα1 radiation. Line profiles of θ–2θ have been recorded close to the InAs (111) and GaAs(111) Bragg reflections by a Cyber-star point detector. After recording of diffraction patterns,

the angular values were recalculated into energy-independent coordinates of reciprocal space using equations shown in subchapter 3.10.

The GID experiments for different growth time were accomplished with λ = 1.41 Å at the ID01 beamline of ESRF (Grenoble, France). Phase sensitive scan and evolution of the transition layer were characterized by studying of in-plane lattice compounds of the samples. During GID measurements the incident angle of X-ray beam is keeping constant with respect to the surface and fixed in range of critical angle (angle of total internal reflection) of substrate (with discussed energy for GaAs 0.3°). In order to determine the composition of buffer layer and NWs corresponding WZ and ZB sensitive reflections were chosen. We fixed the detector at the calculated 2θ position for a certain Bragg reflection and rotated the sample around out-of-plane (111) direction. By tuning the incident angle of the beam to the sample α_i, one is able to control the penetration depth of the beam. For incident angle smaller then critical angle, refracted wave cannot propagate into the material. Instead there will be an evanescent wave travelling parallel to the surface, with an exponentially decaying amplitude away toward the interior of the material. This is important, if the diffuse background from defect scattering in the bulk is an issue, in particular for scattering from a nanostructures on the surface. Described geometry allows to distinguish signal of substrate and structures on the surface. Even above the critical angle the penetration of the wave is reduced enough, in order to reduce bulk scattering. For scattering for single crystalline substrates often an incident angle of tens of degree is chosen. The intensity of substrate reflection is increasing with increase of incident angle. Passing through interface, the wetting layer contributes to the scattering signal in addition to that of the substrate. Due to specific of experimental geometry, the GID measurements are presented in surface coordinates described in Chapter 3.8.

4.3 Results and discussion

First step of the research has been realised at home X-ray lab of University of Siegen. A submillimetre sized X-ray beam has been used for illumination of macroscopic samples. The diffraction signal produced by all types of structures existing in the investigated systems visible on SEM images (Figure 4.1). SEM images of the samples series with variation of growth time from 20sec to 300sec demonstrate temporal evolution of the growth.

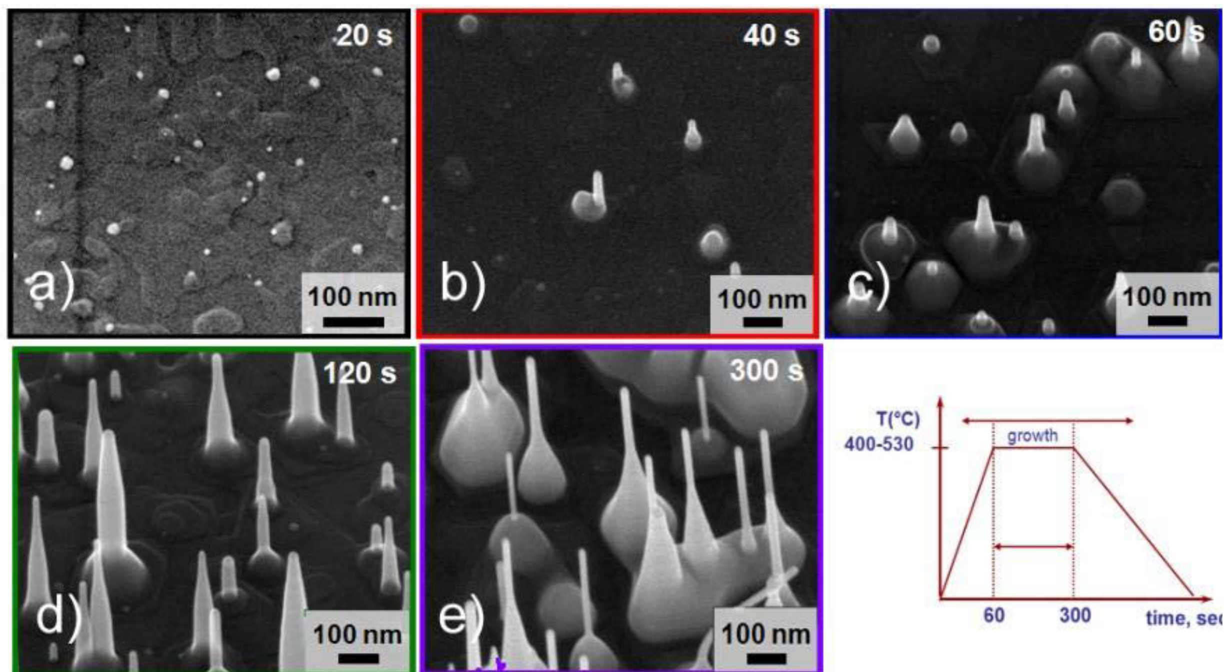

Figure 4.1 SEM images of growth samples series: a) growth time 20 sec; b) growth time 40 sec; c) growth time 60sec; d)growth time 120 sec; e) growth time 300 sec

Time spans chosen for sample preparation are corresponding to different stages of growth. After 20 sec first droplets appeared on sample surface and start to move horizontally leaving traces of crystallized material (Fig. 4.1a). First vertical structures like NWs start to appear after 40 sec. With further increase of growth time number and sizes of vertical structures are increasing. Additionally one can observe the increase of size at the bottom part of NWs which characterizing the droplet shape. After 120 sec no gold partials can be detected which are left the substrate surface. The temporal development of NWs structure was investigated by X-ray diffraction – out-of-plane and in-plane geometry. Fig. 4.2 represents line X-ray profiles recorded for 5 samples of growth series close to

InAs and GaAs (111) Bragg reflections. Our experimental results are in agreement with SEM investigation. Only after 60 sec one may observe measurable intensity in the q_z range of InAs reflection (q_z=17.9nm^{-1}).

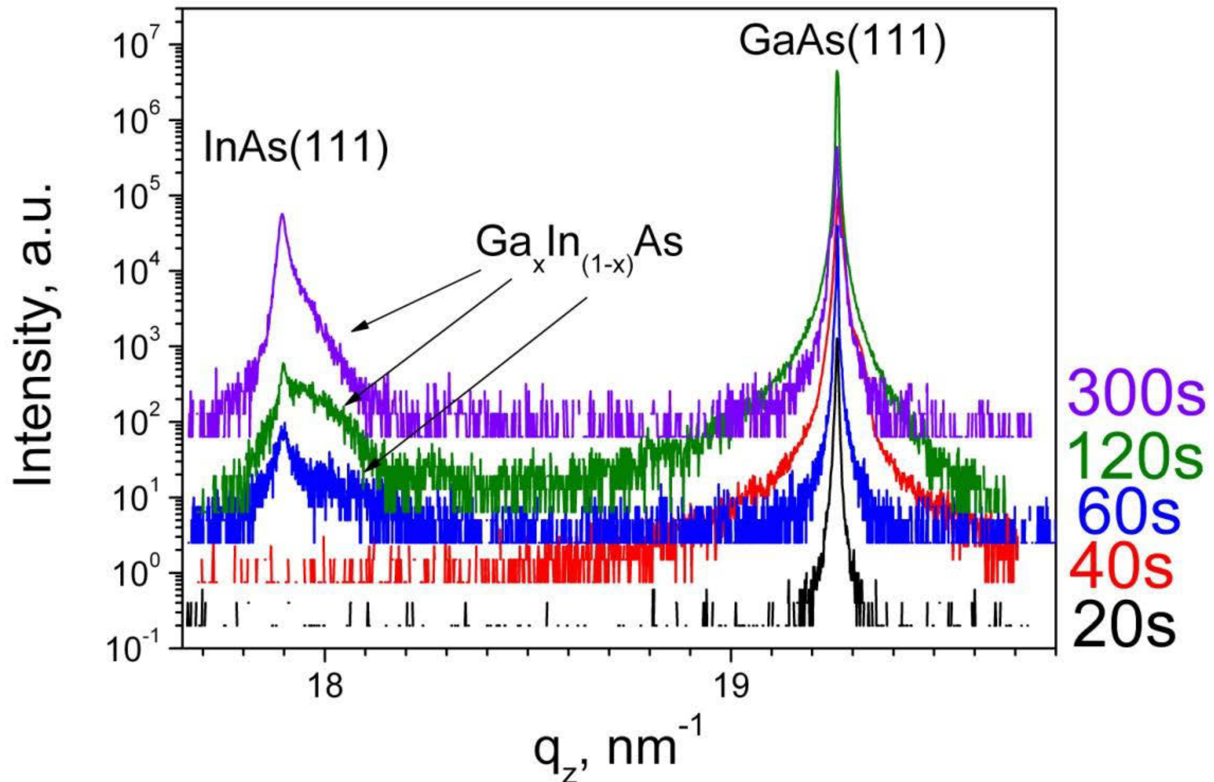

Figure 4.2 Results of out-of-plane X-ray diffraction measured for growth time series. After 60 sec of growth signal from $Ga_xIn_{(1-x)}As$ wetting layer appeared

After 20sec and 40 sec the amount of InAs deposited on substrate is too small to produce a diffraction signal under home lab conditions that is why only GaAs (111) reflection appeared in the corresponding scans. After 60sec of growth time a small asymmetric signal of the InAs peak was detected. The asymmetric shoulder can be explained by the presence of $Ga_xIn_{(1-x)}As$ alloy. Between 60sec and 120sec the intensity of InAs reflection is increasing together with intensity of the shoulder. After 300 sec a strong signal of InAs is observed in the same time the intensity of $Ga_xIn_{(1-x)}As$ alloy kept constant. This result can be interpreted as NWs growth starting from the wetting layer which covers the sample surface; after 120 sec the whole surface is covered by $Ga_xIn_{(1-x)}As$ alloy but nucleation of new InAs NWs is going on during the whole growth process.

Measurements of the phase composition were performed in GID geometries (fig. 4.3). Series of in-plane reflections with the same out-of-plane momentum

transfer was chosen for the experiment. For each sample experiments were performed with incident angle α_i lower then critical angle of the substrate α_C (top curves) and higher than critical angle (bottom curves). In GID geometry ($4\overline{2}\overline{2}$) is reflection of zincblende phase corresponding to ($30\overline{3}0$) reflection of wurtzite phase. Along the same direction ($20\overline{2}0$) reflection can be found which has no representation in the zinc-blende phase (see Chapter 3). Comprising the two reflections one can obtain information of structure evaluation during growth process.

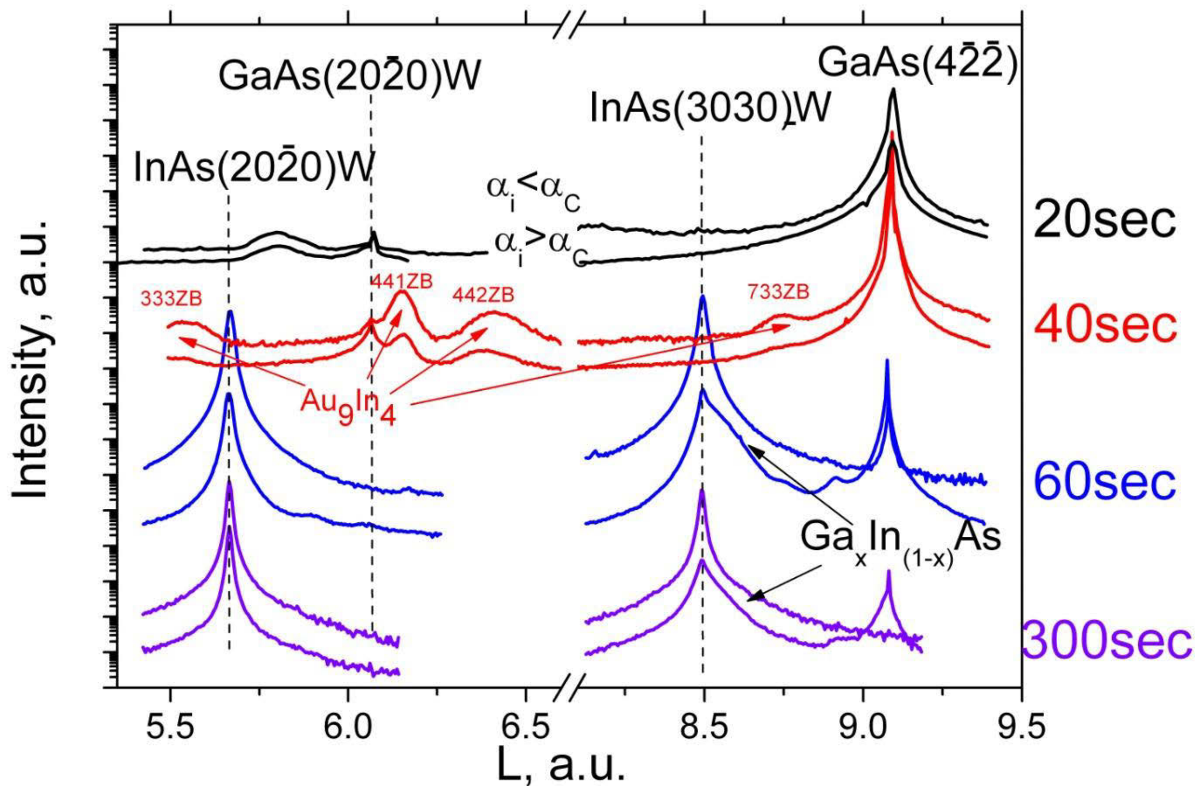

Figure 4.3 Results of GID measurements through line of($20\overline{2}0$) / ($30\overline{3}0$): for each sample represented curve measured with $\alpha i<\alpha c$ (top) and $\alpha i>\alpha c$ (bottom)

SEM images and out-of-plane diffraction did not show NWs signal from samples with growth time less than 60s. However quasi-peak is found at GaAs wurtzite position. Possible explanation is the existence of stacking faults and nucleation of small amount of GaAs WZ material after reaction with gold catalysts which give a weak signal. For 20sec sample a hump appears in range of L=5.65 refer to phase of gold alloy. It is not observed any more for longer growth. Also curves measured from 20 sec looks quite similar for both cases of incident angle – $\alpha_i<\alpha_c$ (top curves) and $\alpha_i>\alpha_c$ (bottom curves). After 40sec a set of new reflections appeared. We identified them as Au_9In_4 phase of surface alloy (see

Chapter 2, Fig. 2.2). Structures belong to the surface because the intensity of discussed peaks is higher in case of penetration the substrate by the beam ($\alpha_i<\alpha_c$). In figure 4.3 we marked reflections of different orientation of Au_9In_4. According to growth details explained in [12] wurtzite GaAs layer is a result of preparation procedure of InAs NWs growth. Growth was performed at temperature 450°C but already at 420°C the interface between gold particles and substrate material become liquid and creates the alloy. Under influence of external As-flux the alloy decomposes into solid Au-droplets (with content of Ga) and GaAs. Deposition of such GaAs is characterized by the creation of many of twin defects what in result gave a signal at GaAs wurtzite L position. After 60sec of growth signals from InAs NWs appeared for first time. The NWs have a wurtzite structure because peaks of increasing intensity are found at $(20\bar{2}0)$ and $(30\bar{3}0)$ wurtzite position. In the same time the shoulder corresponds to wetting layer because it at $(30\bar{3}0)$ only and only for case of higher incident angle. The findings of $Ga_xIn_{(1-x)}As$ layer in zinc-blende structure agrees with [10]. Growth of InAs NWs can be described in two steps: growth of $Ga_xIn_{(1-x)}As$ layer followed by gold-rich layer formation in condition of external In- and As-fluxes. After horizontal alloy growth (growth time below 60sec) the vertical growth of InAs NWs is starting from a Au_9In_4 solid solution. During the growth, deposited gases of indium and arsenic are collaborating with liquid Au-Ga solution, created from liquid gold and diffuse from substrate gallium. It leads to not promotional increasing of the radial size of bottom part of NWs (fig. 4.1).

4.4 Growth Model

Based on experimental results after inspection with SEM and XRD, a growth model was proposed. Solid gold particles are reacting with GaAs substrate under conditions of external pressure created by As-flow. With beginning of In-flow, the VLS process is starting. First indium collaborates with Au-Ga alloy creating $Ga_xIn_{(1-x)}As$ solid solution. The crystal growth is going on in form of traces on substrate surface (fig .4.1a). A model of such a trace is shown in fig. 4.4.

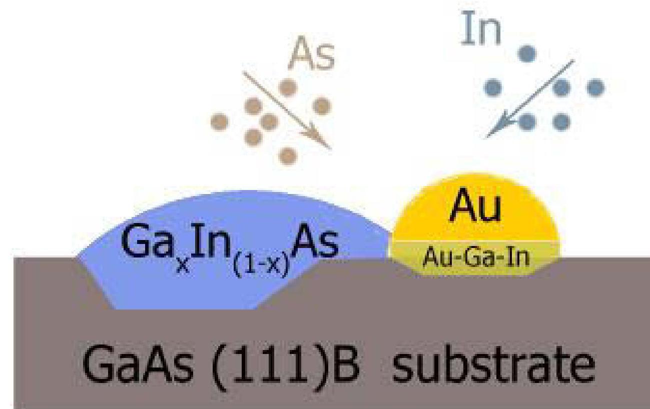

Figure 4.4 Scheme of NW nucleation process during VLS growth

From described experiments the following conclusions can be done: a presence of wurtzite GaAs has been found after alloy formation of Au and substrate material under certain temperature and pressure conditions. Also such conclusion is confirmed by preparation technique of the substrate. Deposition of 1nm gold layer on GaAs wafer predicts the creation of a Au-Ga alloy with high Ga content. Based on the results SEM inspection and X-ray structure analysis, we proved the appearance of a ZB $Ga_xIn_{(1-x)}As$ wetting layer. The growth is characterized by switching from the planar growth of the layer to vertical one of wurtzite InAs NWs. The change of growth direction is justified by changes in interface energies [13].

4.5 Summery

In this chapter the heteroepitaxial growth of wurtzite InAs NWs was examined by SEM and a XRD techniques. Based on experimental results substrate/NW interface was described and model of NWs growth process was proposed. Switching from horizontal to vertical VLS growth was detected. By GID measurements phase composition of structure components on different stages of growth could be determined. Au-Ga alloy has been found for the first stages of growth. Further formation of solid $Ga_xIn_{(1-x)}As$ solution plays an important role in nucleation of InAs NWs. Phase of $Ga_xIn_{(1-x)}As$ alloy was found to be zinc-blende. In contrast, InAs NWs preferentially grow in wurtzite phase. Growth of pure InAs (without Ga content) is observed after 120sec. From XRD measurements lattice parameters of InAs NWs were calculated a = 4.243 Å and c =7.025 Å (c/a = 1.656).

Chapter 5

The influence of growth parameters on the phase composition and defect structure of InAs nanowires grown by self-assisted molecular beam epitaxy onto Si(111)

In this chapter, I discuss the results of structure investigations of InAs NWs grown by MBE on Si substrate. The preferentially nanowire structure is wurtzite but our findings demonstrate that the grown nanoobjects are highly defective. Evidence for the high density of SF has been found by probing Bragg reflections being particular sensitive to SF inclusions. Numerical estimations of SFs density were done by calculation of X-ray diffraction pattern based on the model of a statistical average over many nanowires. Also, growth of parasitic zinc-blende islands has been observed. To improve the quality of growing structures and to find key parameters of growth, I demonstrate the results of the investigation of a sample series grown under different growth conditions and probed the SF density and the ZB phase contribution.

In 2010 K. Dick *et al.* reported about the possibility to control the nanowire crystal structure by variation of growth temperature and pressure, the molar pressure fraction and the V/III ratio. These growth experiments have been performed for six materials of III-V group. For Au catalyzed growth of InAs NWs it was demonstrated that it is possible to control the structural phases by changing the growth temperature within the range from 400 to 480 °C. The increase of growth temperature has an effect on the morphology of the NWs. The NW diameter is observed to be larger for ZB NWs then for WZ NWs. In addition, a narrow temperature window slightly lower than 400°C was found where the stacking fault density dramatically has decreased and a change of structural phases took place [15]. The authors explained this fast change of structure by thermodynamic effects but not by the growth kinetics. As we discussed earlier, the use of metal catalysts leads to undesirable effects during the growth. For example, at typical growth temperature (400-500°C) gold particles diffuse into the substrate creating deep level defects and destroying the surface layers [16].

An alternative way to eliminate the use of metal catalyst is the self-assisted growth of NWs (see Chapter 2), which successfully has been obtained and reported in 2007 [17]. The structure was analyzed by TEM demonstrating a high density of SFs and twin defects in the grown nano-objects. The growth of highly defected structures can be explained by phase mixture of the two possible structure types – wurtzite and zinc-blende (Chapter 3). The growth usually realizes along substrate cubic direction [111] independent from substrate orientation [18]. Despite the difference in stacking sequences, [111] axis of ZB phase is [0001] direction of hexagonal phase, which makes *in-situ* phase control complicated. Nevertheless for Au-assisted growth strong dependence of crystal structure from growth parameters and growth preparation methods has been shown. Phase-controlled growth was achieved and demonstrated for InAs NWs grown on InAs [111] substrate. NWs grow usually in wurtzite phase, when the substrate is bulk InAs. Out-of-plane lattice parameters of wurtzite and zincblende phases differ by 0.4% only [19]. In case of InAs and Si the lattice mismatch is 11.6%. Despite the lattice mismatch, MBE growth provides an opportunity to grow strain relaxed InAs NWs on Si substrate [20].

S. Hertenberger *et al.* [21] demonstrated self-induced growth of InAs NWs on Si (111) by solid-source molecular beam epitaxy. The growth is characterized by spontaneous nucleation followed by VLS growth. The growth was performed with different V/III-ratios. The structure was investigated by *in-situ* RHEED, SEM and TEM techniques. TEM images were obtained for NWs grown under As-rich and under In-rich growth conditions. The images exhibit highly defective structures with an approximate periodicity of SF of 1 nm for both types of

growth. Tomioka *et al.* used Raman spectroscopy and TEM for the structure characterization of self-induced InAs NWs grown on Si substrate by selective-area metal-organic vapor epitaxy. The growth was performed on InAs and Si substrates. High density of twin defects was observed with periodicity of 1-3 bilayer distances for both substrates. The grown structures exhibited a mixture of zincblende and wurtzite phases [22]. A tendency of high SF density of InAs NWs grown on Si was also reported in [23]. InAs nanowires were grown on Si substrate in a MOCVD chamber. The morphology of InAs nanowires were inspected by SEM. The images show vertically standing nanowires with a small amount of parasitic islands. TEM investigations demonstrated that the nanowires are highly uniform in diameter. No metal droplet was observed on top of the nanowires. High-density of twin defects and stacking faults were found along the whole wire length.

Explanation of NWs polytypism has been developed in recent years. The classical nucleation theory is used to describe the growth temperature dependence of twin planes density. Glas *et al.* suggested a theoretical description of the dependence of both structural types from the position of solid/liquid interface. Growth initiates after the supersaturation of droplet by the source material atoms [24].

Another undesirable effect is the parasitic growth of islands. The presence of parasitic islands was observed usually in SEM images together with InAs nanowire. Authors of [25] described those phenomena for catalysts-free growth of InAs by the influence of the oxide layer. The growth is initiated by desorption of indium atoms from the Si/III surface. The thick SiOx-mask prohibits wetting of the substrate by the highly mismatched NWs material. The nucleation process fully depends on indium adsorption and desorption kinetics. Free island growth appears due to a large energy barrier between surface and volume free energies [26]. It leads to a reduction of the stacking variety in the very beginning of the growth process. When the island size is smaller than the critical size, the growth continues with a reduction in total free energy. The number of adatom incorporation into the island increases constantly. Such growth continues while desorption is decreasing with time up to the indium desorption saturates. Such explanation was proposed for low temperature growth process (450-520°C). For higher temperatures (560°C), the growth is limited by the number of nucleation events and the larger re-evaporation of diffused indium adatoms compare to lower temperature.

The understanding of parasitic growth helps to improve the growth procedure. Tuning the growth conditions can improve a structural perfection of the grown wires and reduce a parasitic contribution. Most of the reports dedicated to structural investigations are based on the results of TEM

inspections providing real space images of the NW structure. Information on the defect structure of selected NWs can be obtained by HRTEM. Only a small number of objects can be examed by this technique due to the complicated preparation. It makes it difficult to obtain statistic information about structural properties.

In case of XRD experiment, from intensity and FWHM of Bragg peak one can judge the amount of material and the defect density. A small amount of material produces broad reflections, but with low intensity. In our experiments we observe a broad peaks with high intensity at reflections particular sensitive to stacking faults. That can be explained by the high density of SFs.

For interpretation of X-ray data I used a numerical description of the defect structure of the NWs. In particular I performed a simulation of unique WZ reflection being sensitive to inclusions of SF such as (10i5) reflection for WZ phase. Numerical simulations are based on a Monte Carlo approach [27] assuming statistical distribution of certain numbers of different types of SFs and the distances between two neighboured fault planes. For application at NWs the undisturbed basis function is the shape function of a NW described by a SINC function.

For a quantitative analysis I used the approach published recently [28] developed for considering the influence of SFs on the diffraction patterns taken from thin films. It neglects effects of dynamical X-ray scattering and describes the kinematical diffuse. The simulation considers the following simplifications: the main structure of NW is wurtzite; the incident and exit angles of the X-ray are much larger than the critical angle of total external reflection; the position of SFs is random and the density of fault planes is high enough to assume a statistical ensemble average for the X-ray signal. X-ray scattering intensity originated by a set of randomly stacked SFs. The numerical simulations are based on a Monte Carlo approach assuming a statistical distribution of SFs and the distances between two neighboured fault planes. It has been shown that different types of stacking faults (e.g. changes from ABAB to BCBC or ACAC type of stacking) lead to slight differences in the broadening of the affected Bragg reflections [29], which can be accessed for particularly high ordered materials. However, in the present case no distinction between the different types is possible due to the very large broadening of the reflections, and I considered a random sequence of intrinsic SFs only.

For all samples, simulations were performed for the wurtzite reflection only with average height as obtained by the SEM images. The broadening of the reflections was then simulated by the inclusion of stacking faults with mean distance MF (indicated in Figures), assuming a geometrical distribution of the distance between subsequent fault planes. For growth series sample described in

Chapter 6, in each simulation step, the results from the preceding step for shorter NWs have been considered, as these segments are maintained at the bottom of the NWs.

Parasitic islands exhibit ZB phase (see chapter 6). We suppose that the main contribution to ZB reflections intensity measured in experiments comes from islands. We use this approach for the characterization of NWs systems grown under different growth conditions. In such way, we investigate the effect of growth parameters on the NWs parasitic islands density. Choosing WZ and ZB reflection with the same in-plane momentum transfer, one get an opportunity to perform phase sensitive measurements by a single scan experiment. The SF density and number of islands crucially depend on growth parameters as the growth temperature, the V/III ratio *etc.* and/or the method of substrate preparation. Although the number of investigated samples is small, but they can be use to demonstrate structural differences provided by the tuning of the growth parameters.

Presented data were measured at two synchrotron radiation source facilities. One set of samples were measured at DELTA Synchrotron in Dortmund (Germany) at BL9 beamline dedicated to high resolution diffraction experiments. The measurements were done at 11 keV energy with submillimeter beam size. Diffracted intensity has been recorded with a two-dimensional PILATUS detector. The second set of data was obtained at the P08 beamline of PETRA III Synchrotron in DESY (Hamburg, Germany) with energy of 9keV and submillimeter beam size (500x200 μm^2 – horizontal and vertical size respectively). To record the scattered intensity, an one-dimensional MYTHEN detector was used. For sake of comparison of the experiments all angular coordinates were transformed into wavelength independent reciprocal space coordinates using the relations described in subchapter 3.10.

For data analysis and fitting procedure, the line profiles were extracted from RSMs integrating a q_x range of 0.4 nm^{-1} along q_z (the integration range is shown in Fig. 5.3a by black rectangle). Estimation of NWs/islands volumes ratio was done by normalizing the intensity and calculating the intensity ratio of WZ/ZB reflections. The integration of the intensity of WZ reflection has been done between q_z=42.7nm^{-1} and q_z=46.5nm^{-1}. The island contribution was estimated from the sum of integrated intensity of the two ZB reflections.

5.1 As-/In-rich conditions

At first we tested our approach on NWs grown on bare Si substrate under indium-rich and arsenic-rich conditions. The growth was realized under so call

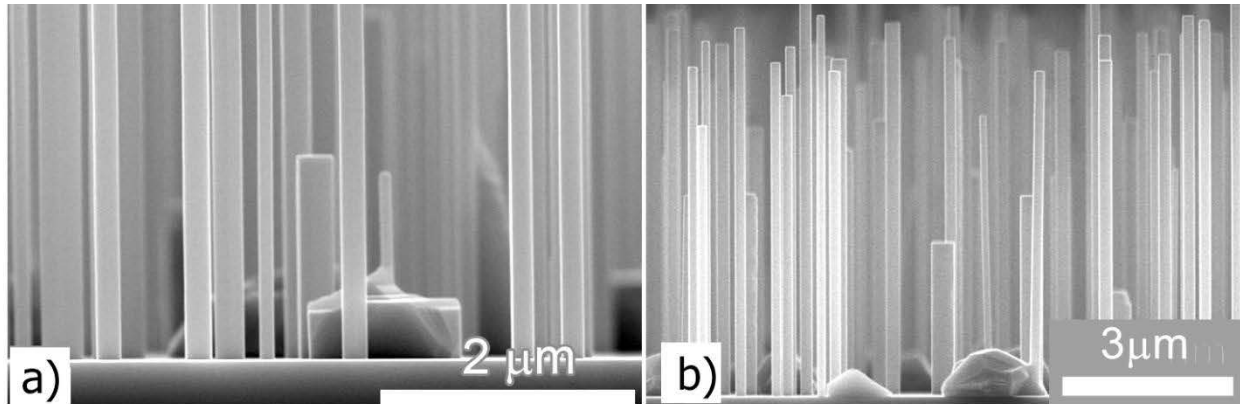

Figure 5.1 SEM images of InAs NWs grown under: a) As-rich conditions; b) In-rich conditions

“typical” growth conditions such as: growth temperature 450°C and V/III ratio 120. The total content of InAs used during growth for both samples was the same. At arsenic-rich conditions, indium was supplied for two hours with low In-flux. Indium-rich conditions have been achieved by 30min deposition of indium with low flux followed by 45 min with double flux.

The growth of InAs NWs under As-rich and In-rich conditions has been discussed in [25]. The grown NWs were characterized by SEM concentrating on the morphology of NWs. The authors explained the islands formation by the low indium adatoms diffusion from the substrate and local increase of indium concentration up to supersaturated of nucleated particle. One way to solve this problem is an increase of In-flux under constant V/III ratio what has been done for our experiment. In [25] was shown the influence of In-flux on morphology of the NWs. With the increase of In-flux, the axial growth rate and the diameter demonstrate similar behavior – linear increase up to a certain value and fast drop down, corresponding to InAs clusters formation on the sample surface (not islands anymore, but close layer).

The characterization of the NWs started with SEM analysis (Fig. 5.1). No difference in morphology was observed within the inspected areas of both

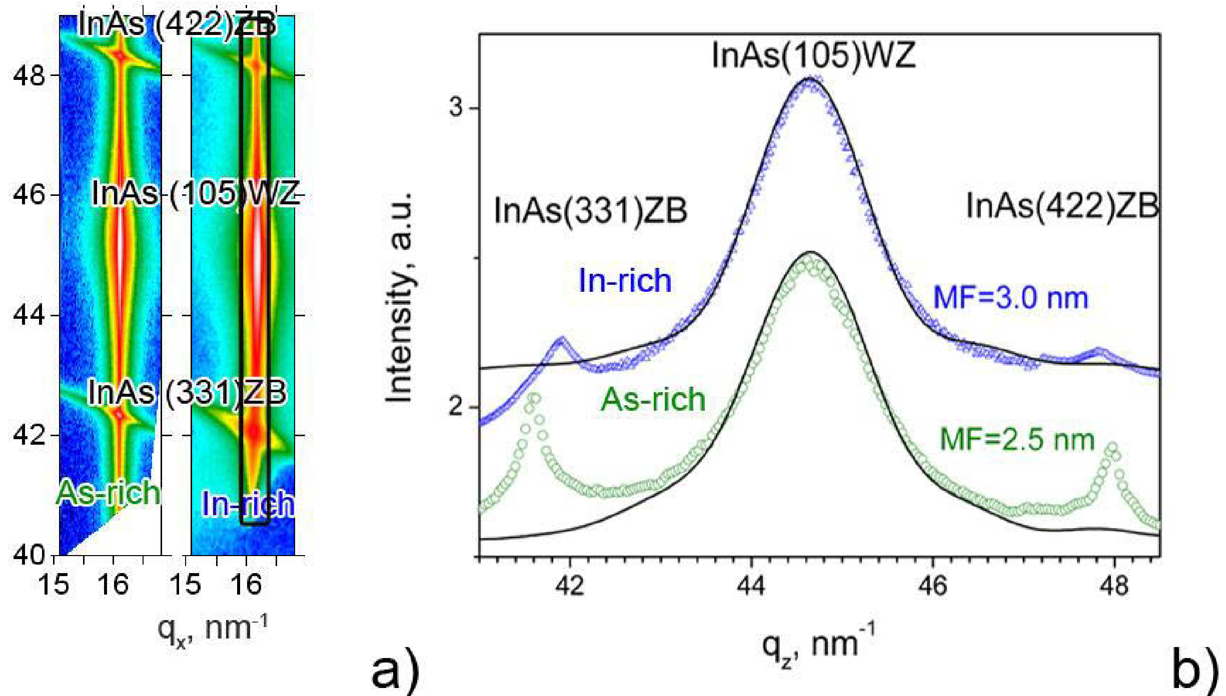

Figure 5.2 a) Reciprocal space maps measured through (331), (105) and (422) reflections; b) line profiles extracted from RSMs (dotted lines) and simulation of WZ reflection (solid line) , MF - average length of perfect WZ segment

samples. The shapes of grown structure look similar and uniform. NWs grow show hexagonal shape. Grown structures are vertically aligned with average length of 4μm and an average diameter of 200nm.

Figure 5.2a demonstrates RSMs recorded for both samples. The CTR can be observed on both maps at q_x=16.05nm^{-1}. At q_z=41.89 nm^{-1} and q_z=47.86 nm^{-1} ZB reflections are visible – (331) and (422) respectively. Small inclinations of reflections with respect to q_z were related to variation in orientation of diffracted object. The symmetry of zinc-blende peaks requires repeating same the reflections with periodicity of 120°. The family of reflections {331} and {422} rotates with respect to each other by 60°, so usually the appearance of both reflections along the same q_z line is a signature of the appearance of twin defects. But we also have shown by the experiment with nano-size beam, there are two kinds of islands existing on the sample surface oriented (331) and with orientation (422) (Chapter 6) what can separately contribute to diffraction pattern of the ensemble.

Estimating NW/island volume ratio for the case of As-rich growth, we received 1.6 and for case of In-rich this number is 2.9. Our results are in agreement with assumption that an increase of In-flux decreases number of islands. In case of In-rich growth, zincblende reflections exhibit less intense

peaks compared to As-rich (Fig. 5.2b). In addition, Monte Carlo simulations have been performed to describe the defect density of the discussed samples. Using identical input parameters (number of illuminated objects, number of planes within a coherent patch, plane distance in the wurtzite lattice *etc.*) for both samples, simulations were performed by fitting the average distance between two neighboring stacking faults. Results of simulations are shown on Fig. 5.2b, where the distance between two neighbors SF is marked by “MF”. The error bar of my calculations is about 1 nm, so the difference in average WZ segment length of 0.5nm is within the error bar and negligible. The average length of perfect WZ segment is 2.5 nm and corresponds to SF density 0.41nm^{-1}. It characterizes the grown NWs as highly defective. We conclude that the increase of In-flux has not improved the perfection of NWs, but reduces the amount of ZB compounds in the system.

5.2 Substrate coverage

The same technique of NWs/islands volume ratio and estimation of SF density was used to characterize the effect of the substrate coverage. In the previous subchapter, we discussed the nanowire growth on bare Si substrate concentrating on the effect of indium flux. The presented theory of island formation [25] crucially depends on the thickness of the native oxide layer onto the substrate. Here, we compare structures grown on bare substrate and those covered an oxide layer. In literature one can find a number of reports on different kinds of substrate coverage by native SiOx layer, Hydrogen Silsesquioxane (HSQ), nonconductive polymer layers or buffer layers used for the reducing of lattice mismatch between substrate and grown material [28-30]. In these reports

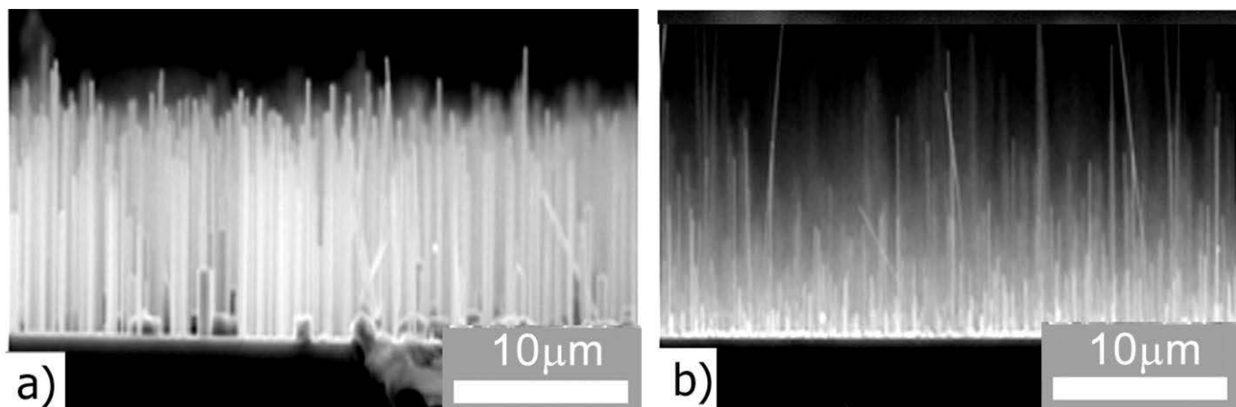

Figure 5.3 SEM images of InAs NWs grown on: a) bare Si substrate; b) on native SiOx layer

tendency in morphology of NWs were observed and discussed. Authors of [30] mentioned that the use of a thin oxide layer (1-3 nm thickness) increases the

density of NWs. The grown wires are characterized by a high aspect ratio and a small number of parasitic islands. At the same time, the use of a thick oxide layer leads to the growth of tilted i.e., not perfectly vertical aligned wires. NWs grown on bare substrate are characterized by a lower number density and a lower aspect ratio. All conclusions were done based on results of SEM and TEM studies. In this subchapter, I compare InAs NWs grown on Si substrate covered by native silicon oxide layer and those grown on bare Si.

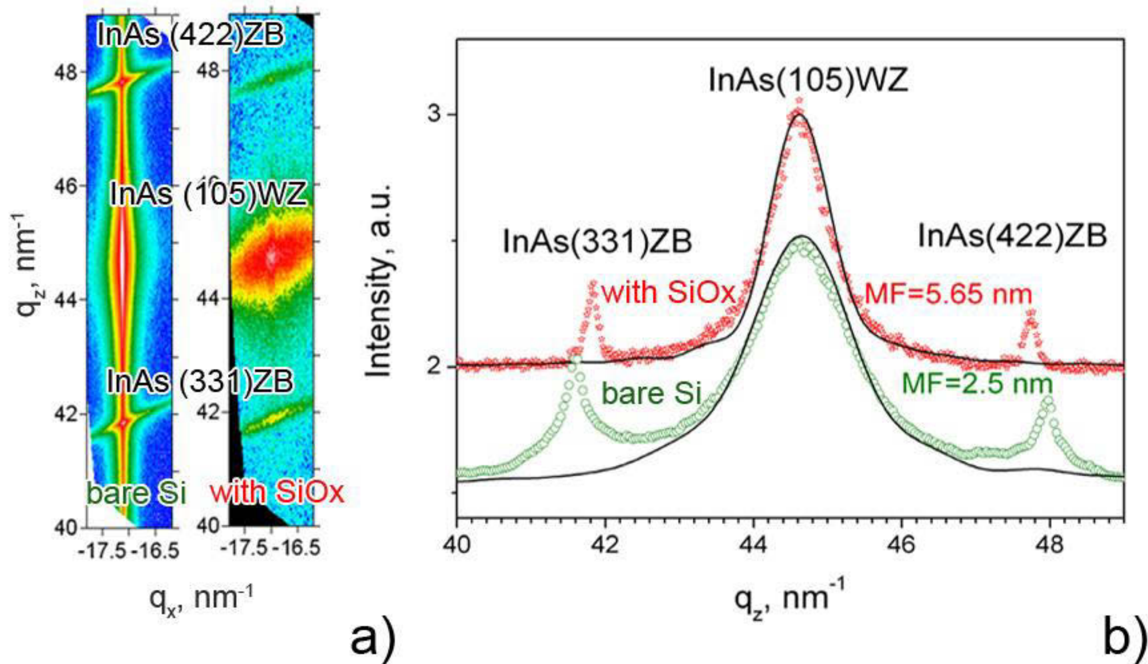

Figure 5.4 a) Reciprocal space maps measured through (331), (105) and (422) reflections from NWs grown on bare Si (left) and on native SiOx layer (right); b) line profiles extracted from RSMs (dotted lines) and simulation of WZ reflection (solid line)

Both samples were grown in the same MBE chamber at temperature of 450°C with a V/III ratio 120 using equal amount of InAs (growth details described in Chapter 6). Prior the growth both substrates were chemically cleaned. Native silicon oxide layers were etched. The etching time defines presence and absence of the native oxide layer. As result NWs were grown on bare Si substrate and substrate covered with 2 nm thick oxide layer. The growth time was different for the two substrates due to the difference in the nucleation process. The growth on bare Si took two hours, on substrate covered with oxide layer the growth has proceeded for four hours and 20 minutes using the low growth rate mode to limit the nucleation of InAs on oxide layer but not direct on substrate via small holes. Figure 5.3 shows SEM images from both samples in large scale due to length of NWs. Figure 5.3a exhibits NWs grown on uncovered substrate. The NWs look uniform and more dense than in case of SiOx layer growth what can be explained by the low growth rate. The length of the NWs does not vary so much as in Fig. 5.3b. The wires grown on SiOx are characterized

by a lower density of parasitic structures (from top view SEM image – not shown) and NWs aspect ratio does not change so significantly.

Measured RSMs are shown on Fig. 5.4a, where one can identify the reflections (331) and (422) of ZB and (105) reflection of WZ phases of InAs. From the sample grown without SiOx layer, an intense line (CTR) through all three reflections can be observed. In contrast, in the second map one can see more intense spots at the Bragg peak positions, but no intense line along the whole q_z range. These findings can be attributed to two factors. NWs on the second sample are well-ordered and show a lower SFs density compared to the first case. The results of the fitting procedure are shown on fig. 5.4b by a solid line. Following our assumption that the NWs are forming in WZ phase, again I concentrated on WZ (105) reflections and use the same approach as in pervious subchapter. The structure perfection can be estimated from FWHM, which obviously is smaller for the case of SiOx surface. Simulations gave an average size of perfect WZ domain between two neighbor SFs. As mentioned in previous subchapter, the size of perfect domain for NWs grown onto bare silicon is 2.5 nm. In case of SiOx layer, this number is more then in two times larger and equals to 5.65 nm. For the ratio between WZ and ZB reflections for NWs grown on bare Si we received 1.6, for the second sample this ratio equals to 2.4. This is explained by the dominance of WZ structure in the system and the lower number of parasitic islands found onto the oxide layer compared to the case of bare Si. This observation is in agreement with [30].

In the introduction part I already mentioned the reasons of parasitic structures formation. More detail explanation can be found in [25]. The presence of the oxide layer is necessary for the immobilization of indium droplets on the surface restricting the particle size making NW nucleation possible [31]. From our findings, one can conclude that the use of the thin SiOx layer leads to a reduced number of parasitic grown structures and a lower SFs density.

5.3 Substrate temperature

One of the most significant parameter of growth is the substrate temperature. Tuning the temperature and the V/III ratio one is able to control the phase composition of the growing system. This has been demonstrated in several publications for different growth modes. In resent a paper H. Joyce *et al.* have shown that the NWs structure perfection depends on the interplay between various parameters. The authors found out empirically that for InAs NWs grown by Au-assisted metal-organic chemical vapour deposition at low temperature (400°C) and high V/III ratio, it is energetically favourable to form the zinc-blende phase. At higher temperature and lower V/III ratio, one is able to achieve a

growth of SF-free wurtzite NWs. The critical factor, determining ZB and WZ perfection, is the change in vapour-nucleus surface energy, which is hardly connected to temperature and V/III ratio [31]. For MBE grown NWs on Si substrate it was shown that the variation of growth temperature between 400°C and 500°C leads to changes in the NWs morphology. Also, TEM experiments demonstrated that most of NWs exhibited pure zinc-blende phase with a few exceptions of NWs showing defective regions [32].

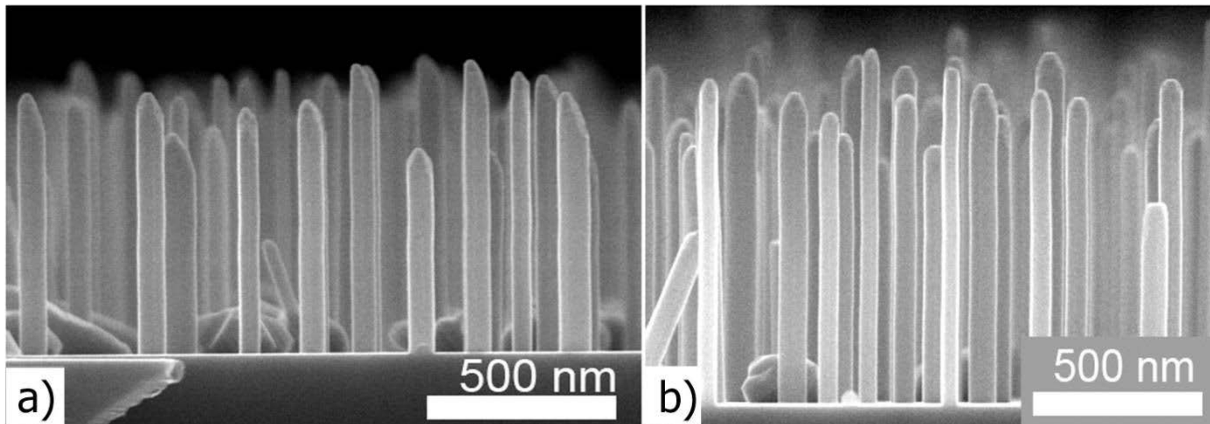

Figure 5.5 SEM images of InAs NWs grown with temperature a) 445°C, b) 425°C

For the next experiments we have chosen samples grown in different modes compared to the previous subchapters. The samples were grown on oxide layer at low V/III flux ratio. Here growers tested the influence of the substrate temperature on structure perfection of InAs NWs grown on Si (111) by MBE-mode. Before growth, the Si substrates were chemically cleaned in acetone in an ultrasonic bath for 3 min followed by ultrasonic cleaning in ethanol for 10 min and etching by 5% HF for 4.5 min, loaded to a piranha solution for 10 min and left in the air for two days. It gave the possibility to clean substrates from dust particles, to create (111) terraces and to grow a thin native oxide layer, which improve the growth process as shown in previous subchapter. The samples were grown in MBE chamber with short annealing before the growth procedure. The NWs were grown by 30 min with As/In-flux ratio of 30, with an equivalent planar growth rate 100 nm/h. In this subchapter, I discuss samples grown at 445°C and 425°C substrate temperatures. Figure 5.5 demonstrates SEM images of the inspected samples. Already from SEM investigations difference in NWs morphology can be detected. The sample, grown at 445°C, is characterized by vertically aligned NWs with height of 800-900 nm and NWs diameters of 70-130nm. For the second case, the length of grown NWs is larger compared to first case, but varies between 600 and 1100 nm. The diameter of wires is between 30 and 80nm. For both samples the NW density is nearly the same and amounts to 4 μm^{-2}. SEM images from both samples demonstrate the existence of parasitic

structures. The top part of wires does not look flat compared to the growth on bare Si with high V/III ratio.

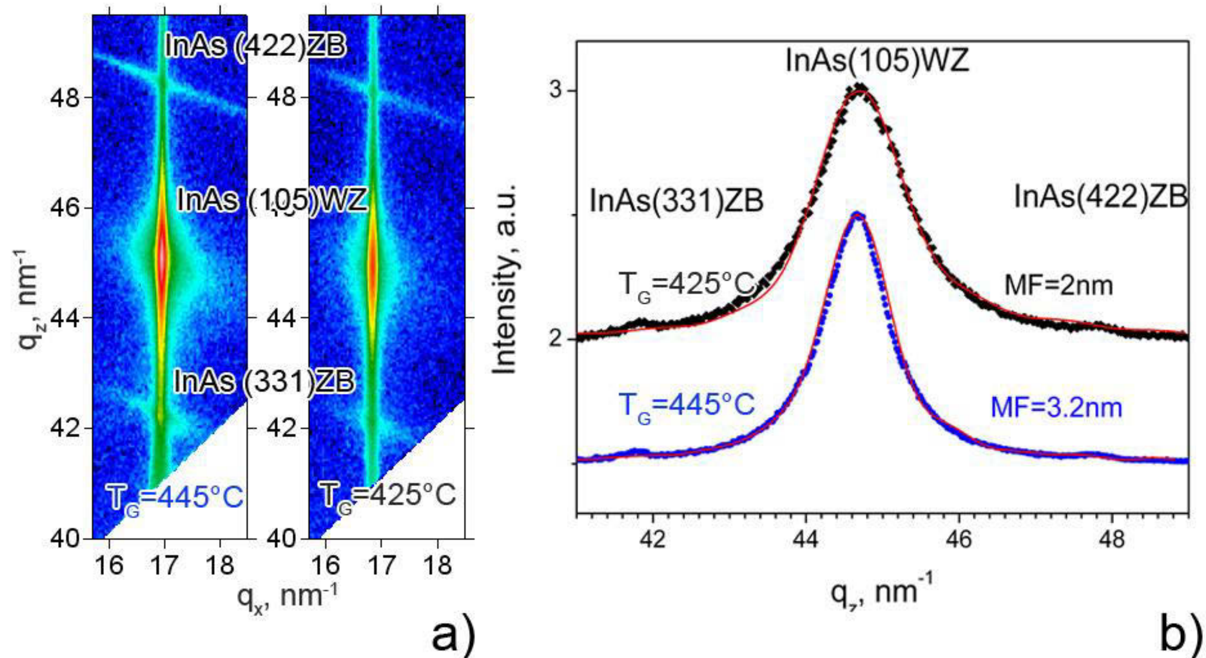

Figure 5.6 a) Reciprocal space maps measured through (331), (105) and (422) reflections from NWs grown with temperature 445°C (left side) and 425°C (right side map); b) line profiles extracted from RSMs (dotted lines) and simulation of WZ reflection (solid red line)

Figure 5.6a demonstrates RSMs maps recorded from samples grown with the different substrate temperature through ZB (331), (422) and WZ (105) reflections. Compared to the previous cases, shown in this chapter, ZB reflections are not so intense, but a strong signal from CTR is observed in contrast to the NWs sample grown on SiOx discussed before. ZB reflections are inclined and remained part of powder ring – corresponding to orientation of islands facets. At the same time, the intensity of the ZB reflections is close to the diffuse scattering of wurtzite reflection. Calculation of the ratio of the integrated intensity of WZ peak to the sum of intensity of ZB signals gave values 4.7 and 4.2. The difference of values is below by the error bars of calculations and did not demonstrate a difference of volume ratios between NWs and islands. Figure 5.6b shows line profiles extracted from RSMs. The shape of curves proved the low intensity of ZB reflections, which here can be recognized as small humps at q_z=41.9nm^{-1} and q_z=48nm^{-1}. Both curves are characterized by strong WZ reflections with a difference in FWHM is larger in case of growth at lower temperature. The average size of perfect WZ segment is demonstrated on fig 5.6b. The error bar of the fitting procedure is in the range of 1 nm (curves still can be fitted in this limits with corresponding tuning of other fit parameters admissible by physics of the process). The difference of MF parameters of about 1.2 nm provides approved by obviously different FWHM of both curves. Test of the intensity ratio did not

show remarkable differences for two temperatures applied for NWs growth process in terms of WZ/ZB ratio. For both temperatures a low amount of ZB compounds is observed, smaller compared to growth modes demonstrated in subchapters 5.1 and 5.2. The internal structure is characterized by a high number of SFs with lower defect density in case of higher temperature.

As was reported in literature, improvement of structural perfection of grown NWs can be done by tuning temperature and V/III ratio simultaneously. There is a narrow temperature gap for the growth of NWs, but to introduce significant changes in the structures, temperature change of 20°C only is not enough. Nevertheless, comparing current growth mode with so call "typical" growth conditions, we note that the amount of ZB compounds noticeably reduced. I reported about NWs grown at temperatures 445°C and 425°C with V/III ratio 30. The "typical" growth (subchapter 5.1 and 5.2) occurs at temperature 450°C with the V/III ratios 120. The SF density has been estimated by length of the perfect WZ segment: 2nm and 3.2nm, "typical" growth provided the size of 5.65nm. Obvious advantages and disadvantages exist for both growth regimes. Therefore a compromise between the two growth techniques should be found.

5.4 Growth rate

In subchapter 5.2, I compared the NWs grown on the substrates covered with SiOx and on bare Si. It has been mentioned that the growth on SiOx performed at low growth rate (GR) limits the nucleation of InAs islands on SiOx. My results demonstrated a decrease of SF density compared to NWs grown on bare Si with higher growth rate. Of course, the growth rate was not the only factor of difference, which could lead to improvements in structure perfection. In this subchapter, I exam the effect of the growth rate on SF density for NWs grown on SiOx and with a low V/III ratio. There are limited reports about the effect of growth rate on NWs morphology and properties. H. Joyce *et al.* have shown that a rapid nanowires growth rate can significantly improve the nanowire quality. Investigations were performed on GaAs NWs grown by MOCVD with the use of Au catalysts and structural properties are inspected by SEM and TEM. The optical properties have been inspected by photoluminescence spectroscopy. The authors demonstrated that the NWs grown with a rapid growth rate are less tapered, free of planar crystallographic defects and displayed a high phase purity. High flow of group III- and group V materials required a shorter growth time and produce minimum tapering of nanowires. Also, it was proposed that precursor of III- and V-species are supposed to reduce surface and interfacial tensions. The elements of group V have low solubility and behave as surfactants when they become absorbed by the catalysts droplet.

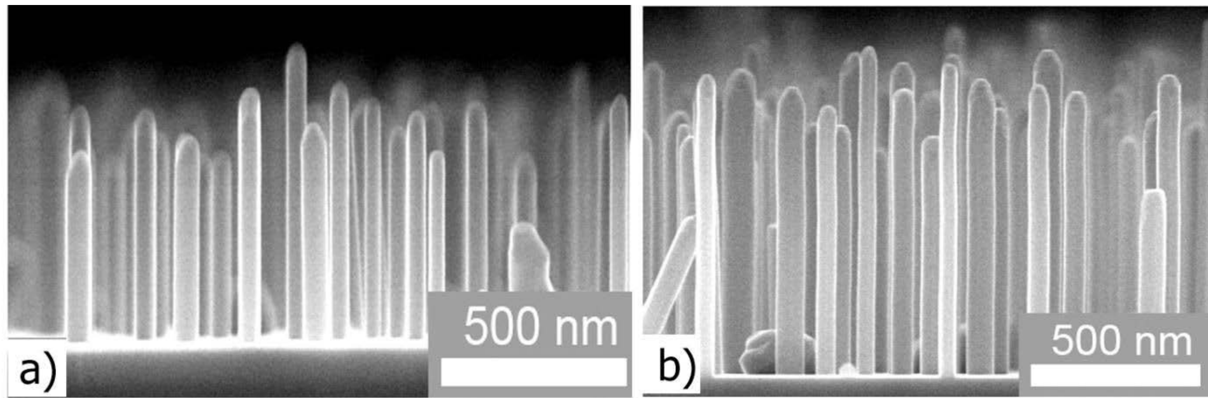

Figure 5.7 SEM images NWs grown with equivalent growth rate for planar InAs a) 50 nm/h; b) 100 nm/h

With higher growth rate both elemental species give rise to reduced surface and interface tensions during the growth, so critical tensions for twin formation is exceeded less often [32]. The influence of growth rate on NWs morphology was investigated by J. Budesh Babu *et al.* [33]. Authors reported on InAs NW grown by Au-assisted MBE mode with use of SEM for characterization. Tuning growth rate, one is able to achieve a rapid growth (up to 4 nm/s) with significant changes in diameter and shape of NWs. The height of grown object may reach 14 μm. But report did not include any internal structure information.

In this part, I tested the influence of the growth rate on structural properties of InAs NWs grown by MBE in catalysts free mode on Si substrate. SEM images are shown on fig. 5.7. Preparation and growth procedures have been described in previous subchapter. The growth time for samples of this series was 30 min independent from the growth rate in planar equivalent. Length of NWs grown with higher growth rate is found to be in range 600-1100 nm with diameter of 30-80nm. In case of the low growth rate, the length of NWs is in the range of 500-700nm with diameter 40-80nm. For the same growth time, it is not surprising to observe a smaller length of NWs with lower growth rate. As I show in chapter 6, nucleation of new NWs does not stop during the growth and explains the variation of NWs length in case of the high growth rate. In both cases, the NWs are vertically aligned and have hexagon shape. Also, parasitic islands can be observed in the SEM images.

Figure 5.8a demonstrates RSMs recorded from both samples. A difference between two RSMs is observed in the region of q_z=42nm^{-1}. Sample of the lower growth rate does not show (331)ZB reflection. The existence of ZB components is proved by the weak signal of (422) reflection. In previous chapters, we mentioned that zinc-blende islands are oriented in the certain way – (331) or (422). Low intense ZB reflections without sign of twin defects can be explained by a small number of parasitic structures and structural perfect ZB compounds.

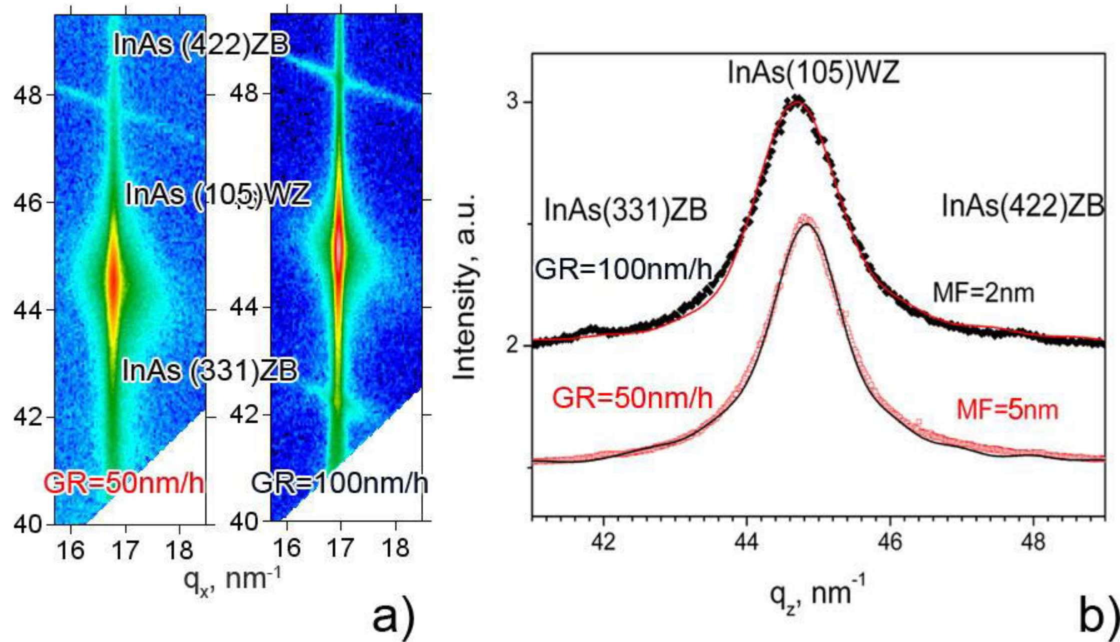

Figure 5.8 a) Reciprocal space maps measured through (331), (105) and (422) reflections from NWs grown with GR=50nm/h (left side) and GR=100nm/h (right side map); b) line profiles extracted from RSMs (dotted lines) and simulation of WZ reflection (solid red line)

The ratio of integrated WZ intensity to the sum of integrated ZB reflections is larger for case of lower growth rate and equal to 4.7, while for the second sample this value equals to 4.2. For the demonstrated growth conditions, the low growth rate reduces a number density of parasitic islands.

At integrated profiles ZB reflections are hardly observed at the top curve (fig. 5.8b) corresponding to the case of high growth rate (GR) and not visible at all for the bottom curve. The FWHM of wurtzite reflection is larger for GR=100nm/h is a sign of the higher SFs density. From simulations we received the lengths of perfect WZ segments to be 5nm for low growth rate and 2nm for high growth rate. In contradiction to [34] we demonstrated that lower growth rate leads to improvements of the structural perfection in terms of a lower islands number and better structural perfection of NWs.

5.5 Conclusions

In this chapter, I presented the results of analysis of different growth modes in terms of SFs density and parasitic growth. For the moment both questions are key problems for InAs growth on Si substrate. I demonstrated mechanism for structure characterization of NWs, which can be used in future investigations. Our results are in agreement with the basic tendency of the growth described in literature. Compared to the "typical" growth regime growth at low V/III ratio and the use of a coating layer, one can reduces a number of parasitic islands. The density of SFs can be reduced by tuning the growth parameters. Important observation is the interplay between these growth parameters. Variation of a single parameter cannot produce improvements of the growth process, but a combination of them may lead to improvements of the phase purity of NWs as it has been demonstrated in publications referred in this chapter.

Sample #	Substrate temperature (°C)	Growth duration (min)	As/In flux ratio	Equivalent growth rate for planar InAs (nm/h)	WZ/ZB ratio	size of perfect WZ segment (nm)	Oxide Layer	Sub chapter
1	450	120	120	100	1.6	2.5	-	5.1, 5.2
2	450	75	120	100 (+200)	2.4	5.6	-	5.1
3	450	260	120	100	2.9	3	X	5.2
4	445	30	30	100	4.2	3.2	X	5.3
5	425	30	30	100	4.7	2	X	5.3,5.4
6	425	30	30	50	4.7	5	X	5.4

Chapter 6

Structural Phase composition of InAs nanowires grown by self-assisted molecular beam epitaxy onto Si(111)

InAs nanowires grown by self-assisted molecular beam epitaxy onto a Si (111) substrate show a transition from a more droplet like to a columnar shape as function of growth time, accompanied by the transition from an In-rich vapour-liquid-solid to an As-rich vapour-solid growth mode. Using sample integrating and single NW resolved X-ray diffraction techniques we studied the phase composition of InAs NWs for both growth conditions. Already after 10 sec of growth the NWs exhibit a high density of stacking faults. For further growth time, the number of defects increases. After 40sec of growth the structure displays a random stacking of InAs bilayers. I show that the stacking fault density increases with increasing growth time. Single NW resolved XRD reveals that the stacking sequence varies random between different NWs. However, in most of the NWs the distances between neighboured SFs show a rather narrow distribution. The transition from In-rich to As-rich MBE growth mode is described in terms of structural defects. The transition of growth modes is accompanied by the increase of SF density.

Chapter is based on paper: A. Davydok, E. Dimakis, A. Biermanns, L. Geelhaar, U. Pietsch, „Structural Phase composition of InAs nanowires grown by self-assisted molecular beam epitaxy onto Si(111)“, *in preparation*

6.1 Introduction.

Combination of the high-speed electrical properties of III-V semiconductors with the optoelectrical properties of Si is of high interest for future electronic devices. That's why in this chapter I will concentrate exactly on such system. Despite the huge lattice mismatch combination of these materials is achievable by nanowire growth onto [111] oriented substrates, e.g. by means of molecular beam epitaxy. NW growth of even highly mismatched systems like InAs onto silicon, showing a lattice mismatch of 11.6% in the bulk phase, has been successfully demonstrated [18]. However, for electrical applications planar defects like stacking faults and twin planes play an important role as scattering centres for charge carriers, leading to degradation of the devices [36]. The crystallographic structure of InAs NWs shows predominantly the hexagonal WZ phase independent from the fact that bulk material and two-dimensional structures are grown in the cubic zinc-blende phase [37]. The NW growth typically takes place along the [0001] hexagonal direction which is parallel to the cubic [111] direction of the substrate. Both zinc-blende and wurtzite phases differ in the sequence of bilayers stacking along the growth direction. Because of the very small difference of formation energies [38], a switching between the two phases during the growth process is hardly to control and leads to the creation of planar defects that can already be monitored by *in-situ* reflection high energy electron diffraction during NW growth. More detailed structural analysis can be performed by High-resolution Transition Electron Microscopy [39-41] and High-resolution- X-ray diffractometry as shown on previous chapter.

However phase control growth of InAs NWs was achieved by different growth technique, like Au-assisted metal-organic chemical vapour deposition and Au-assisted metal-organic vapour phase epitaxy, mainly by tuning the growth parameters in the particular temperature range and the V/III ratio [42]. Krieger *et al* [43] have shown the appearance of other stacking sequences in InAs NWs, grown by MOVPE substrate, such as the 4H phase which is known from SiC [44]. In all cases growth were realized on InAs substrate. In the same time in case of self-assisted InAs NWs grown on silicon substrate independent from growth technique, most of reports are complying about high density of SFs and twin defects [22, 46].

In recent paper [37] authors have reported on InAs NW self-catalytic MBE growth under initially In-rich conditions. It was found that the NW growth rate changes from high (30 μm/h) during the initial time of growth to low (2.5 μm/h) for further growth. This change is explained by the transition from In-rich to As-

rich conditions at the NW growth interface due to the decreasing arrival of Indium adatoms at the growth front caused by the formation of additional nucleation centres. Whereas wurtzite was identified as predominant phase in the initial growth time, the appearance of “streaky” features in RHEED pattern while growing in the As-rich phase was interpreted by an increasing defect density within the hexagonal NWs. A detailed real structure analysis of the grown NW could not be performed.

Most of the papers report on morphology and internal structural analysis of the grown NWs were preformed with SEM and TEM. Instead of TEM, X-ray technique is a non-destructive method, which does not require complicated sample preparation procedure. X-ray diffraction can provide structure information from an ensemble of NWs, but also from a single object with the use of specific nano-focus setup.

In following chapter I will discuss investigation of the phase structure of InAs NWs by means of high-resolution X-ray diffraction techniques. Using sample integrating XRD we show that under As-rich conditions the NW grow with inclusion of a high number of stacking faults. Spatially resolved NW inspection using a focussed X-ray beam reveals that the SF arrangement varies randomly between the NWs but shows a rather sharp distribution of SF distances.

6.2 MBE –Growth

The samples series was grown at 450°C with indium flux F_{In}=100nm/h and ratio V/III=120. Growth was stopped after 10 sec (sample A), 43 sec (sample B), 86 sec (sample C) and 2 hours (sample D). Growth of all samples started with opening of As-cell shutter and after a while - the Indium cell. In the end of growth both shutters were closed simultaneously. The growth time of each sample is defined by the opening time of the In-shutter. To remove the native oxide layer the substrates were etched in 5% HF for 1 min, organic residuals were etched out in H_2SO_4 /H_2O_2 (3:1) for 10 min, for creation atomic flat terraces – in 40% NH_4F for 10 min, and etched in 5% HF for 10s passivate the surface with hydrogen. After each step substrates were rinsed by deionized H_2O. Substrates were dried with N_2 and loaded to the MBE system. Prior to growth the substrates were annealed at temperature more than 500°C. More detail about growth process in [46]- growth series D.

After unload samples from growth chamber all of them were examined with SEM (Fig. 6.1). For short NWs (sample A) SEM cannot distinguish between

NWs and islands, because objects do not differ in shape and exhibit more spherical form. For longer growth time (43 sec) NWs can be identified by the formation of side facets, visible from sample (B); sample (C) clearly observe difference in shape of NWs and islands. According to SEM investigations the length of NWs were estimated as: for sample (A) – 70 nm; sample (B) – 250nm ; sample (C) – 450nm and sample (D) - 4 μm. In the same time the diameter of NWs of all samples equal to ~95 nm, except sample (D) with NWs diameter 160 nm.

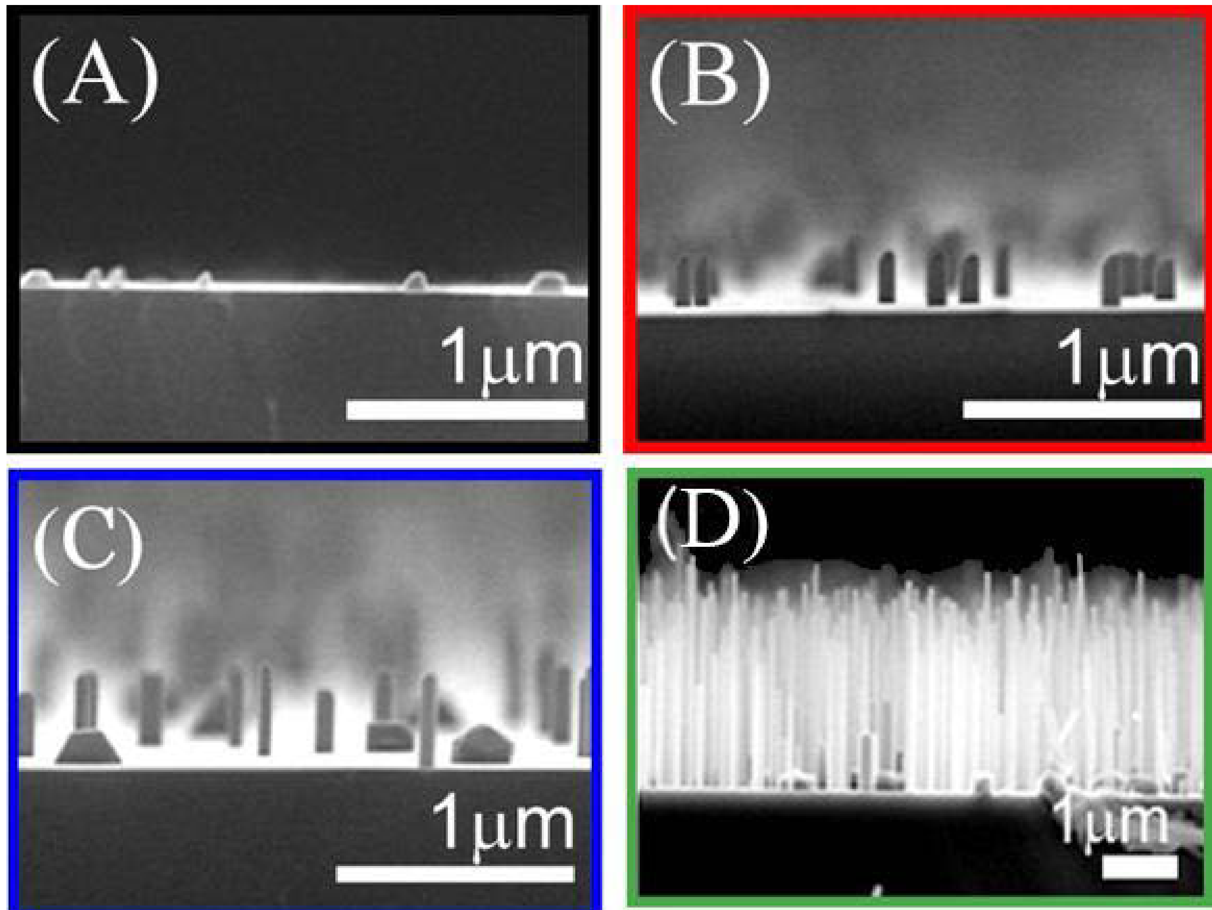

Figure 6.1 SEM images of samples (A)-(D) represent typical shapes of nanostructure on different stages of growth.

6.3 Experimental technique and results

In presented case, integrating XRD measurements at NW ensembles (whole sample) have been performed at the P08 beamline of PETRA III Synchrotron in Hamburg. The incoming monochromatic X-ray beam with energy of 9keV was collimated to a size of 200 x 500 μm² using a set of slits. To record the intensity profiles along the growth direction the incidence angle α_i of the X-

ray beam with respect to the (111) lattice planes of the sample was rocked through the exact Bragg condition with a step of $\Delta\alpha_i$ =0.01°, simultaneously moving detector through the diffraction position with double steps. The diffraction intensities were recorded using a 1D pixel detector, MYTHEN, with pixel size of 50 μm along the α_f direction [47].

X-ray diffraction is a non-destructive tool to characterize crystalline materials. For inspection of NWs various scattering geometries can be employed to probe the phase composition, the lattice parameters and the strain variation along the growth direction. Symmetric X-ray diffraction (sXRD) is applied to inspect lattice parameter and strain along the hexagonal [0001] growth direction. The same Bragg reflection holds for the (111) Bragg peak of zinc-blende structure. In this geometry the ZB and WZ phases can be separated already due to their different out-of-plane lattice parameter which is for InAs d(111)= 0.605nm/sqrt(3)=0.349nm and d(0002)= 0.351nm. In reciprocal space it leads to appearance of two reflections with slightly different q_z position (the transformations form incident and reflected angles to q-coordinates are described in Chapter 3). The larger d-value corresponds to a smaller q_z. Symmetric geometry is realized by simultaneous scan of incident and exit angles through the equal angular range. This measurement in symmetrical geometry, already provide indication of wurtzite and zinc-blende phases. More detail phase analysis can be done in asymmetric out-of-plane geometry (aXRD). Considering bulk lattice parameters and [111] orientation of substrate we identified the (331) reflection to be particular sensitive for zinc-blende but (10i5) reflection as wurtzite sensitive only. Along the same zone the (422) reflection is allowed for zinc-blende structure only. These asymmetric reflections are accessible either in grazing- incidence (grazing incidence angle) or grazing exit (grazing exit angle) geometry. Due to larger incidence angle the later one provides a much smaller foot print. In addition, the positions of these reflections are defined by both in-plane and out-of-plane lattice parameters. From literature the InAs wurtzite in-plane and out-of-plane lattice parameters are a=0.427nm and c=0.702nm [43].

6.3.1 Ensemble measurements

For all samples reciprocal space maps were recorded in vicinity of the (111) Bragg reflection of silicon (Fig. 6.2a). From RSMs one can observe an increase of InAs peak intensity with growth time i.e. an increase of InAs amount. As see in sample (D) the InAs reflex splits in two well resolve peaks. Following observation provoked us to perform measurements in q_x-q_y plane (Fig. 6.2b). We received a pictures with six-strikes around InAs the reflection for sample (A) ; for other

samples the cross-sections are rotated by 30° with respect to each other corresponding to transition from {1 -1 0} side-facets towards {1 1 -2} facets. Considering the time evolution of this feature we attribute the {1 -1 0} appearing first to wurtzite (larger c- lattice parameter) and the second one with {1 1 -2} to zinc-blende appearing at later stage of NW growth. In real space such image can be explained by hexagons but in reciprocal space by strikes pointing to the hexagons facets (Fig. 6.2b). Prior the measurements we aligned samples according Si (422) reflection. It gave us possibility to define orientations of both hexagons (Fig. 6.2b left side).

Extracted line scans along q_z in range of Δq_x=0.1nm^{-1}are shown in Fig.6.3. Both the InAs and Si peaks are clearly separated without major intensity in between. The fact that one of the peaks appears at position close to table value of (111) position of bulk InAs already for sample A, tells us that the large lattice mismatch of 11.6% between InAs and silicon has been already released in this initial state of growth. In so highly mismatched systems the strain is released at the very beginning of growth process after certain critical diameter of InAs NWs through formation of misfit dislocations. This is in agreement with previous studies taken for GaAs NWs grown onto silicon [48]. For the present samples the InAs peak does not appear at the q_z position expected for cubic material at q_{ZB}=17.96nm^{-1} (dotted line). In fact the peak maximum is shifting towards smaller q_z measuring larger out-of-plane lattice parameter of WZ phase (q_{WZ}=17.90nm^{-1}). However, zooming in the InAs peak we identify an asymmetric peak shape which can be decomposed into a less intense ZB peak and a higher intense WZ peak (Fig. 6.3b). The decomposition shows that the relative ZB content decreases from 36% for sample (A) down to 8% for sample (D) (Fig. 6.3b).

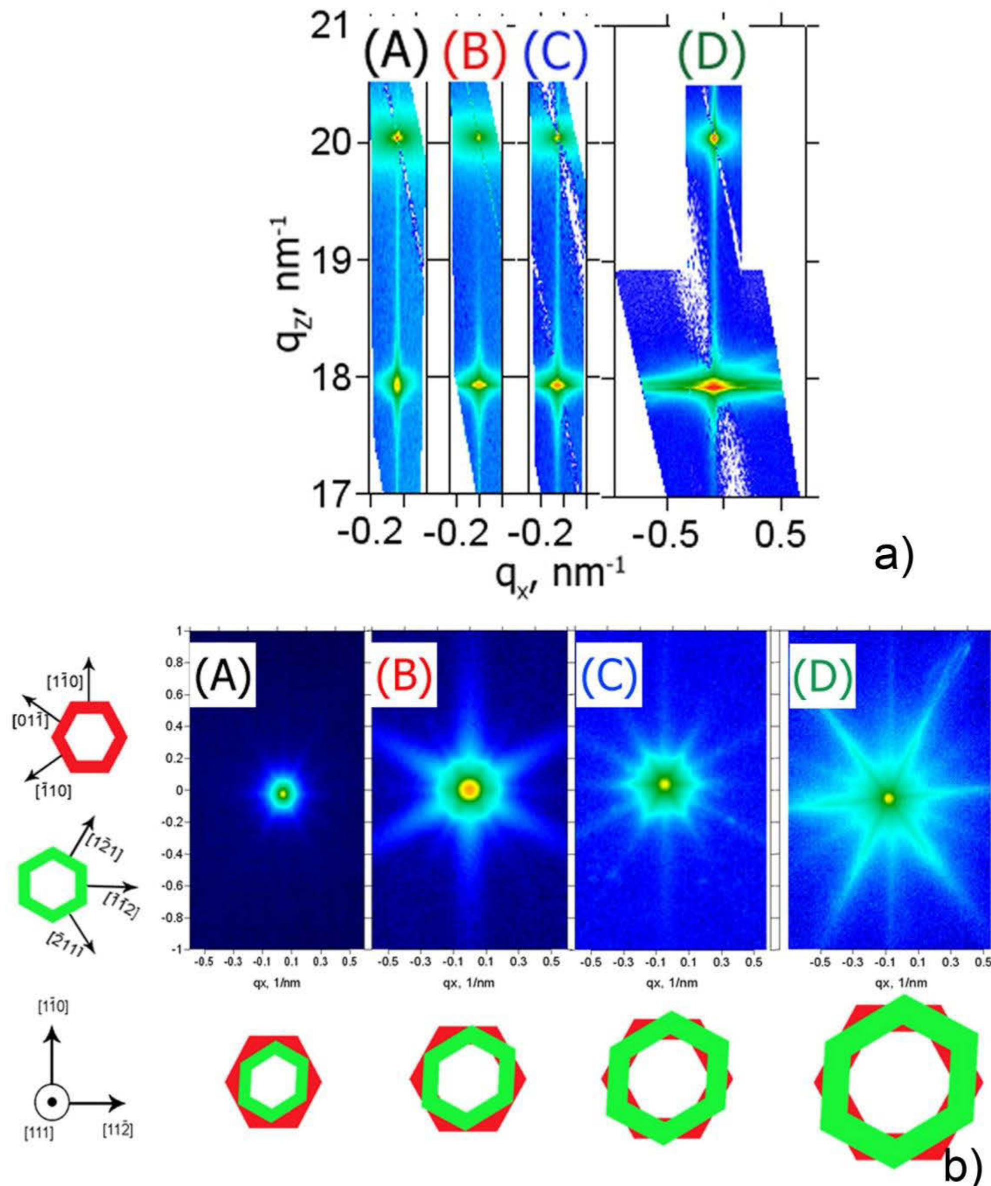

Figure 6.2 RSMs recorded for samples (A)-(D) close to (111) reflections of a) Si (top)and InAs (bottom) reflexes in q_x-q_z plane; b) qx-qy RSMs of InAs reflections samples (A)-(D)

Next we inspected the same samples in asymmetric geometry of X-ray diffraction. Considering the structural relations between ZB and WZ phases explained in [49] we have measured line scans along q_z covered by detector range of q_x=(16.94±1) nm^{-1}, where q_x defines the in-plane lattice parameters which is approximately same for the (422) and (331) ZB reflection at q_z = 41.95nm^{-1} and q_z =48.09nm^{-1}, and the (10i5) WZ reflection at q_z =44.94nm^{-1}, respectively (see Fig. 6.4a). In contrast to (111) all these three reflections are sensitive to the inclusion of SFs [43]. Whereas ZB and WZ peaks show similar intensity and full width at half maximum (FWHM) for sample (A), both intensity and FWHM of the WZ

reflection increase with increasing the NW length. At the same time the FWHM of the ZB reflections stays unchanged and shows a FWHM of same order of magnitude as measured at (111) – see Table 6.1. The considerable increase in FWHM of the (10i5) reflection cannot be explained by the increasing length of the NWs. An increase in length would lead to a decrease of the respective FWHM. Hence, the observed evolution must be caused by the inclusion of SFs.

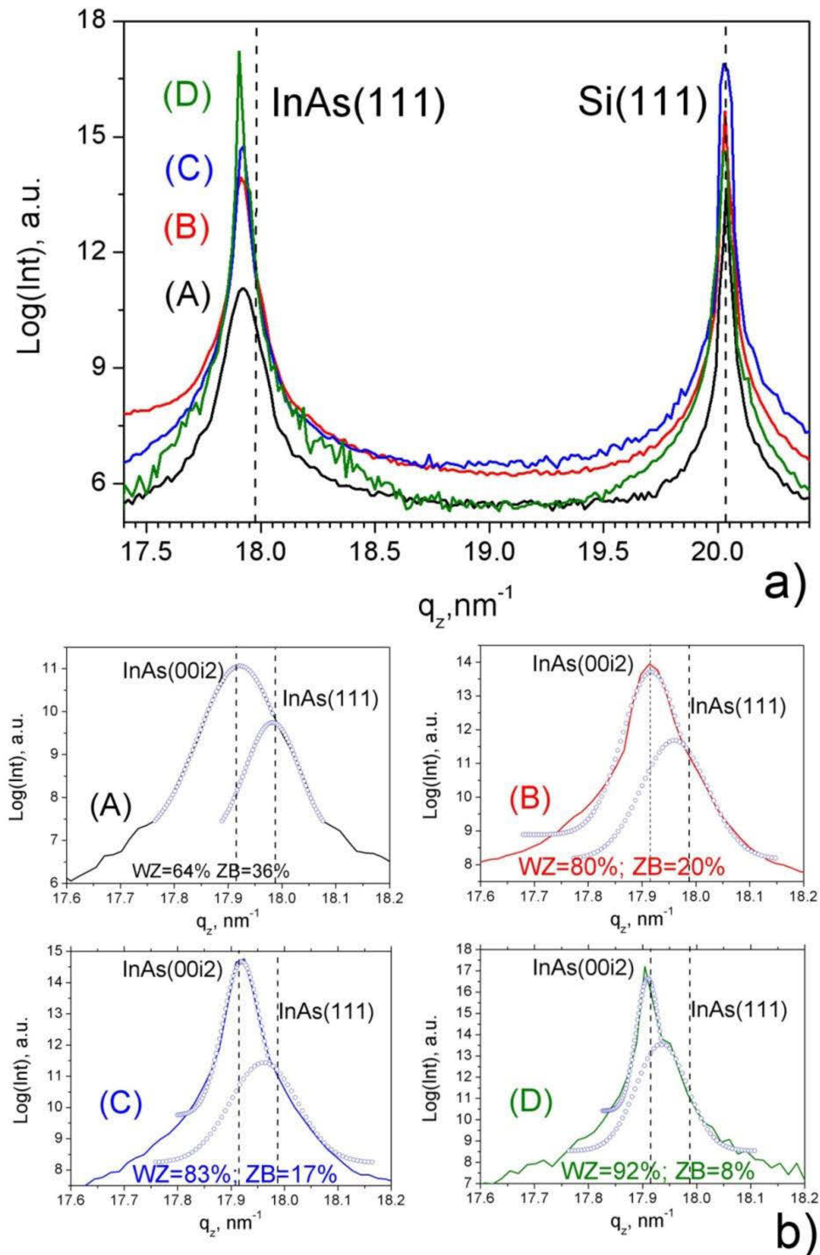

Figure 6.3 a)XRD - (111) reflection of InAs NWs grown onto Si (111) substrate; by dotted line mark expected positions for bulk materials; b) decomposition of InAs (111) peak on ZB and WZ compounds, dotted line mark expected position for both phases.

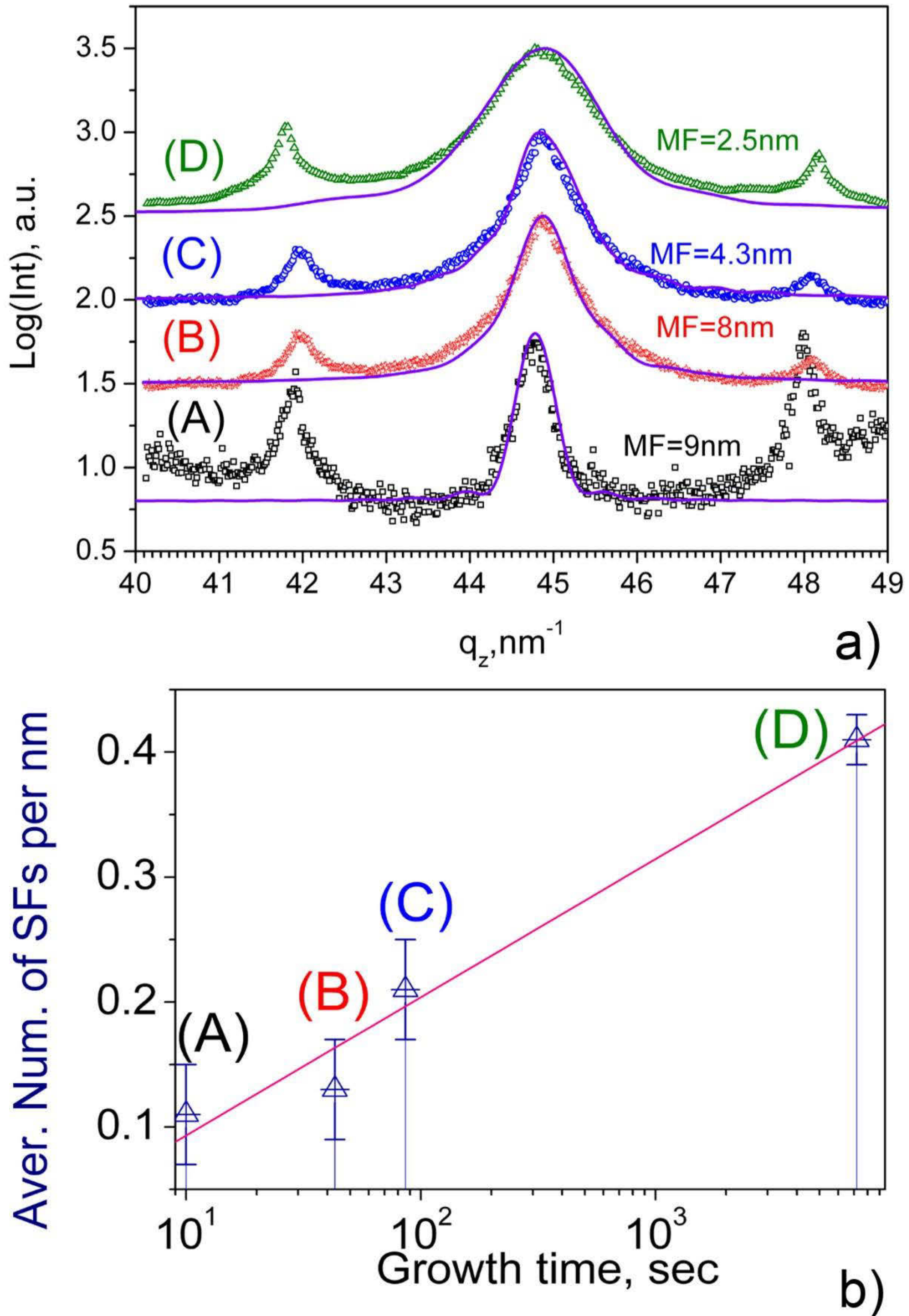

Figure 6.4 a) Asymmetric reflections at q_X=16.94nm^{-1} for samples (A)-(D): measured curves shown by doted lines and theoretical simulations – solid line; b) Dependence average density of stacking faults from the growth time.

Table 6.1

Sample	Growth time, sec	Length, nm	Diameter, nm	FWHM (111), 1/nm	FWHM (331), 1/nm	FWHM (422), 1/nm	FWHM (105), 1/nm	WZ/ZB Ratio
(A)	10	75	90	0.184	0.21	0.1959	0.499	0.42
(B)	43	250	95	0.133	0.251	0.319	1.114	1.24
(C)	86	450	95	0.134	0.246	0.273	1.171	1.26
(D)	7200	4000	160	0.132	0.162	0.17	1.608	1.6

6.3.2 Grazing Incident Diffraction

GID measurements have been performed in order to verify the variation of in-plane lattice parameter during the growth of the NWs. In particular I measured samples (A), (B) and (D) as a samples characterizing an early stage of growth (not NWs yet), a sample already formed NWs and islands and the sample with long NWs and large islands. In the experimental setups, the incident beam hits the samples under a shallow angle incidence α_i =0.15° smaller than the critical angle of silicon (α_C=0.2°) and InAs (α_C=0.284°). GID probes lattice planes perpendicular to the growth axis. Here, I examined the lattice mismatch between the (4-2-2) reflections of Si (Fig. 6.5c) and InAs (Fig. 6.5b). The $(4\overline{2}\overline{2})$ of ZB phase is (300) reflection of wurtzite structure. So probing $(4\overline{2}\overline{2})$, I obtain the signal from both phases. Additional measurements have been performed at an unique WZ reflection (Fig. 6.5a). The Si peak found at $q_{||}$=56.58nm^{-1} corresponds to the bulk value and was used as a reference. For sample (A), InAs (200) reflection appears as a wide hump centred at $q_{||}$=33.82nm^{-1} corresponding to an average in-plane lattice parameter of a_h=4.291Å. This value is in the range of in-plane lattice parameters (marked with red dotted line) of wurtzite InAs known from previous works. The “mixed” reflection of both phases exhibits more intensity and narrow shape: FWHM of (200) is 0.18nm^{-1}; 0.29nm^{-1} of (300). It can be explained by contribution from ZB phase. As estimated from measurements in asymmetric geometry, the amount of ZB InAs should be equal to the amount as WZ InAs on this stage of the growth.

For InAs$(4\overline{2}\overline{2})$ reflection the expected position is at q_{II}=50.85nm^{-1} for bulk InAs with a_C= 6.05Å (black dotted line Fig. 6.5b).But the peak appeared at position of q_{II}=50.77nm^{-1} and corresponds to lattice parameter a_C=6.06 Å. Also the shape of the peak is rather symmetric comparing with sample (C). In case of

sample (C), both reflections (200) and (300) appeared at slightly larger q_{II}. The position of the (200) reflection of sample (C) is q_{II} =33.85nm^{-1} corresponding to a_h= 4.286Å.

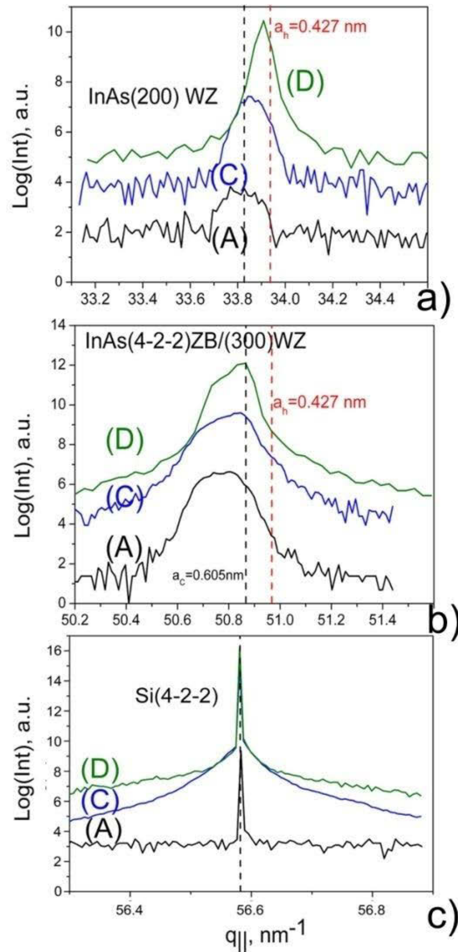

Figure 6.5 Results of GID measurements samples (A), (C), (D): a) unique WZ reflection (002); b) reflection existence for both phases; c) Si ($4\overline{2}\overline{2}$) reflection used for alignments

For sample (D), the (200) peak is shifted further towards larger q_{II}=33.9nm^{-1} corresponding to a lattice parameter a_h= 4.280Å. Following the data received from our experiments in asymmetric geometry the SF density of NWs is increasing during the whole growth process as well as numbers of NWs (Fig. 6.4). The in-plane parameters of WZ phase gradually decreases from 4.291Å to 4.280Å. Possible explanation is formation of side facets corresponding to the switching from vapour-liquid-solid growth to vapour-solid one.

6.3.3 Single wire resolved measurements

Spatially resolved XRD measurements at individual NWs have been performed by use of the nano-focus setup at ID01 of ESRF in Grenoble [50]. The

X-ray beam of 8keV was focused down to a spot size of 300 x 300 nm^2 using a Fresnel zone plate (FZP). Distance from FZP to sample position was 129 mm. The size of the focused beam was sufficiently small in order to separate individual NW´s in coplanar symmetric scattering geometry. For recording the diffraction intensity, we used a 2D pixel detector, MAXIPIX with pixel size of 55 x 55 μm^2.

Single wire resolve measurements were performed with nanosize partly coherent beam (in certain experiment slits setting for improvement of the beam coherence was not used). X-ray beam was focused down to 300 x 300 nm^2 size using Fresnel zone plate. FZP are circular diffraction gratings with radial decreasing line width. Because the refractive index for X-rays differs from 1 by only about 0.1%, diffractive lenses are often preferred for X-ray focusing. The size of the focal spot and therefore the spatial resolution of the microscope is limited by the width of the finest (outermost) zones [52]. FZP was placed 129 mm in front of the sample. A central beamstop was installed before FZP and used for cutting the high-intense central part of the beam. An order-sorting aperture was placed in behind the FZP, to block unfocused part beam coming not from the central part. Only the first diffraction orders produced by the FZP reached the sample (fig.6.6).

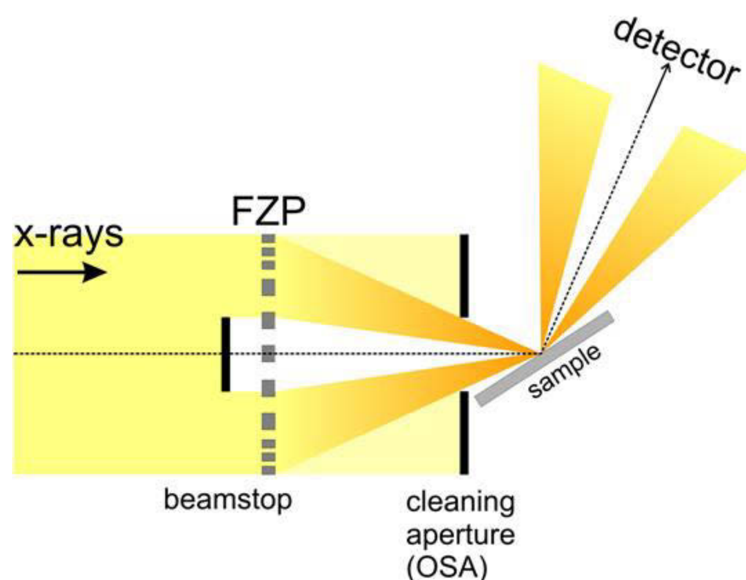

Figure 6.6 Focusing Fresnel Zone Plate setup

Single NW resolved measurements have been performed at samples (C). First we recorded reciprocal space maps in aXRD geometry to find the positions of Bragg reflections with large size beam. The (10i5) WZ peaks was found at q_z=44.9nm^{-1} and the (331) ZB peak at q_z=41.9nm^{-1}. Then the Fresnel zone plate was introduced and spatially resolved intensity maps have been recorded at fixed angular positions using a x-y positioning system below the sample. One intensity map was taken at a position close to WZ (10i5) (fig.6.7a – contour map) and

another one close to the (331) ZB reflection (fig. 6.7a – colour map). Despite the small shift between the two intensity maps, which resulted from the instability of the sample goniometer, structures with reflection in both intensity maps, as the one highlighted by a blue circle, could be easily localized (fig. 6.7a). Some other structures, as the one highlighted by a red circles, appear only in the (331) ZB intensity map, indicating the absence of WZ contribution. Figures 6.7b and 6.7c show reciprocal space maps recorded at spatial positions marked by red and blue circles in fig. 6.7a at (331) Bragg reflection. Figure 6.7d represents RSM of object "2" recorded at (10i5) WZ position. Object "2" marked with blue circle displays no pronounced Bragg peak but exhibits a speckle like scattering pattern along the q_z direction similar to findings published by [53] indicating the appearance of SFs. On the other hand, fig. 6.7b shows a RSM being typical for an island-like object in ZB structure. From oscillations along q_z with $\Delta q_z = 0.06\ nm^{-1}$ we determined the height of the object to be 104 nm which well corresponds to the average height of parasitic island seen in between the NWs of sample (C) in fig.6.1.

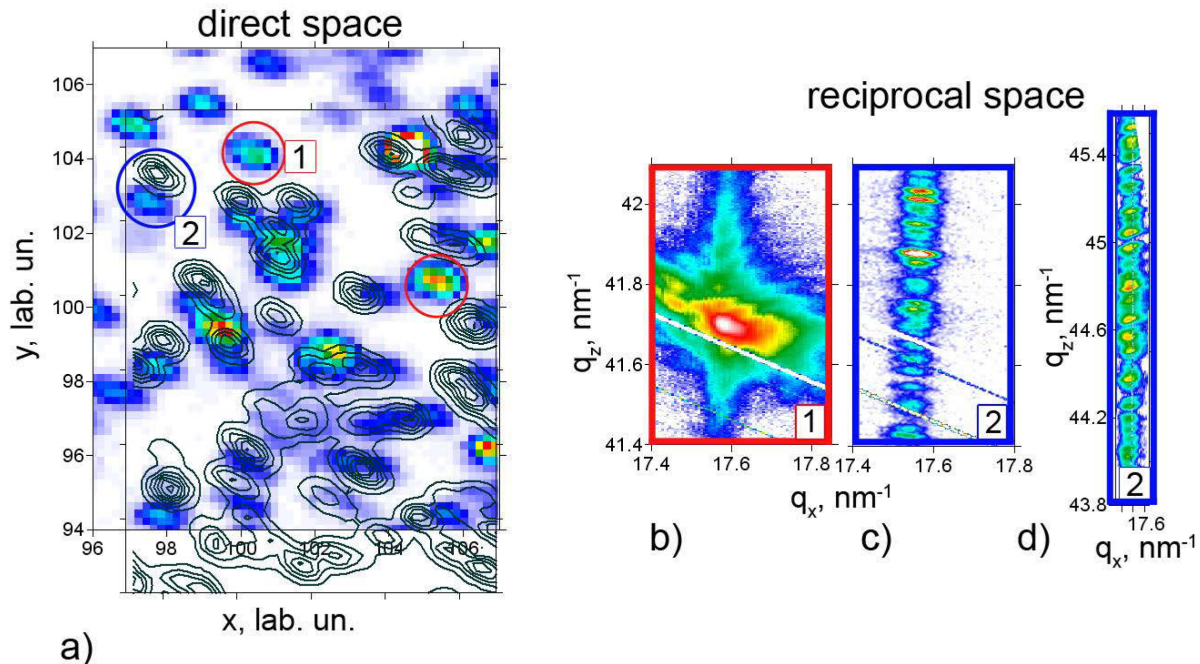

Figure 6.7 a)Overlay of the position maps recorded at InAs(331) reflection (colour map) and InAs (10i5) reflection (contour map); b) RSM of object 1 in qz range of ZB reflection; c) RSM of object 2 in qz range of ZB reflection; d) RSM of object 2 in qz range of WZ reflection

Whereas the RSM taken at other ZB positions are almost similar, the RSM taken at different WZ objects always exhibit a complete different speckle pattern prolonging the whole q_z range. Moreover, only in few cases a particular intensity maximum close to the (10i5) reflection could be identified. This behaviour cannot be explained by the appearance of a dominant WZ phase or another but periodic stacking of InAs bilayers. Therefore we identify the pattern as *distorted phase*.

The speckle pattern can be explained by the coherent superposition of scattering amplitudes created at different uniquely stacked bilayer units separated by SFs. Subsequently a different speckle pattern refers to a different arrangement of SFs within the NWs along wide range of q_z through ZB and WZ reflections. If a large ensemble of NWs with different stacking sequences is probed using a non-focussed X-ray beam, the incoherent superposition of individual diffraction signals of all NWs leads to the broad FWHM of the (10i5) reflection observed in fig.6.4.

The same kind of measurements has been performed for sample (B) – 43sec of growth time. Stability of the diffractometers motors was enough to performed measurements not of selective reflections but scan whole range like it has been done in case of ensemble measurements. The sample was aligned using Si (331) reflection. Prior to single wire characterization RSM in a long range of q_z was recorded with wide beam and the angular positions of Bragg reflections were found. With focused beam (300 x 300nm^2) due to footprint effect we still illuminated the complete wire of 100 x 250 nm^2 size (radial and height respectively) or a complete island. The NWs positions were aligned at (105) reflection by scan of x- and y- motors. No position maps of real space were recorded. Measurements of 4 NWs are shown on fig. 6.8.

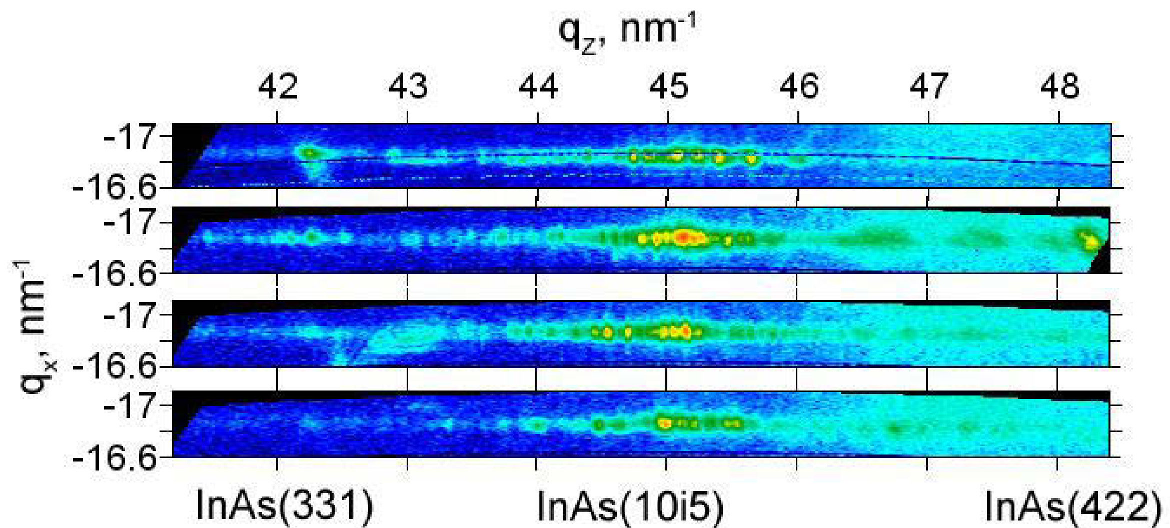

Figure 6.8 RSMs of single NW measured in long rang of q_z from sample (B)

Already after 43 sec of growth the NWs are highly defective. This one may conclude from speckle-like signal at InAs (105) reflection. Also some intensity maxima were observed at ZB reflection positions. As in case of ensemble measurements we observed both ZB reflections – (331) and (422) – along the same line, this is not the case for nano-focus measurements. ZB reflection appears at the side of smaller q_z or at higher q_z but never simultaneously. For now it is of hard to say from where the ZB signal comes. Two possible

explanations can be done. The first is based on the NWs structure formed mainly by not pure wurtzite but partially zinc-blende. Well-oriented ZB domains exist in NW with orientation (331) or (422). The presence of one ZB reflection only tells us about the absence of twin defects. On other hand, slightly misaligned measurements are really sensitive to any vibration of the setups and could lead to a partial illumination of neighbour islands, then as completely ZB and could contribute at zinc-blende position, but does not influence the signal from NWs. Nevertheless, on this stage of investigation it is just speculations. This problem can be solved more direct by TEM analysis with local structure investigations.

6.4 Simulation

Considering the results of NW resolved measurements, the peak broadening of (10i5) reflection seen in the integrating measurements is explained by the inclusion of SFs. For a quantitative analysis we used the approach published recently [29] developed for considering the influence of SFs on the diffraction patterns taken from thin films. Algorithm was adopted for the case of hexagonal nanowires by changing shape function and used to describe defect density (more detailed in Chapter 5). Also For growth series sample memory effects was imitated using for an each simulation step, the results from the preceding step for shorter NWs as started parameters, as these segments are maintained at the bottom of the NWs.

In the result of our calculation the increasing FWHM is correlated with the increasing number of SFs within the NWs separating perfectly stacked sequences of bilayers of decreasing size. Following these parameters a vertical stack of scattering planes was created.

Table 6.2

Sample	Growth time, [sec]	NW Length, [nm]	Average length of WZ segment, [nm]	Mean number of all SFs, $[nm^{-1}]$
(A)	10	75	9±2	0.11
(B)	43	250	7±2	0.15
(C)	86	450	6±2	0.22
(D)	7200	4000	2.5±2	0.41

The results of simulation are shown in Table 6.2 and by solid lines in fig.6.4a. Whereas the width of sample (A) approximately corresponds to the half of the average height of NWs the SF density increases significantly for increasing growth time. The mean length of a perfect WZ segment decreases from 9nm for sample (A) to 2.5 nm for sample (C) and does not fit to a hexagonal phase anymore (see fig.6.4b). Therefore we name it "*distorted phase*".

For more detailed investigation of speckles pattern we measured several samples for which the growth was stopped after 43sec. NWs heights were estimated from SEM images 250 nm (sample B) what perfectly fits to the beam size of 300 x 300nm^2 and gives the possibility to illuminate the whole object. The speckle pattern taken by coherent diffraction from single NWs contains information about the detailed arrangement of SFs within each of the NWs. As shown by [53] for isolated NWs the arrangement of coherently scattering units can be obtained using the mechanism of phase retrieval or by trial and error. One example of the composition of one NW obtained by trial-and-error analysis is shown in fig.6.9d. Although the coincidence between experiment and simulation is not complete a detailed SF arrangement can be obtained. However, this procedure is time consuming and difficult to achieve. Fig.6.9b shows selected line scans along q_z taken from RSM shown in fig.6.9a of sample (B). Few of the speckle patterns of different NWs of same sample show a rather flat intensity distribution (fig 6.9b - #5) without pronounced peaks. Other line scans show pronounced peaks. The q_z-positions of subsidiary peaks differ between the NWs indicating different arrangements of coherently scattering segments. However, these speckle patterns show rather similar distances between subsidiary peaks referring to a rather sharp distribution of segment lengths along the NW axes. For a quantitative analysis we use a cross-correlation of all measured speckle pattern as it was shown for neuronal synchronization [54]. The cross correlation function is defined by:

$$C_{mn}(\Delta q_Z) = \sum_{q_z} \sum_{q_z} I_m(q_Z) * I_n(q_Z + \Delta q_Z) \qquad (6.1),$$

where $I_{m,n}$ are the speckle pattern of wires m and n , respectively. The cross-correlation function estimates the probability to find similar SF distances in different NWs.

For demonstration of the results produced by the cross-correlation function model of two NWs were created with fixed size of a perfect WZ segment. Using the algorithms of phase-retrieval modelling, two of the diffraction pattern with random distribution of SFs was generated. Both models are characterized by the mean distance between two neighbour SFs of 7nm (Fig.6.9c – top curve, with DS

marked mean distance between two neighbour SFs). Corresponding cross-correlation demonstrates a set of the peaks in q-space which in real space are correlated with set of distances aliquot to 7 (14nm, 21nm etc.). In the same manner we expected to find peaks on the CCF-curves from measured diffraction patterned. Here one should note the variation of distances between SFs is much larger then included in the models and it is leading to more complex CCF. Excluding the pattern with rather flat distribution the correlation functions $C_{mn}(\Delta q_z)$ of the other about 10 NWs under inspection exhibit certain correlation peaks at similar Δq_z (see fig.6.9c). The peak at $\Delta q_z = 1.8$ nm^{-1} is generated by the finite q_z interval selected in the experiment (fig. 6.9b). The next large correlation peak found is the peak at $\Delta q_z \approx 0.93$ nm^{-1} corresponding to a distance of $t = \dfrac{2\pi}{\Delta q} =$ 6.8 nm. Comparing the fluctuation of the mentioned peak position in the correlation functions of this distance fluctuates by Δt= 0.4nm only. Another peak is found at $\Delta q_z \approx 0.75$ nm^{-1}, which corresponds to t=8.4 nm and it also is in the range of the SF distances found from ensemble simulations shown in fig. 6.4.

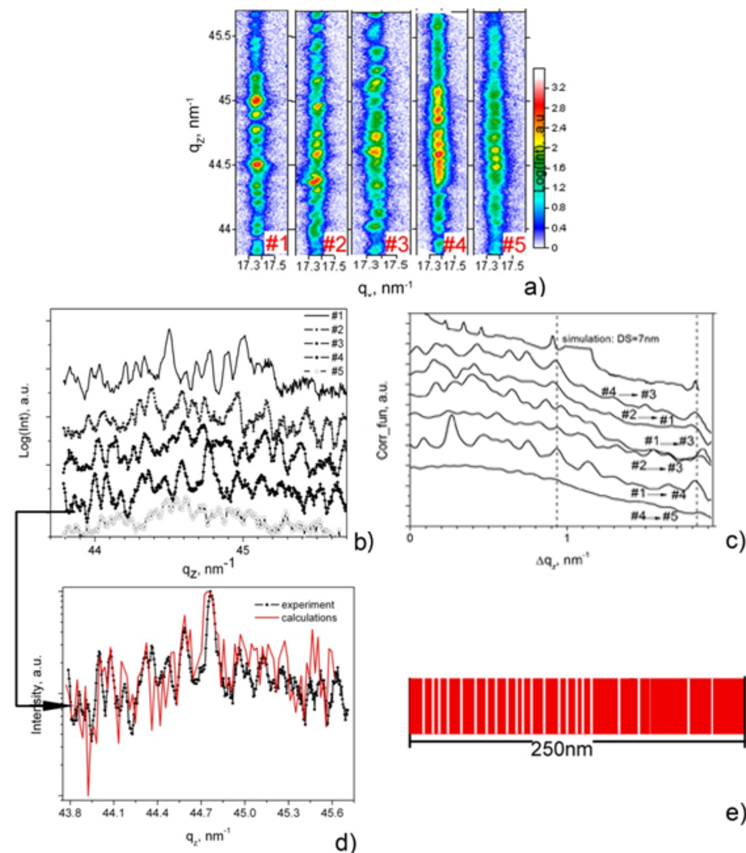

Figure 6.9 a) RSM recorded from different NWs of sample (B); b) line profiles extracted from RSM; c) speckle-speckle correlation function of randomly combined signal; d) phase retrieved SFs sensitive single wire measurements; e) real-space model of retrieval NW (SFs are shown by white lines)

6.5 Discussion

Our measurements show that the MBE grown InAs NWs on Si substrate preferentially show up in the WZ phase, whereas parasitic InAs islands exhibit ZB structure. However, the main outcome of our work is the investigation of the SF probability as function of NW growth. Using sample integrated X-ray diffraction we always find SFs in all NWs independent from growth time and the indicated growth mechanism. Using a statistical method to SF distribution within NWs we could quantify the mean SF density as function of growth time. In detail, we find an increasing number density of stacking faults for increasing the growth time. Whereas in the early stage of growth the mean distance between neighboured SF is in the order of 9nm for 70 nm long NWs, and decreases to 6nm for 500nm long NWs and reduces further to about 3nm for NWs of microns length. The increase in SF density is non-linear, i.e. is seems to saturate after few minutes of growth. Investigating single NWs we find a low SF density for the very small NWs, so we cannot exclude that SF free structures may exist in the early stage of NW growth. That means that the SF formation can be related to the transition from VLS to VS mechanism as discussed in a previous paper where the higher SF density is explained by the influence of the higher adatom diffusion via the NWs side wall which is less dominating in the VLS mode.

Single NW resolved inspection reveals that the SF distribution varies drastically among the NWs grown onto the same sample. Due to the high degree of spatial coherence of the nano-beam, the superposition of scattering amplitudes of different perfectly stacked units within the NW being separated by SFs results in the appearance of speckles. These speckles were measured within a wide q_z range of ± $0.7nm^{-1}$ in vicinity of the expected (10i5) WZ peak position. Form crystallographic point of view this phase cannot be described by WZ or ZB anymore, therefore we name it *"distorted phase"*. NWs exhibit a random arrangement of stacking faults differing from NW to NW.

The appearance of SFs in InAs has been identified by V. Chamard *et al.* using coherent X-ray imaging. However, the authors could not separate single NWs and therefore the SF analysis kept rather qualitative [25]. The detailed SF arrangement can be retrieved from the speckle pattern. This can be done by phase retrieval [22] or by trail and error assuming a certain stacking sequence within the NW [29]. Both methods are very time consuming but less informative with respect of understanding the NW growth. Therefore we applied the cross – correlation analysis to compare the diffraction patterns taken from different NWs and find that most of NWs of one sample show indeed similar distances between neighboured SFs. These distances are in rather good agreement with the results

of the statistical analysis over the whole NW ensemble. In consequence detailed analysis of SF composition is necessary only if physical properties at single NWs will be measured and interpreted.

Stacking faults are hardly connected with diameter of NWs. As shown by [38] the NW free energy is lower for WZ phase then for ZB phase if the NW diameter is below a critical diameter. For InAs the critical diameter is in the order of 10 to 20nm. This is explained by the fact that the number of dangling bonds at the clean non-saturated surface is larger for ZB then for WZ [56]. The surface energy is in competition with the volume cohesive energy which is lower for ZB compared to WZ. The creation of WZ phase strongly depends on the nucleation mechanism [57] and WZ is more energetically favourable for VLS growth. Therefore for NWs with diameter close to the critical one SF formation is likely. Under this growth conditions, the critical diameter is close to 100nm. For an increase of NW diameter, the WZ phase formation becomes instable during fast axial growth. Whereas initially the In- and As- moieties are supplied throughout the top facet only diffusion along the side facets becomes dominant for increasing the growth time. The slightly increasing diameter for increasing the growth time and the supply of material via diffusion along the side facets are associated with the increasing number of SFs. Nevertheless macroscopic fluctuation of growth conditions can be ruled out as origin of SF formation as shown in work of Joyce et al [43].

6.6 Conclusions

In summary, our results support the assumption of a changing growth mode from VLS towards VS in InAs MBE growth suggested in [47]. Both modes results in rather defective WZ NWs. Already after 10 sec of growth a high density of SF has been detected. NW growth in the VS mode, on the other hand, is accompanied by faster increase of number of SFs inclusion where the SF density increases with increasing growth time with nucleation of new NWs during growth.

Conclusions

In the present work X-ray diffraction was applied for real structural investigations of InAs nanowires. The growth process has been studied by probing temporal growth series of samples where the growth time corresponds a certain growth stage of nanowires growth. Evolutions of nanostructures performed by the various growth modes were described. Moreover, the effect of growth parameters on the structure of the nanowires was tested with the use of synchrotron radiation.

X-ray diffraction was used for description of the metal-organic-vapour-phase-epitaxial growth of wurtzite InAs NWs. It was shown that NWs growth is accompanied by appearing of $Ga_xIn_{(1-x)}As$ alloy. This alloy has the zinc-blende structure and grows like wetting layer in the system. Also sign of Au-GaAs alloy was detected at an early stage of the growth process. By GID measurements the phase composition of the structure elements has been described. Growth of wurtzite InAs NWs is observed after 120sec. Based on experimental results substrate/NW interface was described and model of the NWs the growth process is proposed.

On the second step of the investigations, we concentrated on InAs NWs grown by molecular beam epitaxy. MBE allows to grow III-V material NWs nearly on any semiconductor substrate. We characterize InAs NWs grown onto Si[111] substrate under various conditions and with different substrate coverage. The intensity of unique zinc-blende reflection was associated with signal from parasitic islands. Also, using Monte-Carlo simulations based on the average model of NW, estimation of the stacking fault density was done. We have shown that slightly changing the temperature and the growth rate one is able significantly reduce the density of stacking fault. We have demonstrated that the use of low V/III ratio and coating layer provide reduction of parasitic islands. Density of SFs can be omitted by tuning of the growth parameters. The important observation is that a variation of one parameter cannot produce significant improvements of the growth process.

Finally, a detailed structure analysis of InAs NWs grown on bare Si substrate was performed. Array of nanowires was examined realizing symmetrical and asymmetrical geometry of X-ray diffraction. By previous investigations, NWs facets formation was correlated with an increase of SF density. In our experiments with the use of the Monte-Carlo simulation, we have shown that already after 10 seconds of growth time nanostructures exhibit high density of SF. Creation of SF occurs during whole process increasing density of fault inclusions. Single nano-objects were characterized employing nano-focus setup. Scattering pattern from NWs appeared as 'bar-code' signal at position of unique ZB and WZ reflections. High density of SF does not allow to associate such kind of structure with one of structural phases. Each NW demonstrates individual sequences of speckles demonstrating individual structure of every NW grown under the same conditions on the same substrate. Phase retrieval procedure was applied for more detail analysis of speckled patterned. This method is time-consuming and required an exact model of NW with an exact distribution of SF. Alternative way to obtain structural information from a 'bar-code' patterned is the calculation of the correlation function of the two wires. Both techniques estimated the SF density of NWs at a certain growth stage and gave results which are in good agreement with the fit results of the ensemble measurements.

References

[1] C. Thelander, T. Mårtensson, M. T. Björk, B. J. Ohlsson, M. W. Larsson, L. R. Wallenberg, and L. Samuelson Appl. Phys. Lett. 83, 2052 (2003)

[2] E. Lai, W. Kim, P. Yang, Nano Res, 1: 123, 128, 2008

[3] H. Kind, H. Yan, B. Messer, M. Law, P. Yang, Adv. Mater., 14, 2, 2002

[4] Jr H. He,Yi Y. Zhang, J. Liu, D. Moore, G. Bao, Z. L. Wang, J. Phys. Chem. C, Vol. 111, No. 33, 2007

[5] K. Hiruma, M. Yazawa, T. Katsuyama, K. Ogawa, K. Haraguchi, M. Koguchi, H. Kakibayashi, J. Appl. Phys. 77, 447, 1995

[6] M. Björk, B. Ohlsson, T. Sass, A. Persson, C. Thelander, M. Magnusson, K. Deppert, L. Wallenberg, L. Samuelson, Appl. Phys. Lett. 80, 1058–1160, 2001

[7] B.J. Ohlsson, M.T. Björk, A.I. Persson, C. Thelander, L.R. Wallenberg, M.H. Magnusson, K. Deppert, L. Samuelson, Physica E 13, 1126–1130, 2002

[8] K. Dick, K. Deppert, T. Mårtensson, B. Mandl, L. Samuelson, W. Seifert, Nano Lett. 5, 761–764, 2005

[9] S. Dayeh, E. Yu, D. Wang, Nano Lett. 7, 2486–2490, 2007

[10] U. Pietsch, V. Holy, T. Baumbach, High-Resolution X-Ray Scattering. From Thin Films to Lateral Nanostructures. Advanced Texts in Physics, Springer, Berlin, 2005

[11] J. Bauer, V. Gottschalch, G. Wagner, J. Appl. Phys. 104, 114315, 2008

[12] J. Bauer, U. Pietsch, A. Davydok, A. Biermanns, J. Grenzer, V. Gottschalch, G. Wagner, Appl Phys A, 96, 851, 2009

[13] J. Bauer PhD thesis „Metallorganische Gasphasenepitaxie von GaAs- und InAs-Nanodrahtstrukturen über den „vapor-liquid-solid“ - Wachstumsmechanismus“, Fakultät für Physik und Geowissenschaften der Universität Leipzig , 2009

[14] X. Zhang, J. Zou, M. Paladugu, Y. Guo, Y. Wang, Y. Kim, H.J. Joyce, Q. Gao, H.H. Tan, C. Jagadish, Small 5, 366–369, 2009

[15] K. Dick, P. Caroff, J. Bolinsson, M. Messing, J. Johansson, K. Deppert, L. Wallenberg, L. Samuelson, Semiconductor Sci. Technology 25, 024009, 2010

[16] A. Motayed,S.Krylyuk, A. Davydov,Applied Physics Letters 99, 113107, 2011

[17] S.-G. Ihn, J.-I. Song, Nanotechnology, 18, 355603, 2007

[18] H.Shtrikman, R.Popovitz-Biro, A. Kretinin, P.Kacman, IEEE Journal of selected topics in quantum electronics, 17, 4, 2011

[19] D. Kriegner, C. Panse, B. Mandl, K. Dick, M. Keplinger, J. Persson, P. Caro, D. Ercolani, L. Sorba, F. Bechstedt, J. Stangl, G. Bauer, Nano Letters, 11, 1483–1489, 2011

[20] E.Dimakis, J. Lähnemann, U. Jahn, S. Breuer, M. Hilse, L. Geelhaar, H. Riechert, Crystal Growth Designe, 11, 4001,2011

[21] S. Hertenberger, D. Rudolph, S. Bolte, M. Döblinger, M. Bichler, D. Spirkoska, J. J. Finley, G. Abstreiter, G. Koblmüller, Applied Physics Letters 98, 123114, (2011)

[22] K. Tomioka, J. Motohisa, S. Hara, T. Fukui, Nano Letter, 8, 10, (2008)

[23] W. Wei, X. Bao, C. Soci, Y. Ding, Z. Wang, D. Wang Nano Letters, 9, 8, 2926 (2009)

[24] F. Glas, J. Harmand, G. Patriarch, Physical Review Letters, 99, 146101 (2007)

[25] S. Hertenrberger, D. Udolph, J. Becker, M. Bichler, J. Finley, G. Abstrier, G. Koblmüller, Nanotechnology, 23, 235602 (2012)

[26] B. Lewis, J. Anderson, "Nucliation and growth of Thin films", New York: Academic (1979)

[27]V. K. Kabra, D. Pandey, ActaCryst., A, 51 , 329-335 (1995)

[28] M. Barchuk, V. Holý D. Kriegner, J. Stangl S. Schwaiger, F. Scholz ,Physical Review B, 84 , 094113 (2011)

[29] Warren, B., New York: Dover Publication Inc. (1990)

[30] M. Madsen, M. Aagesen, P. Krogstrup, C. Sørensen, J. Nygard, Nanoscale Research Letters, 6, 516, (2011)

[31] T. Rieger, S. Heiderich, S. Lenk, M. I. Lepsa, D. Grützmacher, Journal of Crystal Growth, 353, 39–46, (2012)

[32] B. Mandl, J. Stangle, E. Hilner, A. Zakharov, K. Hillerich, A. Dey, L. Samuelson, G. Bauer, K. Deppert, A. Mikkelsen, Nano Letters, 10, 11, 4443 (2010)

[33] H. Joyce, J. Wong-Leung, Q. Gao, H. Tan, C. Jagadish, Nano Letters 10, 908 (2010)

[34] G. Koblmüller, S. Hertenberger, K.Vizbaras, M. Bichler, F. Bao, J. Zang, G. Abstriter, Nanotechnology, 21, 365602 (2010)

[35] M.Stiles,D. Hamann, *Physical Review B, 38* , 2021-37 (1988)

[36] P. Caroff, K. A. Dick, J. Johansson, M. E. Messing, K. Deppert, L. Samuelson, *Nature Nanothechnology 4* , 50 (2009)

[37]H.Shtrikman,R. Popovitziro, A.Kretinin, L. Houben, M. Heiblum,Bukała, M. Galicka, R. Bucz ko, Perła Kacman,*Nano Letters,* 9,4, 1506 (2009)

[38] Y. Lu, Yi Lu, J. Tu, C. Gu, X. Xia, X. Wang, S.Mao, *Journal of Material Chemistry,* 21, , 4843 (2011)

[39] M. Messing, J. Wong-Leung, Z. Zanolli, H.J. Joyce, H. Tan, Q. Gao, L. Wallenberg, J. Johansson, C. Jagadish, *Nano Letters*,11, 9 , 3899 (2011)

[40] S. Paiman, Q Gao, H J Joyce, Y Kim, H H Tan, C Jagadish, X Zhang, Y Guo, J Zou , *J. Phys. D: Appl. Phys.* 43 , 445402 (2010)

[41] H. J. Joyce, J. Wong-Leung, Q. Gao, H. Tan, C. Jagadish, *Nano Letters*, 10 , 908 (2010)

[42] J. Bolinsson, P. Caroff, B. Mandl, K. Dick, *Nanotechnology*, 22 265606 (2011)

[43] D. Kriegner, C. Panse, B. Mandl, K. Dick, M. Keplinger, J. Persson , P. Caroff, D. Ercolani, L. Sorba, F. Bechstedt, J. Stangl, G. Bauer, *Nano Letters*, 11 , 1483 (2011)

[44] P. Kackell,B. Wenzien, F. Bechstedt, *Physical Review B*, 17037 (1994)

[45] K. Tomioka, J. Motohisa, S. Hara, T. Fukui, *Nano Letters*, 8,10, 3475 (2008)

[46] E.Dimakis, J. Lähnemann, U. Jahn, S. Breuer, M. Hilse, L. Geelhaar, H. Riechert, *Crystal Growth Designe*, 11, 4001 (2011)

[47] O. H. Seeck, C. Deiter, K. Pflaum, F. Bertram, A. Beerlink, H. Franz, J. Horbach, H. Schulte-Schrepping, B. Murphy, M. Greve, O.Magnussen, *Journal of Synchrotron Radiation*, 19, 30 (2012)

[48] A. Biermanns, S. Breuer, A. Davydok, L. Geelhaar, U. Pietsch, *Physica Status Solidi* (RRL) - Rapid Research Letters, 5, 4, 156 (2011)

[49] A. Biermanns, S. Breuer, A. Davydok, L. Geelhaar, U. Pietsch,*Jornal of Applied Crystalography*, 45 , 239 (2012)

[50] A. Biermanns, A. Davydok, H. Paetzelt, A. Diaz, V. Gottschalch, T. H. Metzger, U. Pietsch, *Journal of Synchrotron Radiation*, 16 , 796 (2009)

[51] C. G. Schroer, *Physical Review B*, 74, 033405 (2006)

[52] V Favre-Nicolin, F Mastropietro, J Eymery, D Camacho, Y M Niquet, B M Borg, M E Messing, L-E Wernersson, R. Algra, E. Bakkers, T. Metzger, R. Harder, I. Robinson, *New jornal of Physics*, 12 , 035013 (2010)

[53] M Galicka, M Bukała, R Buczko and P Kacman,*Journal of Physics: Condensed Matter*, 20, 45(2008)

[54] V. Chamard, J. Stangl, S. Labat, B. Mandl, R. Lechner, T. Metzger,*Journal of applied crystallography*, 41(2008)

[55] J. Gulden, S. O. Mariager, A. P. Mancuso, O. M. Yefanov, J. Baltser, P. Krogstrup, J. Patommel, M. Burghammer, R. Feidenhans'l , I. Vartanyants, *Phys. Status Solidi A* 11, 2495 (2011)

Acknowledgments

Foremost, I would like to thank my supervisor, Prof. Ullrich Pietsch, who made it possible for me to work in exciting field of science and welcomed me in his group. His support and guidance has brought me to the end of my PhD thesis I would like to express my gratitude to Andreas Biermanns for guiding in the world of X-ray diffraction experiments and share his experience during long nights at synchrotrons. He has always been open to inspiring discussions. I thank the members of the Solid State Physics group for the inspiring work environment and good working atmosphere. Special thanks go to Jens Bauer, Steffen Breuer, Emanouil Dimakis and Lutz Geelhaar for samples preparation and productive discussions of the results. I am grateful for the support I got from the beamlines staff of ID01 (ESRF), P08 (PETRA III) and BL9 (DELTA). Special thanks go to Prof. V. Holy for sharing programming routine and help in data interpretation. As well as Christian Gutt to whom I am grateful. I want to mention Jörg Grenzer, who is working in related fields of science, I had a great opportunity for exchange of ideas and knowledge. This work would not be possible without the financial support of DFG (Pi 217/38) and DELTA Graduate School, foundations which sponsored my reaserch.

At last, I want to thank my family and friends for keeping up with me and being supportive the whole time I am away.

Appendix

MATLAB Codes

Code 1

```
% MATLAB Code for simulation of X-ray scattering from InAs nanowires ensemble
% based on Monte Carlo algorithm. Adaptation from original code of Prof.V.Holy
% (Charles University, Prague)


ExD=load('*.dat');      %load data-file with phase sensitive scan


hkl=[h k l];            % diffraction indexes in the cubic system

q=qmin:qstep:qmax;      %vector of the q values in the HKL space along [111]
                        in cubic system in number of (111) bilayers

a=a;                    %lattice parametr
epsW=1.641/1.633-1;
N=N;                    % number of the (111) planes in the coherent patch
Np=Np;                  % number of coherent patches
MF=MF;                  % average length of the zincblende segments between
                        neighboring fault planes
cI=ci;                  % relative number of intrinsic SFs
cE=ce;                  % relative number of extrinsic SFs
cT=ct;                  % relative number of twin planes
L=0;                    % coherence width of the primary beam in the monolayer
                        thicknesses (0..ideally coherent primary beam)

pom=cI+cE+cT;
if pom==0;pom=1;end;
pI=cI/pom;pE=cE/pom;pT=cT/pom;

A=[a 0 0; 0 a 0; 0 0 a];  % coordinates of the basis vectors of the direct
                            lattice in the laboratory system
dAs=[1/4  1/4  1/4];            % position of the As atom in the molecule,
                           crystallographic system
p=[1/6 1/6 -1/3];          % lateral shift of the B plane from the A position,
                            crystallographic system
v=[1/3 1/3 1/3];           % vertical shift of the B plane from the A position,
                            crystallographic system

DAs=dAs(1)*A(1,:)+dAs(2)*A(2,:)+dAs(3)*A(3,:);  % position of the As atom in
```

```
                                              the molecule, laboratory system

P=p(1)*A(1,:)+p(2)*A(2,:)+p(3)*A(3,:); % lateral shift of the B plane from the
                                         A position, laboratory system
V=v(1)*A(1,:)+v(2)*A(2,:)+v(3)*A(3,:); % vertical shift of the B plane from
                                         the A position, laboratory system

B=2*pi*(inv(A))';                      %coordinates of the basis vectors of
                                       the reciprocal lattice in the
                                       laboratory system

nq=length(q); Q=zeros(nq,3);       %coordinates of the scattering vector in
                                   the laboratory system

for j=1:3
    for k=1:3
        Q(:,j)=Q(:,j)+(q'+hkl(k))*B(k,j);
    end;
end;
QQ=sqrt(Q(:,1).^2+Q(:,2).^2+Q(:,3).^2); sthL2=QQ.^2/16/pi^2;

w.hkl4(:,1)=(hkl(1)-hkl(2))/2*ones(nq,1);
w.hkl4(:,2)=(hkl(2)-hkl(3))/2*ones(nq,1);
w.hkl4(:,3)=(hkl(1)+hkl(2)+hkl(3))*2/3+2*q;

kappa=exp(-1i*(Q(:,1)*P(1)+Q(:,2)*P(2)+Q(:,3)*P(3)));   % kappa=exp(-iQ.p)

xiW=exp(-1i*(Q(:,1)*V(1)+Q(:,2)*V(2)+Q(:,3)*V(3))*(1+eps));  % xi=exp(-iQ.v)

fTIn=[19.162400   0.547600   18.559600   6.377600   4.2948   25.849900   2.039600
92.802900 4.939100];
fTAs=[16.672300   2.634500   6.070100   0.264700   3.43130   12.947900   4.277900
47.797200 2.531000];   % Thomson coefficients

fIn=fTIn(1)*exp(-sthL2*fTIn(2))+fTIn(3)*exp(-sthL2*fTIn(4))+...
    fTIn(5)*exp(-sthL2*fTIn(6))+fTIn(7)*exp(-sthL2*fTIn(8))+fTIn(9);
fAs=fTAs(1)*exp(-sthL2*fTAs(2))+fTAs(3)*exp(-sthL2*fTAs(4))+...
    fTAs(5)*exp(-sthL2*fTAs(6))+fTAs(7)*exp(-sthL2*fTAs(8))+fTAs(9);

% structure factor of a InAs molecule
phi=(fIn+fAs).*exp(-1i*(Q(:,1)*DAs(1)+Q(:,2)*DAs(2)+Q(:,3)*DAs(3)));


if L>0;
    sig=exp(-(linspace(-N/2-5,N/2+5,N+10)/(2*L)).^2)/(L*sqrt(2*pi));
else
    sig=ones(1,N+10);
end;


vysl=zeros(nq,1);
d=zeros(nq,1);

for jp=1:Np                                   % loop over the patches
```

```
Ms=0;                                         % generation of the positions of the
                                              fault planes, geometric distribution
                                              of the distances
    k=1;
    while Ms<N;
        dist=randraw('geom',1/(1+MF),1);
        if dist>3;
            wtyp=rand(1);
            ityp(k)=0;
            if wtyp<pI;
                ityp(k)=1;
            end;
            if wtyp>=pI && wtyp<pI+pE;
                ityp(k)=2;
            end;
            if wtyp>=pI+pE && wtyp<pI+pE+pT;
                ityp(k)=3;
            end;
            Ms=Ms+dist;
            M(k)=Ms;
            k=k+1;
        end;
    end;


    ampl=zeros(nq,1);                   % calculation of the amplitude

    xic=ones(nq,1);
    kappac=ones(nq,1);
    isigs=1;
    k=1;
    j=1;


    while j<=N;                               % loop over the basal planes
        if j<M(k);
            isig=isigs;
            xic=xic.*(xiW.^isig);
            kappac=kappac.*(kappa.^isig);
            ampl=ampl+phi.*kappac.*xic*sig(j);
            j=j+1;
        end;
        if j==M(k);
            switch ityp(k);
                case 0;
                    isig=isigs;
                    xic=xic.*(xiW.^isig);
                    kappac=kappac.*(kappa.^isig);
                    ampl=ampl+phi.*kappac.*xic;
                    j=j+1;
                case 1;
                    isig=-isigs;
                    xic=xic.*xiW;
                    kappac=kappac.*(kappa.^isig);
                    ampl=ampl+phi.*kappac.*xic*sig(j);
```

```
                    j=j+1;
                    isigs=isig;
                    isig=-isigs;
                    xic=xic.*xiW;
                    kappac=kappac.*(kappa.^isig);
                    ampl=ampl+phi.*kappac.*xic*sig(j);
                    j=j+1;
                    isigs=isig;
                    if jp==1;
                        w.sig(j)=isig;
                    end;
                    j=j+1;
                    isigs=isig;
                case 2;
                    isig=-isigs;
                    xic=xic.*xiW;
                    kappac=kappac.*(kappa.^isig);
                    ampl=ampl+phi.*kappac.*xic*sig(j);
                    j=j+1;
                    xic=xic.*(xiW.^isig);
                    kappac=kappac.*(kappa.^isig);
                    ampl=ampl+phi.*kappac.*xic*sig(j);
                    j=j+1;
                    xic=xic.*xiW;
                    ampl=ampl+phi.*kappac.*xic*sig(j);
                    j=j+1;
                 case 3;
                    isig=-isigs;
                    xic=xic.*xiW;
                    kappac=kappac.*(kappa.^isig);
                    ampl=ampl+phi.*kappac.*xic*sig(j);
                    j=j+1;
                 end;
            k=k+1;
        end;

    end;
        amplS=abs(ampl).^2;
       vysl=vysl+abs(ampl).^2;
    end;

w.q=q;w.int=vysl/Np;
w.int=w.int;
M1=max(w.int);
NormInt=w.int/M1;
ExD2=ExDInt;
M2=max(ExD2);
NormIntEx=ExDInt/M2;
plot(q,NormIntEx,'black')
hold on;
plot(q,NormInt,'o-');
```

Code 2

```
% MATLAB Code for simulation of X-ray scattering from single InAs nanowire
% with compound phase structure

wlength=lambda;                              %length of wire in nm
ac=a;                                  % lattice parameter of matereal in nm
aw=ac*sqrt(2)/2;
natom=3*round(wlength/ac);                   % numbers of layers
zbatom=zb;                                   % number of ZB layers
wzatom=natom-zbatom;                         % number of WZ layers
qz=qmin:qstep:qmax;                          % range of qz
qx=qx;
qy=qy;
count=1;

%In Thomson coefficients
a1=[19.162,18.560,4.295,2.040]; b1=[0.548,6.378,25.850,92.803]; c1=4.939;
%As
a2=[16.672,6.070,3.431,4.278]; b2=[2.635,0.265,12.948,47.797]; c2=2.531;

x=0;y=0;


for k=1:zbatom                               %creation of Zb stack
type(k)=mod(k,3)+1;
end;

for k=1:wzatom                               %creation of WZ stack
type2(k)=mod(k,2)+1;
end;


m=length(qz);

A1=0;
A2=0;

while count<=length(qz)                      % loop over qz range
```

```
    fIn=0;
    fAs=0;

       fIn=fIn+sum(a1.*exp(-b1.*(qz(count)/10/(4*pi))^2))+c1;
       fAs=fAs+sum(a2.*exp(-b2.*(qz(count)/10/(4*pi))^2))+c2;


       F(count)=0;

      for j=1:zbatom
         if type(j)==2
             dx(j)=0; dy(j)=0;
          end;
          if type(j)==1
              dx(j)=aw/2; dy(j)=aw/(2*sqrt(3));
            end;
          if type(j)==3
            dx(j)=0; dy(j)=aw/sqrt(3);
          end;

          z1(j)=j*(sqrt(3)/3)*ac;
          z2(j)=j*(sqrt(3)/3)*ac+0.25*sqrt(3)*ac;

F(count)=F(count)+fIn*exp(i*qz(count)*z1(j))*exp(i*qx*(x+dx(j)))*exp(i*qy*(y+d
y(j)));

F(count)=F(count)+fAs*exp(i*qz(count)*(z2(j)))*exp(i*qx*(x+dx(j)))*exp(i*qy*(y
+dy(j)));
       end;

         A1(count)=abs(F(count))^2;

         for j=1:wzatom

           if type2(j)==1
             dx(j)=0; dy(j)=aw/sqrt(3);
          end;
          if type2(j)==3
              dx(j)=aw/2; dy(j)=aw/(2*sqrt(3));
          end;
          if type2(j)==2
            dx(j)=0; dy(j)=0;
          end;

          z1(j)=j*(sqrt(4/3))*ac/2;
          z2(j)=j*(sqrt(4/3)/2)*ac+0.25*sqrt(4/3)*ac;

F(count)=F(count)+fIn*exp(i*qz(count)*z1(j))*exp(i*qx*(x+dx(j)))*exp(i*qy*(y+d
y(j)));

F(count)=F(count)+fAs*exp(i*qz(count)*(z2(j)))*exp(i*qx*(x+dx(j)))*exp(i*qy*(y
+dy(j)));
       end;
```

```
        A2(count)=abs(F(count))^2;


        count=count+1;
end;

semilogy(qz,A);
```